DEVELOPMENT AND APPLICATION OF NOVEL PHYSIOLOGICAL MRI METHODS TO IMAGE CHANGES IN OXYGENATION

by

Alan Huang

A dissertation submitted to Johns Hopkins University in conformity with the requirements for the degree of Doctor of Philosophy

Baltimore, Maryland
January 2014

Abstract

Acute ischemic stroke is the third leading cause of death and leading cause of disability in developed countries. An ischemic stroke results when there is an obstruction of the blood supply to the brain. When a patient presents with acute ischemic stroke in the emergency room, the first decision that needs to be made is whether or not the patient is a suitable candidate for thrombolytic treatment, which can be risky and lead to death. Currently, doctors use a combination of multiple magnetic resonance imaging (MRI) scans to determine whether or not a patient is suitable for thrombolytic treatment. The combination of diffusion and perfusion scans allow doctors to see regions of the brain that have already infarcted and regions at risk of infarction. However, perfusion scans frequently overestimate the tissue at risk of infarction, which results in stroke patients being taken in for aggressive therapies that they may not benefit from. In this dissertation, I explored three ways to improve the current state of diagnostic stroke imaging by allowing for better visualization of regions at risk of infarction and by doing this non-invasively.

Upon lack of oxygen delivery to the brain, autoregulatory mechanisms lead to vasodilatation of cerebral blood vessels. After blood vessels vasodilatate for an extended time, cerebral blood vessels eventually collapse, and the region of tissue supplied by these vessels progress to infarction. I hypothesized that regions of the brain with increased cerebral blood volume (as a result of vasodilatation) could be salvageable with thrombolytic therapy. To image these regions, I scanned eighteen patients using Vascular Space Occupancy (VASO) MRI, a new method sensitive to changes in cerebral blood volume. While VASO MRI can provide a different type of contrast and potentially offers information that is not available through diffusion and perfusion scans, it is cumbersome to process VASO images, and VASO MRI can be confounded by changes in T_1 especially if tissue has already progressed to infarction.

Recent research has shown that pH is a better indicator of regions of the brain at risk of irreversible damage. Chemical exchange saturation transfer (CEST) MRI is a novel MRI method that is sensitive changes in the exchange rate between bulk water and exchangeable protons on proteins. Amide proton transfer (APT) MRI is a subset of CEST-based techniques that is sensitive to changes in pH. I scanned healthy volunteers and acute stroke patients with APT MRI. I showed that APT MRI has the potential to accurately determine whether or not a region of tissue is at risk of infarction.

It has also been shown that changes in the oxygen extraction fraction, the percentage of available oxygen extracted by the brain from the blood, is also a useful indicator when making decisions about unique treatment plans for each patient. Hemoglobin, the protein responsible for transporting oxygen to all parts of the body, exists in two different states (oxyhemoglobin and deoxyhemoglobin), each with exchangeable protons in different parts of the spectrum. By applying CEST and frequency label exchange (FLEX) transfer MRI in bovine blood, I detected differences in the oxygenation of hemoglobin.

The work completed in this dissertation has the potential to aid physicians in treatment planning for acute ischemic stroke patients.

Thesis Committee

Dr. Peter van Zijl (thesis advisor, reader)
F.M. Kirby Center for Functional Brain Imaging,
The Russell H. Morgan Department of Radiology and Radiological Science,
Johns Hopkins University

Dr. Susumu Mori (reader)
Department of Biomedical Engineering,
F.M. Kirby Center for Functional Brain Imaging,
The Russell H. Morgan Department of Radiology and Radiological Science,
Johns Hopkins University

Dr. Peter Barker
F.M. Kirby Center for Functional Brain Imaging,
The Russell H. Morgan Department of Radiology and Radiological Science,
Johns Hopkins University

Dr. Argye Hillis-Trupe
Department of Neurology,
Department of Physical Medicine and Rehabilitation,
Department of Cognitive Science,
Johns Hopkins University

Acknowledgements

This work would not have been possible without the constant and amazing support of my PhD advisor, Dr. Peter van Zijl. I have not only learned how to actively pursue a problem in science from Peter, but also how to negotiate, how to enjoy life (World Cup in front of MR1), how to make simple presentations that get the point across, and how to present. Thank you for your guidance, your wisdom, and the many lessons that I have learned from you about magnetic resonance, science, and life.

Next, I would like to thank my family. I thank my wife, Chun-Ting Chao 趙君婷, for the constant support she offered me even when it meant spending our first Christmas and first New Year's as a married couple in the lab. I thank my mother, my father, and my brother, Bernard for giving me constant support during my PhD program and being understanding when final exams, abstract deadlines, and conference deadlines prevented me from going home to Texas. I would also like to thank my cousin, Dr. Ching-Hui Huang, and cousin-in-law, Dr. Kido Nwe, for insightful discussions about CEST.

I would also like to thank my committee members, Dr. Peter Barker Dr. Susumu Mori, and Dr. Argye Hillis for their suggestions to my dissertation. Thank you Dr. Barker and Dr. Mori for insights regarding CEST imaging, and thank you Dr. Hillis for advice about developing new sequences for acute stroke imaging.

I would also like to thank all of the members of the F.M. Kirby Center for their friendship and interesting (and quite often amusing) lunch discussions. I would like to thank Dr. Jun Hua for always being able to stimulate my nose with his lunches and with his help and his guidance with MT-VASO MRI. I would like to thank Dr. Craig Jones for his advice about life (about dealing with parents and in-laws about wedding plans) and for his help with python, with MATLAB, and with CEST. I would like to thank Dr. Nirbhay Yadav for his help with python and with FLEX. I would like to thank Dr. Ksenija Grgac for all of her help related to learning how to operate the perfusion phantom, operating the perfusion phantom, and learning how to fix any problem that derives out of perfusion phantom-based experiments. I would like to thank Dr. Jiadi Xu for his help in the animal facility on the 500 MHz and 700 MHz spectrometers. Thank you Dr. Jonathan Farrell and Dr. Bennett Landman for your help with modeling code. I would like to thank Dr. Manus Donahue for introducing me into the lab and to arterial spin labeling. Thank you Dr. Qin Qin for your thought-provoking discussions with ASL. And thank you Ying Cheng, Dr. Jim Pekar, Dr. Ann Choe, Dr. Xu Li, Dr. Juan Wei, Dr. Haifeng Zeng, Dr. Suresh Joel, Dr. Samson Jarso, and Dr. Issel Lim for being great friends. I would also like to thank Joseph Gillen for all of his help with issues related to the MR scanner and to issues related to Godzilla/House/Sumatra. My deepest gratitude goes to the MRI techs Ms. Terri Brawner, Ms. Kathleen Kahl, and Ms. Ivana Kusevic for all of their help related to operating the MR machine and the many times that they scanned me with my sequences while I went into the machine. And last but not least, I would like to thank Ms. Candace Herbster for either knowing the answer to all most questions related to KKI or if not the answer, then knowing who to find to give me the proper answer, and Mrs. Heather Mackey for ordering any materials I need the second that I request them.

I would like to thank my collaborator Dr. Richard Leigh for his effort in selecting suitable patients for my APT in acute stroke project. I would like to thank my collaborators at the NIH for the VASO in acute stroke project, Dr. Steven Warach and Dr. Li An.

I would also like to thank Hong Lan, the go-to person for any problems related to procedures in the BME department and in life. Thank you for all of your advice, and I would like to thank the Biomedical Engineering department for giving me the opportunity to train here and to lead you from 2009-2010.

Finally, I would like to thank all of my friends and roommates in Baltimore who have made my time in the PhD program pass quickly. Thank you Dr. Ji-Liang Shiu, Wan-Ting Chen, Kate Huang, and Janice Lu. Thank you “222ers” Yunching Chen, Pailing Lo, Yunke Song, Ariel Yung, Bryce Chiang, Pauline Che, Xindong Song, Henan Xu, Dr. Cheng-Ran Huang, Yu-Ja Huang, Brook Sung, Angela Chen, April Zhao, Engine Chen, Dan Jiang, Lin Guo, and Nan Zhou. And thank you to everyone else who participated in 222 activities Dr. Nan Li, Wei-Chiang Chen, Cecilia Ng, Dr. Alice Ho, and Derrick Lum. Thank you Dr. Suneil Hosmane for insightful discussions on post-PhD career options such as management consulting and investment banking.

Finally, I thank all of my volunteers who went into the scanner for me so I could collect all of the data needed to graduate!

Table of Contents

Chapter 5. Assessing Cerebral Blood Volume Changes in Acute Ischemic Stroke Patients Using Magnetization Transfer-Enhanced Vascular Space Occupancy (MT-VASO) ……………………………………………………………………………55

List of Tables

List of Figures

Chapter 1. Introduction and Overview

1.1 Introduction

Management of acute ischemic cerebrovascular syndrome (AICS), more commonly known as acute ischemic stroke, is complicated by the heterogeneity of the disease, by the need to make fast individualized decisions on a per patient basis, and by deleterious side effects of aggressive treatments. Magnetic resonance imaging (MRI) is an emerging form of diagnostic imaging with the potential of deriving many new contrast mechanisms by manipulating the timing of radiofrequency and magnetic field gradient pulses. Three-dimensional images can be acquired quickly, non-invasively, with high spatial resolution, and without delivering ionizing radiation to the patient.

In acute ischemic stroke, an embolus or thrombus obstructs blood flow to certain regions of the brain and reduces cerebral perfusion, needed for delivery of oxygen to the brain. This results in a "core" region of the brain (where neurons cannot survive due to the lack of oxygen) that progresses to infarction (in other words, dies) and is unsalvageable with any treatment. However, a few decades ago it was found using Positron Emission Tomography (an imaging modality that measures cerebral metabolism and perfusion using radiotracers injected into the bloodstream) that regions of the brain surrounding the core that have low perfusion and are electrically inactive but are not yet irreversibly damaged can be salvaged with thrombolytic therapy. This salvageable region of the brain has been termed the "ischemic penumbra". More recently, the original definition of penumbra has been somewhat modified in that the complete region of reduced perfusion surrounding the core has been included, which generally is larger than just electrically dysfunctional tissue, Depending on the type of imaging used, multiple penumbra (perfusion-based, pH-based, oxygen extraction based) have been defined in an attempt to guide therapy of ischemic stroke patients. There are currently three main therapeutic options available to restore blood flow to the brain: 1) intravenous tissue plasminogen activator (IV-tPA); 2) intra-arterial tPA (IA-tPA); and 3) mechanical thrombectomy (clot retraction). Each therapeutic option carries its own benefits and risks, while neurologists frequently have to use incomplete diagnostic information to make a decision to treat or not, and which therapy to use. Current MR methodologies focus on perfusion deficits and frequently overestimate the ischemic penumbra, which results in patients being taken for aggressive therapy and being exposed to unnecessary risks. This dissertation is written with the long-term goal of advancing the field of diagnostic stroke imaging with the development and application of novel MRI contrast mechanisms to image the ischemic penumbra in AICS patients.

1.2. Overview

This dissertation is organized in the following way. First, the reader is given an introduction into the physical mechanisms of nuclear magnetic resonance (**Chapter 2**). Next, the reader is introduced to blood (and its components) and how blood delivers oxygen to the rest of the body to maintain aerobic metabolism (**Chapter 3**). Following this, the reader is introduced to acute ischemic stroke, a particular pathology where oxygen delivery is disrupted due to vessel blockage and, depending on the level of disruption, causes a cascade of changes in the human brain (**Chapter 4**). Next, **Chapter 5** presents the work done on optimizing Vascular Space Occupancy (VASO) MRI, a cerebral blood volume sensitive method, to image the ischemic penumbra based on changes in cerebral blood volume during ischemia. After seeing interesting results using VASO, we decided to image tissue pH, a parameter that should be a better indicator of tissue at risk, as it is only changed when anaerobic metabolism starts to occur. Results of optimizing the pulse sequence, testing on healthy volunteers, and applying the pulse sequence to image intracellular pH in acute ischemic stroke patients are presented in **Chapter 6**. Then, preliminary data from a novel idea to use signals of exchangeable protons on hemoglobin proteins in blood to measure oxygenation are presented in **Chapter 7**. Finally, **Chapter 8** summarizes the work and identifies some potential future research directions.

Chapter 2. Basic Principles of Magnetic Resonance Imaging

2.1. Chapter Goal

This chapter introduces the reader to fundamental concepts of magnetic resonance imaging (MRI). Because this dissertation is focused on the optimization and development of novel magnetic resonance imaging techniques, it is important to have a fundamental understanding of how the MRI machine generates images.

"Magnetic resonance imaging is actually nuclear magnetic resonance imaging, but scientists in the field removed the term "nuclear" from the name because at the time, the general public had a fear of the term nuclear."

- Peter van Zijl, from multiple introductory lectures on MRI methods

2.2. Quantum Mechanical Description of Nuclear Magnetic Resonance (NMR)

Nuclei have four unique properties: mass, electric charge, magnetism, and spin. Spin is a form of angular momentum that is intrinsic to the nucleus. Due to the broad scope of this topic, we will limit discussion to hydrogen nuclei, the most commonly studied nuclei in NMR. It is a spin-1/2 particle. When it is placed in a large external magnetic field, it becomes quantized to two states ($m_z = +1/2$ and $m_z = -1/2$) only due to the interaction between the magnetic moment and the field. The energy difference between these two states is described by equation 2.1.

$$\Delta E = \gamma_H \hbar B_0 \qquad \text{(Equation 2.1)}$$

Where γ_H is 267.522x106 rad/(T·s) and represents the gyromagnetic ratio (the ratio of magnetic moment of the nucleus and its angular momentum) of hydrogen; ħ is Plank's constant (6.626068×10^{-34} m^2 kg / s) divided by 2π; and B_0 represents the large external magnetic field and has units of Tesla (T). The energy difference is related to the frequency of precession through the following relationship: $\Delta E=\hbar\omega$.

$$\omega_0 = \gamma_H B_0 \qquad \text{(Equation 2.2)}$$

This frequency, ω_0 (rad/s), is known as the Larmor frequency.

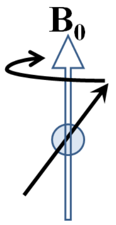

Figure 2.1. A hydrogen nuclei precesses at the Larmor frequency, proportional to the large external magnetic field it is placed in.

When a group of spin-1/2 is placed in a magnetic field, every spin aligns in one of two directions: with the magnetic field (lower energy) or against the magnetic field (higher energy). This is known as the Zeeman effect (figure 2.2).

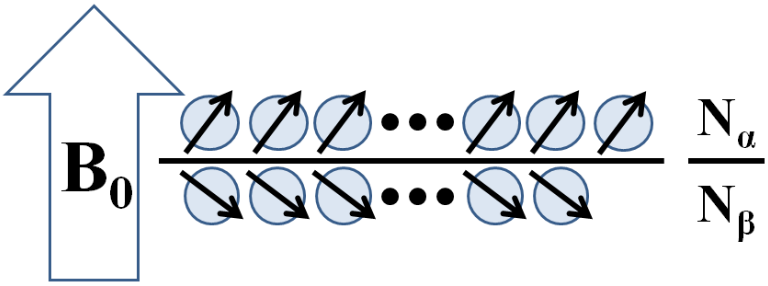

Figure 2.2. Distribution of spins aligning with and against B_0.

The Boltzmann distribution (equation 2.2) relates the ratio of spins in the two energy levels to the difference in energy between the two levels.

$$\frac{N_\alpha}{N_\beta} = e^{-\Delta \mathrm{E}/\mathrm{k_b T}} \qquad \text{(Equation 2.2)}$$

N_α and N_β represent the number of spins in the lower and higher energy states, respectively. ΔE is the energy difference between the two energy states (equation 2.1), k_b is the Boltzmann constant, $1.381\text{x}10^{-23}\,\frac{m^2kg}{s^2K}$, and T is the absolute temperature in Kelvin (K).

When a sample is placed in a large magnetic field (B_0), the difference between the two energy states (with and against the magnetic field) forms the longitudinal magnetization vector with which we can use the classical description of NMR to continue our discussion.

2.3. Relaxation (Spin-Lattice (T_1), Spin-Spin (T_2), and T_2^* Relaxation Mechanisms)

Before continuing with the classical description of NMR, we offer an introduction to relaxation mechanisms which is necessary before we continue. When a sample is rapidly brought into the presence of a large magnetic field, the rate at which the longitudinal magnetization vector forms is in the form of an exponential function:

$$M_z(t) = M_0(1 - e^{-(t-t_{on})/T_1}) \qquad \text{(Equation 2.3)}$$

Similarly, if the sample is rapidly brought out of the presence of a large magnetic field, the decay is also an exponential function of the form:

$$M_z(t) = M_0 e^{-(t-t_{off})/T_1} \qquad \text{(Equation 2.4)}$$

This longitudinal relaxation rate is known as T_1.

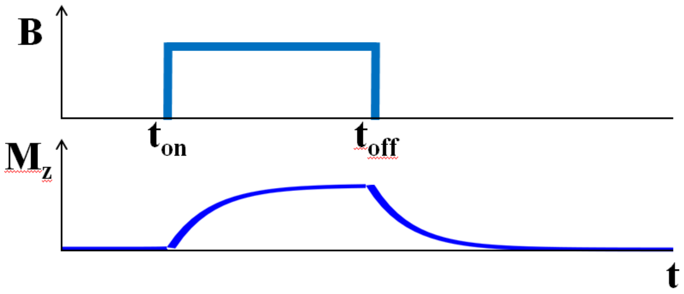

Figure 2.3. Buildup and decay of longitudinal spin magnetization. Reproduced with permission from (1).

Another relaxation mechanism that is important when studying NMR is the transverse relaxation rate, or T_2. When a spin ensemble is placed onto the transverse plane (x-y plane) using a radiofrequency pulse, the magnetization vector begins to dephase as shown in figure 2.5. The rate at which this dephasing occurs is the transverse relaxation time. This decay is governed by equation 2.5.

$$M_{xy}(t) = M_{xy}(0)e^{-t/T_2} \qquad \text{(Equation 2.5)}$$

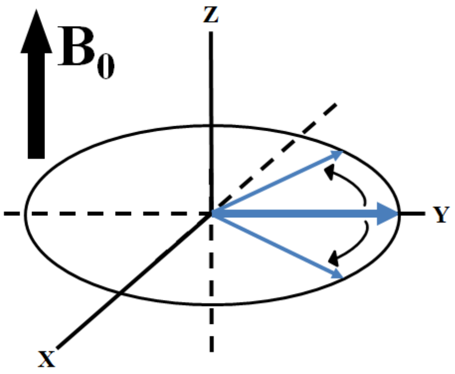

Figure 2.4. Dephasing of the magnetization vector when tipped onto transverse plane using a 90° radiofrequency pulse.

However, pure transverse (T_2) decay is only from the completely random interactions between spins, which requires a completely homogeneous main magnetic field. In reality, there are inhomogeneities in the main magnetic field and susceptibility differences in the sample that cause transverse magnetization to decay at a faster rate, known as T_2^*.

$$\frac{1}{T_2^*} = \frac{1}{T_2} + \gamma \Delta B_{inhomogeneities} \qquad \text{(Equation 2.6)}$$

2.4. The Classical Description of NMR: Bloch Equations

2.4.1. Basic Bloch Equations

Being able to treat the combined behavior of all of the spins in the system as a magnetization vector allows the use of a classical description to give a simpler picture of an NMR experiment via the Bloch Equation (2):

$$\dot{\boldsymbol{M}}(t) = \gamma \boldsymbol{M}(t) \times \boldsymbol{B}(t) \qquad \text{(Equation 2.7)}$$

When analyzing the Bloch equation in the orthogonal components, the Bloch equation can be broken down into its components including the relaxation terms:

$$\frac{dM_z}{dt} = \frac{M_0 - M_z}{T_1} \qquad \text{(Equation 2.8)}$$

$$\frac{dM_x}{dt} = \omega_0 M_y - \frac{M_x}{T_2} \qquad \text{(Equation 2.9)}$$

$$\frac{dM_y}{dt} = -\omega_0 M_x - \frac{M_y}{T_2} \qquad \text{(Equation 2.10)}$$

These Bloch equations can be solved for the magnetization evolution and relaxation to yield:

$$M_x(t) = e^{-t/T_2}(M_x(0) \cos \omega_0 t + M_y(0) \sin \omega_0 t) \qquad \text{(Equation 2.11)}$$

$$M_y(t) = e^{-t/T_2}(M_y(0) \cos \omega_0 t - M_x(0) \sin \omega_0 t) \qquad \text{(Equation 2.12)}$$

$$M_z(t) = M_z(0) e^{-t/T_1} + M_0(1 - e^{-t/T_1}) \qquad \text{(Equation 2.13)}$$

In order to detect any signal from an NMR experiment, a radiofrequency (RF) field must be used to tip the magnetization onto the transverse plane. We can model this in the rotating frame (rotation speed omega) as:

$$\vec{B}_{eff} = \left(B_0 - \frac{\omega}{\gamma}\right)\hat{z} + B_1\hat{x}' \qquad \text{(Equation 2.14)}$$

Then, the Bloch equations in the rotating frame become:

$$\frac{dM_z}{dt} = -\omega_1 M_y + \frac{M_0 - M_z}{T_1} \qquad \text{(Equation 2.15)}$$

$$\frac{dM_x}{dt} = \Delta\omega M_y - \frac{M_x}{T_2} \qquad \text{(Equation 2.16)}$$

$$\frac{dM_y}{dt} = -\Delta\omega M_x + \omega_1 M_z - \frac{M_y}{T_2} \qquad \text{(Equation 2.17)}$$

Where $\Delta\omega = \omega_0 - \omega$, and the solution to this set of differential equations is:

$$M_x(t) = e^{-t/T_2}(M_x(0)\cos\Delta\omega t + M_y \sin\Delta\omega t) \qquad \text{(Equation 2.18)}$$

$$M_y(t) = e^{-t/T_2}(M_y(0)\cos\Delta\omega t - M_x \sin\Delta\omega t) \qquad \text{(Equation 2.19)}$$

$$M_z(t) = M_z(0)e^{-t/T_1} + M_0(1 - e^{-t/T_1}) \qquad \text{(Equation 2.20)}$$

2.5. Chemical Exchange: Bloch-McConnell Equations

A unique feature of NMR is its ability to measure chemical exchange, for instance such as it is occurring between -OH, -NH, and -SH groups and the solvent water. For two exchange sites (otherwise known as a two-pool model), we begin with the simple system with two pools: pool S and pool W.

$$\mathbf{S} \underset{\mathbf{k_{WS}}}{\overset{\mathbf{k_{SW}}}{\rightleftharpoons}} \mathbf{W}$$

Where k_{SW} is the rate constant for exchange from pool S to pool W and k_{WS} is the rate constant for exchange from pool W to pool S. The concentrations of S and W can be related to the rate constants through the following equations:

$$\frac{d[S]}{dt} = -k_{sw}[S] + k_{ws}[W] \qquad \text{(Equation 2.21)}$$

$$\frac{d[W]}{dt} = k_{sw}[S] - k_{ws}[W] \qquad \text{(Equation 2.22)}$$

This is intuitive in that the differential concentration of pool S will be increased by the amount of molecules from pool W exchanged to pool S (given by the product of rate of exchange from pool W to pool S times the concentration of pool W) and decreased by the amount of molecules from pool S exchanged to W, and similarly for the differential concentration of pool W.

To describe chemical exchange in a spin system, we need to convert these concentration-based equations to reflect the magnetization of these two pools in order to add them to the Bloch equations. The equilibrium magnetization of pools S and W are directly proportional to the concentrations of pools S and W, therefore, equations 2.21 and 2.22 can be written to describe the effect of exchange on the magnetization of pool s and pool W. The chemical exchange modified Bloch equations are known as Bloch-McConnell equations named after Harden McConnell who derived them in 1958 and are given in equations 2.23-2.28 (3):

$$\frac{dM_{xs}}{dt} = -\Delta\omega_s M_{ys} - R_{2s}M_{xs} - k_{sw}M_{xs} + k_{ws}M_{xw} \qquad \text{(Equation 2.23)}$$

$$\frac{dM_{ys}}{dt} = \Delta\omega_s M_{xs} + \omega_1 M_{zs} - R_{2s}M_{ys} - k_{sw}M_{ys} + k_{ws}M_{yw} \qquad \text{(Equation 2.24)}$$

$$\frac{dM_{zs}}{dt} = -\omega_1 M_{ys} - R_{1s}(M_{zs} - M_{0s}) - k_{sw}M_{zs} + k_{ws}M_{zw} \qquad \text{(Equation 2.25)}$$

$$\frac{dM_{xw}}{dt} = -\Delta\omega_w M_{yw} - R_{2w}M_{xw} + k_{sw}M_{xs} - k_{ws}M_{xw} \qquad \text{(Equation 2.26)}$$

$$\frac{dM_{yw}}{dt} = \Delta\omega_w M_{xw} + \omega_1 M_{zw} - R_{2w} M_{yw} + k_{sw} M_{ys} - k_{ws} M_{yw} \quad \text{(Equation 2.27)}$$

$$\frac{dM_{zw}}{dt} = -\omega_1 M_{yw} - R_{1w}(M_{zw} - M_{0w}) + k_{sw} M_{zs} - k_{sw} M_{zw} \quad \text{(Equation 2.28)}$$

Where R_1 and R_2 are the longitudinal and transverse relaxation rates, M_0 is the equilibrium magnetization, and k_{sw} and k_{ws} are the exchange rates of protons from pool s to w and vice versa. Under equilibrium, the system obeys the relationship:

$$k_{sw} M_{0s} = k_{ws} M_{0w} \quad \text{(Equation 2.29)}$$

2.6. Spatial Encoding, Signal Detection, and Imaging Pulse Sequences

2.6.1. Spatial Encoding

The measurement of the precessional frequency of the longitudinal magnetization gives information about the magnetic field experienced by any ensemble of spins. If the magnetic field is varied in a controlled manner, the frequency information can yield spatial information. To demonstrate this principle, let's take the main magnetic field and add a gradient in the z-direction (G_z). Then in the z-direction, the field becomes:

$$B_z(z,t) = B_0 + zG(t) \quad \text{(Equation 2.30)}$$

The deviation from the Larmor frequency becomes linear in both z and G and can be quantified using the following equation:

$$\omega_G(z,t) = \gamma z G(t) \quad \text{(Equation 2.31)}$$

This relationship allows us to perform frequency encoding of spatial information using gradients along the z-axis and leads us to the commonly known 1D imaging equation that defines the signal s as a function of frequency.

$$s(k) = \int dz \rho(z) e^{-i2\pi kz} \quad \text{(Equation 2.32)}$$

Where ρ(z) is the spin density as a function of position along the z-axis and is being integrated over that dimension. However, for imaging in vivo systems, we need to encode a 3D volume. For a sample being excited with a set of three orthogonal gradients, we can extend the 1D imaging equation to the following (2):

$$s(\vec{k}) = \iiint dx\, dy\, dz\, \rho(x, y, z) e^{-i2\pi(k_x x + k_y y + k_z z)}$$

$$= \int d^3 r \rho(\vec{r}) e^{-i2\pi \vec{k}\cdot\vec{r}} \qquad \text{(Equation 2.33)}$$

Another way to think about slice selection and spatial encoding is to consider a sample in a large magnetic field, B_0. This sample has a Larmor frequency of γB_0. When a small linear gradient is added in the z-direction, there is spatial variation of frequencies in the z-direction. Spins on one end will precess at a faster frequency than spins on the other end. A radiofrequency pulse can be used to selectively excite a region of spins (i.e. where the precessing frequency is equal to γB_0), determined by the Fourier transform of the radiofrequency pulse. The thickness of the slice is then determined by the strength of the gradient (figure 2.5). A thicker slice can be selected with a smaller gradient (this way a larger region will have spins precessing with frequency γB_0), and a thinner slice can be selected with a larger gradient (the spatial variation of frequencies is larger so a smaller region will have spins precessing with frequency γB_0). Now that a slice has been selected (z-direction), encoding needs to be performed in the x-y plane to resolve in-plane features. Gradients can be turned on in the x-direction to perform frequency encoding, which is used to resolve features in the left right direction. This is known as frequency encoding because similar to slice selection where a gradient is turned on to modulate frequency with respect to position along the z-axis, the x-direction gradient is also used to modulate frequency in the x direction. Y-direction encoding is done by modulating the phase of the signal (known as phase encoding). The phase encoding gradient is “stepped” during the acquisition of a slice. Combined together, slice select, frequency encoding, and phase encoding gradients allow MRI to resolve samples in three dimensions.

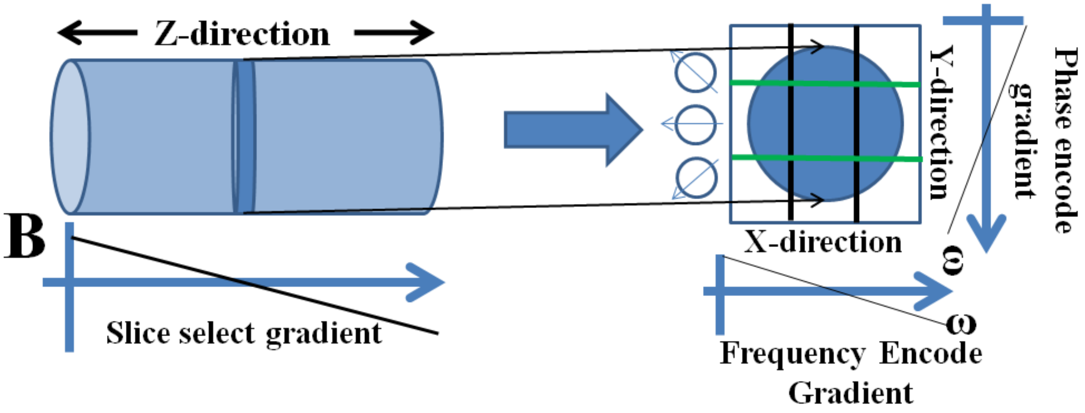

Figure 2.5. Spatial selection in MRI using slice select (z-direction), frequency encode (x-direction), and phase encode (y-direction) gradients.

2.6.2. Detection of Signal

To detect the NMR signal, an RF coil must be placed in the transverse plane, perpendicular to the main magnetic field (B_0), where an electric magnetic force (emf) is induced that is proportional to the magnetization. The signal from the coil is measured using phase sensitive detection, which records the signal on two axes, providing real and imaginary components.

2.6.3. Gradient Echo Imaging Pulse Sequence

A gradient echo sequence is one of the most common MR sequences used to acquire an image. In gradient echo imaging (see figure 2.7), a single RF pulse with flip angle α (where $\alpha \leq 90°$) is applied to tip the magnetization onto the transverse plane then a readout gradient reversal scheme with a net zero gradient integral at the echo time is used to refocus the echo. In gradient echo imaging, magnetic field inhomogeneities and susceptibility differences are not refocused and affect the imaging contrast. Therefore, it is important to have a homogeneous magnetic field when using GRE imaging. The flip angle (α) can be set to give optimized SNR using the Ernst flip angle equation:

$$\alpha = cos^{-1}(e^{-TR/T_1}) \qquad \text{(Equation 2.34)}$$

Where TR is the given repetition time, T_1 is the longitudinal relaxation time of the tissue being imaged, and α is the optimal flip angle. One way to accelerate GRE imaging is with an echo planar imaging (EPI) readout. An EPI read-out can be done by acquiring all of the lines of k-space after the excitation pulse, known as "single-shot," or by using multiple lower flip-angle excitation pulses and acquiring a few lines of k-space each time, known as "multi-shot."

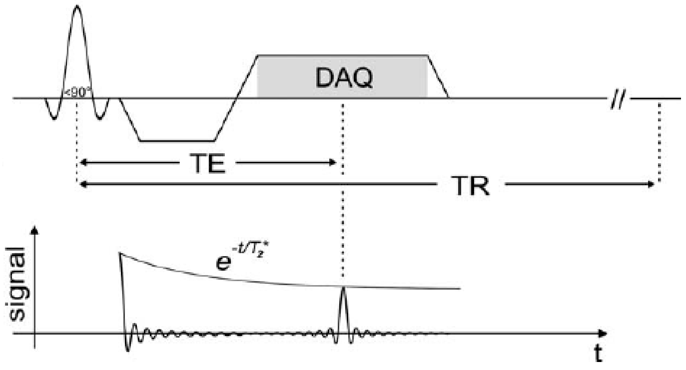

Figure 2.6. Gradient Echo Pulse Sequence Diagram (4). Reproduced with permission by the Journal of Magnetic Resonance Imaging.

In Chapter 6, I will use a multi-shot gradient-echo acquisition scheme to acquire pH-weighted images to aid physicians to make individualized treatment decisions for each patient. Furthermore, in Chapter 5, I will use a single-shot gradient echo EPI acquisition scheme to quickly acquire cerebellar blood flow-weighted images.

2.6.4. Spin Echo Imaging Pulse Sequence

One issue with the gradient echo imaging method is its sensitivity to magnetic field inhomogeneities as well as microscopic fields in the sample. One way to address these concerns is with a spin echo acquisition. A spin echo acquisition uses a 90° pulse to tilt the magnetization onto the transverse plane. When that happens, the magnetization begins to dephase due to T_2, T_2^* and $T_2^{'}$ mechanisms. A certain time later, a 180° pulse is applied to invert the direction of evolution of the magnetization. After waiting another duration of similar length, the spin echo is formed and acquired. The time from applying the 90° pulse to acquiring the spin echo is known as the echo time (TE). In order for an echo to form at that time, the 180° pulse is applied at TE/2. Figure 2.7 shows the pulse sequence diagram of a spin echo sequence.

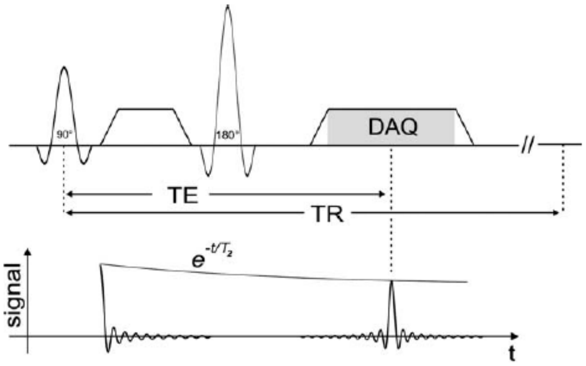

Figure 2.7. Spin Echo Pulse Sequence Diagram (4). Reproduced with permission by the Journal of Magnetic Resonance Imaging.

Equation 2.35 governs the contrast given a specific repetition time (TR) or echo time (TE) in a spin echo experiment.

$$M_z = M_0(1 - e^{-TR/T_1})e^{-TE/T_2} \quad \text{(Equation 2.35)}$$

In chapter 8, I will use the spin echo acquisition method to study exchangeable proton signals in bovine blood because of its high signal-to-noise and because it is not susceptible to local magnetic field inhomogeneities caused by deoxyhemoglobin.

2.6.5. Gradient Spin Echo (GraSE) Imaging Pulse Sequence

In gradient echo imaging, the static magnetic field must be highly homogenous, and high gradients and fast gradient switching times are also needed. Disadvantages of spin echo imaging includes a longer duration due to the presence of many 180° pulses plus high RF power deposition for the 180° pulses. One way to minimize the issues of gradient echo and spin echo imaging is by alternating the two techniques to form a gradient spin echo (or GraSE) acquisition. Figure 2.9 shows a diagram of the GraSE sequence.

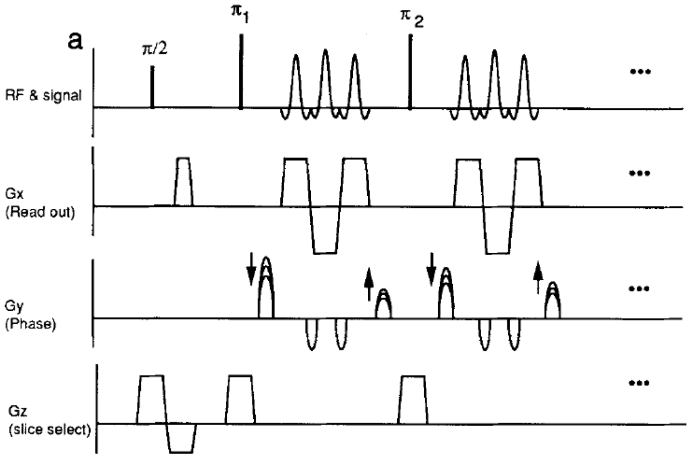

Figure 2.8. Gradient Spin Echo (GraSE) Pulse Sequence (5). Reproduced with permission from Magnetic Resonance in Medicine.

Using a GraSE acquisition scheme, multiple 180° pulses are used to refocus the magnetization to create multiple spin echoes. After each 180° pulse (each spin echo), multiple gradient recalled echoes are formed using the method described in section 2.4.2. Different speed-up factors can be achieved depending on the number of spin echoes and gradient echoes formed. The GraSE acquisition offers a unique way of acquiring true 3D images in a short amount of time. In chapter 6, we will utilize a 3D GraSE sequence to detect changes in cerebral blood volume in acute ischemic stroke patients.

2.7. Conclusion

In conclusion, magnetic resonance is a versatile tool with many ways of generating images with different contrast mechanisms in the human body. Throughout this dissertation, we will apply these basic concepts of NMR to develop novel imaging methods to study acute ischemic stroke in the human brain.

2.8. References

1. Levitt MH. Spin dynamics : basics of nuclear magnetic resonance. Chichester ; New York: John Wiley & Sons; 2001. xxiv, 686 p. p.
2. Haacke EM. Magnetic resonance imaging : physical principles and sequence design. New York: Wiley; 1999. xxvii, 914 p. p.
3. Zhou J, Wilson DA, Sun PZ, Klaus JA, Van Zijl PC. Quantitative description of proton exchange processes between water and endogenous and exogenous agents for WEX, CEST, and APT experiments. Magn Reson Med. 2004;51(5):945-52.
4. Markl M, Leupold J. Gradient echo imaging. J Magn Reson Imaging. 2012;35(6):1274-89.
5. Oshio K, Feinberg DA. GRASE (Gradient- and spin-echo) imaging: a novel fast MRI technique. Magn Reson Med. 1991;20(2):344-9.

Chapter 3. Hemoglobin, Blood, and Tissue Oxygenation

3.1. Hemoglobin

Hemoglobin is a protein responsible for the transport of oxygen in many different organisms. In humans, unique chemical and structural features of hemoglobin allow it to bind oxygen in the lungs, carry it to other parts of the body, and release it. Hemoglobin is contained inside of erythrocytes, one of the four major components (erythrocytes, leukocytes, platelets, and plasma) of blood, at a 5 mM concentration. Hemoglobin contains a four heme groups composed of an iron molecule (Fe^{2+}) in a porphyrin (a heterocyclic ring). The iron is the part of hemoglobin that binds oxygen. However, iron can only bind oxygen if it is in the reduced state (Fe^{2+}). If iron is in the oxidized state (Fe^{3+}), it is unable to bind oxygen. When this happens, methemoglobin reductase, an enzyme commonly found inside erythrocytes, will reduce the iron core to Fe^{2+} to allow it to bind oxygen again. When erythrocytes are lysed, the forward rate constant of methemoglobin reductase reduces by several fold.

3.1.1. Synthesis of Hemoglobin

The synthesis of hemoglobin requires the coordinated synthesis of heme and globin. Heme is synthesized in the mitochondria and begins with the condensation of glycine and succinyl-CoA to form 5-aminolevulinic acid (ALA), which is then transported to the cytosol where a set of reactions will produce coprophorynogen III. Then this molecule is transported back into the mitochondria to produce protoporphyrin IX, which the enzyme ferrochetalase then inserts iron to form the heme. Alpha and beta globin is synthesized from DNA on chromosomes 16 and 11, respectively, in the ribosome. After the heme is formed in the mitochondria, it exits the mitochondria to be combined with the synthesized alpha and beta globins in the cytosol.

3.1.2. Structure of Hemoglobin

When studying proteins, there are four levels of protein structure that are analyzed: the primary, secondary, tertiary, and quaternary structures. The primary structure refers to the sequence of amino acids that the protein is composed of. In the case of human hemoglobin, there are four subunits: 2 α subunits and 2 β subunits. In the alpha subunit, there are 144 amino acids, and in the beta subunit there are 146 amino acids. The secondary structure of protein refers to the alpha helices and beta pleated sheets that it has. In hemoglobin, most of the alpha subunit (75%) is hydrogen-bonded to form several alpha helices. In the beta subunit, there are eight distinct alpha helices. The tertiary structure of protein is how a single subunit of a protein folds and is usually defined by disulfide bonds. The tertiary structure of hemoglobin is such that it forms a box around the heme group, which gives the Fe^{2+} a hydrophobic environment and makes it more difficult for it to be oxidized. When hemoglobin binds oxygen, changes in the tertiary structure occur. These changes have been studied with X-ray crystallography and have been detailed extensively in his 1977 PNAS publication (1).

The quaternary structure of protein refers to how different subunits of a protein interact with each other. Hemoglobin is a tetramer because it has four subunits that interact with one another to form the entire protein. Hemoglobin is generally thought to have two main quaternary structures or states: T or tense/taut state (deoxyhemoglobin) and R or relaxed state (oxyhemoglobin) (shown in figure 1.1). In the tense state, hemoglobin has less of an affinity for oxygen than in the relaxed state. Interestingly, many people have done research on this and have identified certain structural and chemical properties that can be used to identify hemoglobin in its tense or relaxed state (2-6). Many tools have been used to elucidate physical and chemical differences between the two quaternary structures. Using ultraviolet (UV) spectra, difference spectra between T state and R state contains peaks in the aromatic region at 279, 287, 294, and 302 nm. Using UV circular dichroism, T state hemoglobin exhibits a band of negative ellipticity with a single maximum at 287 nm, and derivatives of the R structure show weak positive ellipticity in this region with slight dips at 285 nm and 290 nm. Using nuclear magnetic resonance, a characteristic of the R state is an exchangeable proton resonance 5.8 ppm downfield from water, whereas the T state has a characteristic exchangeable proton resonance 10.0 ppm downfield from water. And using SH reactivity, the rates of reaction of Cys F9 with p-mercuribenzoate are slowed by the R→T transition from the salt bridge formed between His HC3β and Asp FG1β of the T structure that shields the SH group from the reagent.

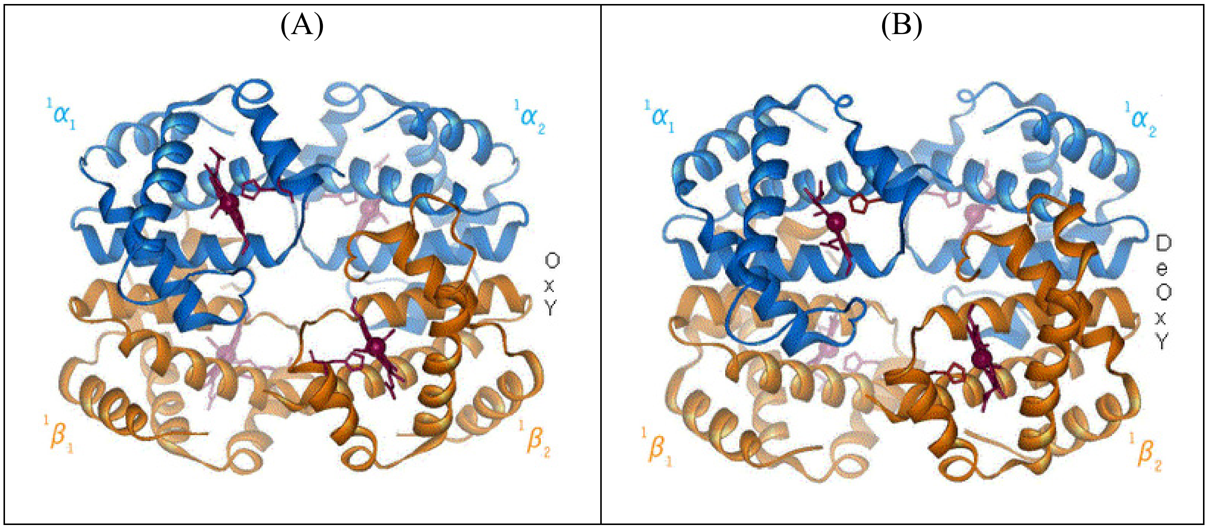

Figure 3.1. Structure of (A) Oxyhemoglobin and (B) Deoxyhemoglobin. (Source: http://en.wikipedia.org/wiki/Hemoglobin). Reproduced under the Wikimedia Commons free license.

Here we will also introduce the primary structure of bovine hemoglobin because the experiments mentioned in Chapter 7 will use bovine blood. In bovine blood, there are also four subunits: 2 α subunits and 2 β subunits. However, the bovine hemoglobin alpha subunit has 142 amino acids, and the beta subunit has 145 subunits. Secondary, tertiary, and quaternary structures of human and bovine blood are very similar. Another major difference between bovine blood and human blood is in the regulation of binding oxygen. In human blood, 2,3-bisphosphoglyceric acid (2,3-BPG) is used to regulate hemoglobin's affinity for oxygen. However, in bovine blood, this is done with chloride ions. In general, bovine blood and human blood are closely related (7) so many scientific studies substitute bovine blood for human blood (8-10).

Other than oxygen, hemoglobin is also able to bind to other molecules such as carbon monoxide (C=O). However, hemoglobin binds carbon monoxide with a binding constant of 250 times that of the binding constant to oxygen (11). Therefore, when hemoglobin binds to carbon monoxide, it causes grave toxicity because it inhibits the ability of hemoglobin to bind oxygen. Typically carbon monoxide poisoning is treated with hyperbaric oxygen therapy, which involves using putting a patient suffering from carbon monoxide poisoning in a chamber with oxygen higher than that of atmospheric pressure. It has been shown that delivery of oxygen at three times that of atmospheric pressure reduces the half life of carbon monoxide in hemoglobin to 23 minutes compared to 80 minutes at normal atmospheric pressure as well as provides delivery of oxygen through blood plasma.

When carbon monoxide binds to hemoglobin, the combined protein is known as carbonmonoxyhemoglobin (or HbCO). Although this protein is unlikely to exist in the human body at high amounts, the high binding constant of carbon monoxide relative to oxygen makes this molecule very stable and easy to study.

3.1.3. Oxygen Dissociation Curve

The oxygen dissociation curve (ODC) helps us understand how hemoglobin carries oxygen throughout our body. It relates the partial pressure of oxygen in the environment (for humans, the environment is the blood) to the oxygen saturation of hemoglobin and is defined by hemoglobin's affinity for oxygen. The ODC has a sigmoidal shape (figure 3.2A) governed by the Hill equation (Equation 1.1) that is evident for the cooperative binding of oxygen (12) (11):

$$Y = \frac{(pO_2)^n}{(pO_2)^n + (p_{50})^n}, n = 1 - 4 \qquad \text{(Equation 3.1)}$$

Where Y is the oxygen saturation fraction, p_{50} is the partial pressure of oxygen at 50% saturation, and n is the Hill's coefficient representing the number of oxygen molecules that can bind to hemoglobin. The oxygen dissociation curve can be shifted left or right depending on various factors such as pH, temperature, the partial pressure of CO_2, and 2,3-BPG (figure 3.2B).

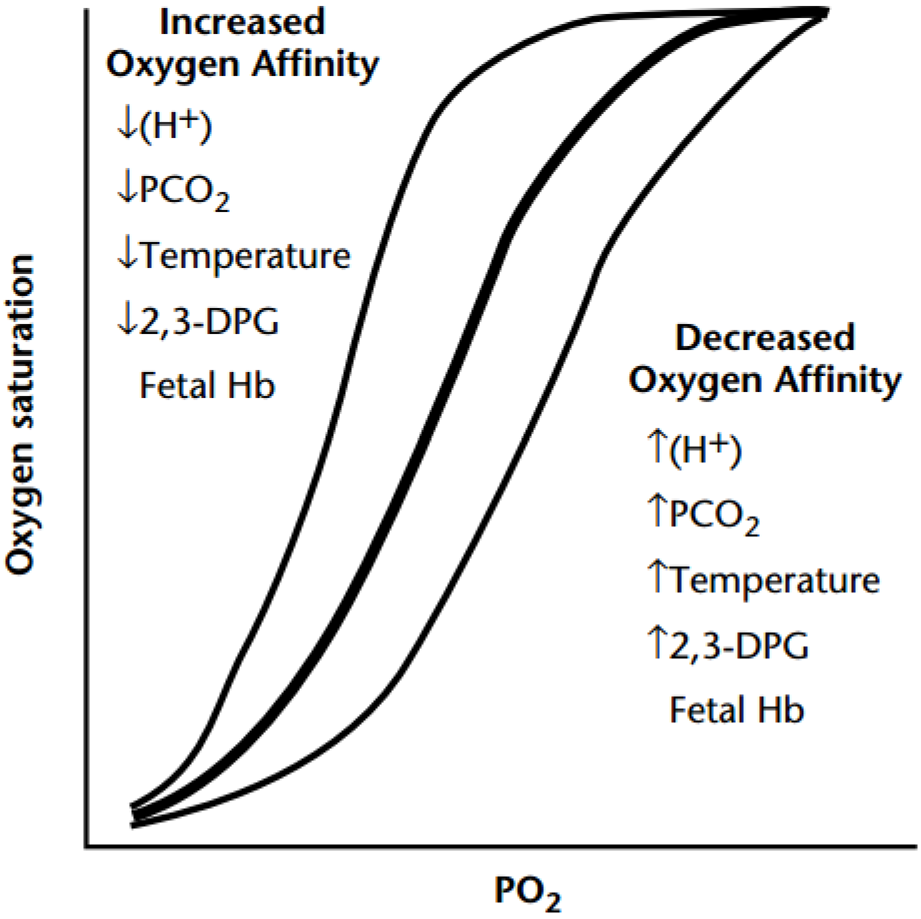

Figure 3.2. Human oxygen dissociation curve. Reproduced with permission from (12).

The average lifetime of a red blood cell is 100-120 days. After four months of push (by arteries), pull (by veins), and being squeezed through small capillaries, erythrocytes experience eryptosis, or erythrocyte programmed cell death. During this process, erythrocytes undergo changes in their plasma membranes so they can be recognized by macrophages and phagocytosed. Hemoglobin, the major constituent of a red blood cell, is broken down into heme and globin. The globin can either be recycled or broken down into its respective amino acides, which are either recycled or metabolized. Because the iron portion of the heme is valuable, it is recycled back to the bone marrow to make new heme and subsequently hemoglobin. The heme is then converted to bilirubin and bound to plasma proteins, which carries it to the liver where it is secreted as bile.

3.2. Blood, Vasculature, and Tissue Oxygenation

Blood is responsible for delivering nutrients and oxygen to the entire body. Hemoglobin, previously mentioned, is responsible for binding oxygen. Figure 3.3 shows a cartoon diagram of the circulatory system of the human body. Oxygen is breathed in at the lungs where there is a high partial pressure of oxygen enabling four oxygen molecules to bind to hemoglobin. Blood carries this oxygen to the heart where it is then pumped to the rest of the body.

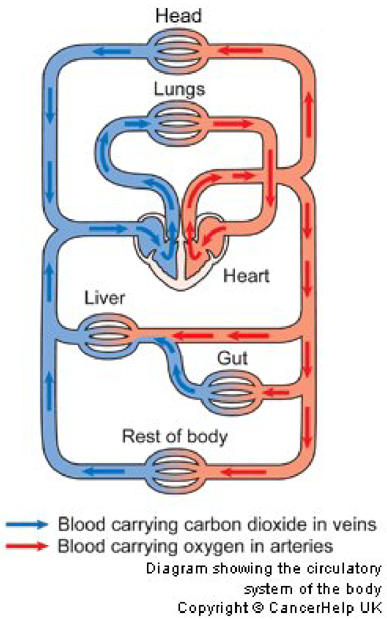

Figure 3.3. Blood Circulation in the Human Body. Taken from the patient information website of Cancer Research UK: http://www.cancerresearchuk.org/cancerhelp.

Blood leaves the heart through the aorta, a large artery, and travels through progressively smaller arteries until it reaches the arterioles, which feeds directly into the capillary network where the walls of the blood vessels are permeable for oxygen to diffuse outside and oxygenate limbs and organs. Carbon dioxide and other wastes are removed from the tissue in these capillaries and then carried through the blood stream to be disposed of by other organs. The blood flow is fastest in the aorta (~50 cm/s) after leaving the heart, but because there is only one aorta in the human body, it is only a small portion of the entire vasculature.

Blood vessels have different structural characteristics depending on the function they serve in transporting blood. The arteries, which carry blood away from the heart, accommodate flow speeds of around twice as fast as in the veins. In order to accommodate flow under pressures of 100 mmHg, arteries close to the heart such as the aorta and pulmonary arteries have thick walls containing large quantities of elastic tissue with large radii. Beyond the aorta, arteries have less elastic tissue and more muscular tissue. Following arteries, blood flows eventually flows through thinner arterioles with smooth muscle that regulates blood flow through vasodilatation or vasoconstriction. The flow of blood is slowest in capillaries where the combined surface area is largest and endothelial cell lining is thinnest (5-10 μm), which is optimal for nutrients to diffuse out to tissue and for waste products such as carbon dioxide to diffuse into the bloodstream. Capillaries then come together to form venules and eventually veins that carry deoxygenated blood back to heart and eventually the lungs to be re-oxygenated. In most people with an average heart rate of 70 times/minute and an average of 70 mL of blood pumped per beat (13), it will take one minute to pump blood around the body once (70 times/minute * 70 mL/time = 4900 mL/minute, which corresponds roughly to the 5 L of blood that each person has in their body).

3.3. Conclusion

Each person has five liters of blood in their body, and there are five million red blood cells in a milliliter. This corresponds to 25 trillion red blood cells in the human body. Also, the human brain is only 2% of the weight in a human body, yet it utilizes 20% of the resources in its metabolism. In this dissertation, we will focus on developing imaging techniques which directly or indirectly (through other parameters related to oxygenation) measure oxygenation in the brain. Therefore, this introduction is given to have a general understanding of how tissue and blood oxygenation are controlled in the human body.

3.4. References

1. Gelin BR, Karplus M. Mechanism of tertiary structural change in hemoglobin. Proc Natl Acad Sci U S A. 1977;74(3):801-5.
2. Fung LW, Ho C. A proton nuclear magnetic resonance study of the quaternary structure of human homoglobins in water. Biochemistry. 1975;14(11):2526-35.
3. Kanaori K, Tajiri Y, Tsuneshige A, Ishigami I, Ogura T, Tajima K, Neya S, Yonetani T. T-quaternary structure of oxy human adult hemoglobin in the presence of two allosteric effectors, L35 and IHP. Biochim Biophys Acta. 2011;1807(10):1253-61.
4. Ogawa S, Shulman RG. High resolution nuclear magnetic resonance spectra of hemoglobin. 3. The half-ligated state and allosteric interactions. Journal of molecular biology. 1972;70(2):315-36.
5. Mihailescu MR, Russu IM. A signature of the T ---> R transition in human hemoglobin. Proc Natl Acad Sci U S A. 2001;98(7):3773-7.
6. Lukin JA, Kontaxis G, Simplaceanu V, Yuan Y, Bax A, Ho C. Quaternary structure of hemoglobin in solution. Proc Natl Acad Sci U S A. 2003;100(2):517-20.
7. Zhao JM, Clingman CS, Narvainen MJ, Kauppinen RA, van Zijl PC. Oxygenation and hematocrit dependence of transverse relaxation rates of blood at 3T. Magn Reson Med. 2007;58(3):592-7.
8. Lu H, Xu F, Grgac K, Liu P, Qin Q, van Zijl P. Calibration and validation of TRUST MRI for the estimation of cerebral blood oxygenation. Magn Reson Med. 2012;67(1):42-9.

9. Grgac K, van Zijl PC, Qin Q. Hematocrit and oxygenation dependence of blood (1) H(2) O T(1) at 7 tesla. Magn Reson Med. 2012.

10. Hall JE, Guyton AC, ScienceDirect (Online service). Guyton and Hall textbook of medical physiology. Philadelphia, PA: Saunders/Elsevier,; 2011.

11. PROCEEDINGS OF THE PHYSIOLOGICAL SOCIETY: January 22, 1910. The Journal of Physiology. 1910;40(Suppl):i-vii.

12. Hay WW, Jr. Physiology of oxygenation and its relation to pulse oximetry in neonates. J Perinatol. 1987;7(4):309-19.

13. Curtis, Helena. Biology: 5th Edition. New York: Worth, 1989: 756.

Chapter 4. Cerebral Ischemia: Mechanism, Diagnostic Tools, and Clinical Management

4.1. Chapter Goal

The work presented throughout this dissertation relates to optimizing recently developed MRI methods and developing new MRI methods with the purpose of improving and augmenting information so physicians can make fast and accurate decisions regarding individualized patient therapy for cerebral ischemia. The goal of this chapter is three-fold:

1) Introduce ischemia, defined by Merriam-Webster dictionary as the "deficient supply of blood to a body part that is due to obstruction of the inflow of arterial blood," and describe the cascade of cellular and molecular events that unfold when ischemia occurs;
2) Introduce diagnostic imaging modalities that are currently being used by physicians to guide treatment decisions;
3) Introduce the options for treatment of ischemia.

4.2. Pathophysiology of Ischemia

4.2.1. Cellular and Molecular Response to Ischemia

Ischemia happens when a thrombus or embolus partially or totally obstructs blood flow, and subsequently oxygen delivery, to a certain part of the body. When a thrombus or embolus blocks the delivery of oxygen and glucose to the brain, multiple events occur on a cellular and molecular level. It is important to understand the effects of this process to design therapies that can protect against harmful effects and to design effective diagnostic tools using non-invasive imaging techniques to have a window into what is happening. Another reason why this is important is because research has shown that ischemia is a heterogeneous disease. Patients frequently present with different symptoms and at different time points and require different or even no treatment. Molecular pathways and mechanisms that mediate neuronal injury include glutamate-mediated excitotoxicity, increase of intracellular calcium, acidosis, secondary messenger systems, inflammatory mechanisms, free radicals, cellular apoptosis, and nitric oxide (1).

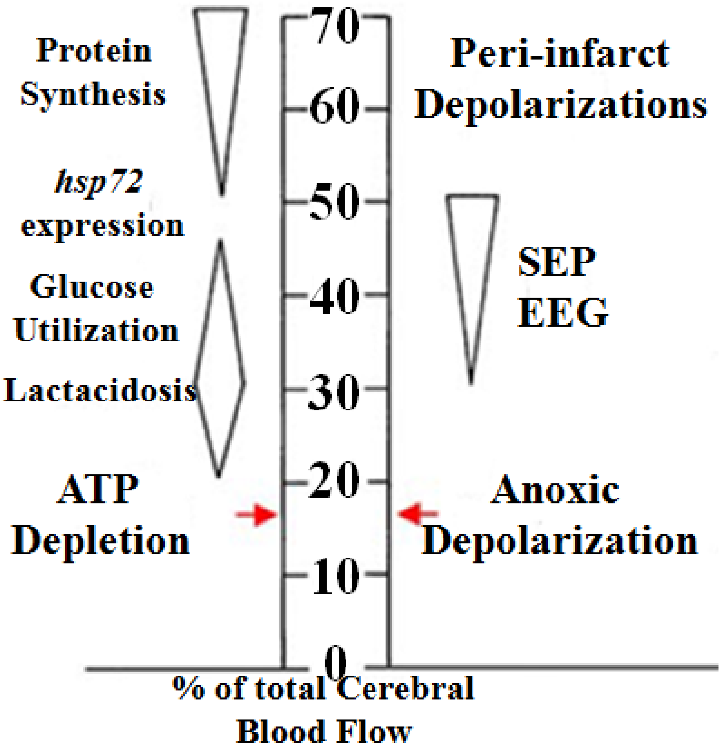

Figure 4.1. Timeline of Cellular and Molecular Events that Occur During Ischemia. SEP = somatically evoked potentials, EEG = electroencephalogram, hsp72 = heat shock protein-72. Adapted and reproduced from (2).

During early ischemia, protein synthesis is one of the first cellular functions that is affected. Furthermore, when cerebral blood flow continues to decrease, heat shock proteins (hsp) are activated. Heat shock proteins is one of the molecular hallmarks of tissue at risk of infarction because they are activated when cells are exposed to various types of stresses including abnormal temperatures, infection, inflammation, toxins, and hypoxia. In ischemia, upregulation of hsp occurs when neurons are exposed to hypoxic stresses and binds to proteins to maintain protein their structure and functionality (3).

As blood flow continues to decrease, nitric oxide (NO), another neurotransmitter and neuromodulator, is activated to help and repair the brain under ischemic conditions. NO has been identified to be produced in from three different types of protein in the brain: neuronal nitric oxide synthase (nNOS), endothelial cell-induced NOS (eNOS), and induced NOS (iNOS). As part of the autoregulatory response when cerebral perfusion is reduced, eNOS serves as a neurotransmitter to signal blood vessels to vasodilatate to increase blood flow, and subsequently the delivery of oxygen, to the brain. This temporarily increases cerebral microvascular blood volume. Contrary to the neuroprotective effects of eNOS, nNOS and iNOS have both been shown to be unfavorable to tissue outcome (3). Clinical trials have been started to investigate how the mechanisms of NO can be translated to clinical therapies (4).

Eventually, cerebral blood flow reaches a critical threshold when tissue acidosis occurs. When there is an insufficient supply of oxygen being delivered to the brain (i.e. cerebral perfusion is between 22 mL/100 g parenchyma/minute and 35 mL/100 g parenchyma/minute) (2), neurons change from aerobic respiration to anaerobic respiration. When this happens, glucose is metabolized to lactate to produce 2 adenosine triphosphate (ATP) (instead of pyruvate to produce 36 ATP under circumstances of normal cerebral perfusion), the source of molecular energy. During ischemia with normal serum glucose levels, pH may drop from its normal physiological value of 7.3-7.4 to 6.4 to 6.6. However, if cerebral perfusion is not quickly restored, then eventually plasma hyperglycemia occurs from the continual delivery of glucose, which will cause the intracellular pH to drop to 6.0.

Finally, when ATP is completely depleted, neurons do not have the means to maintain ionic gradients and anoxic depolarization occurs. This is triggered by the nonsynaptic release of glutamate that increases concentrations of extracellular glutamate. Furthermore, glutamate uptake is impaired by compromised adenosine triphosphate (ATP) production, because when the delivery of oxygen is reduced in ischemia, neurons switch from aerobic respiration to anaerobic respiration. A combination of increased extracellular glutamate and reduced glutamate uptake leads to prolonged glutamate receptor activation, which causes increased cytosolic levels of Ca^{2+}. Increased levels of Ca^{2+} can trigger lipase and protease production and other processes that lead to neuronal death.

Additionally, free radicals (reactive oxygen species (ROS) and reactive nitrogen species (RNS)), constantly being generated in cells (mostly in the mitochondria), are removed by various defense mechanisms in the body. However, it has been shown that nicotinamide adenine dinucleotidue phosphate (NADPH) oxidase generates a majority of superoxide anions during ischemia and activates N-methyl-D-aspartate (NMDA) receptors (caused by increased concentrations of glutamate) (5, 6). Furthermore, it has been validated that glutamate-activated NMDA receptors increases ROS both in neurons and vascular cells, suggesting damage by vascular ROS during ischemia. Additionally, RNS significantly impacts cellular functions by inhibiting mitochondrial enzymes, damaging DNA, and activating Poly ADP ribose polymerase (PARP), which is another one of the mechanisms that leads to cellular apoptosis.

4.2.2. Ischemic Penumbra

In acute stroke, when the brain has been deprived of oxygen for an extended of period of time, membrane ion channels fail to maintain an ionic gradient, apoptotic mechanisms initiate, water rushes into the cell, and cytotoxic edema occurs in a core region. However, it was noticed that in areas surrounding this “core” key neurological functions (e.g. protein synthesis, aerobic metabolism) are suppressed to conserve energy. In 1977, the concept known as the ischemic penumbra was proposed by Astrup as a region of tissue that was functionally silent but anatomically intact (7). However, this region of “misery perfusion” was not visualized for the first until 1981 by Baron et al using positron emission tomography (PET) imaging (8). Figure 4.2 augments figure 4.1 to approximate the flow values where the ischemic penumbra is believed to represent.

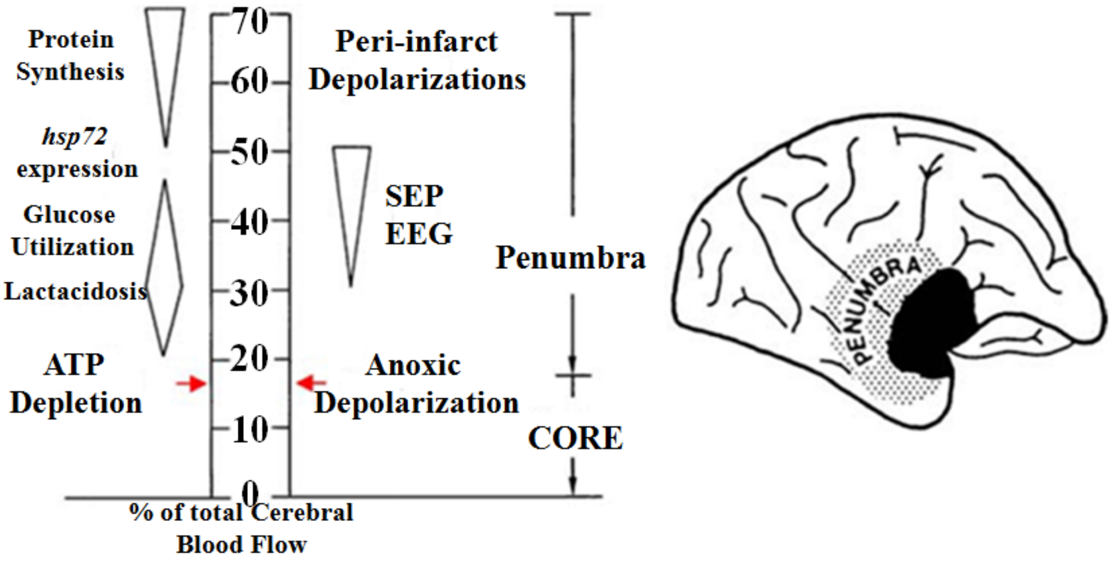

Figure 4.2. How Cellular and Molecular Events Following Ischemia Relate to the Ischemic Penumbra. Reproduced with permission from (2).

Imaging the ischemic penumbra has been a primary focus of acute stroke imaging research. In the next few sections, we will outline how imaging the ischemic penumbra has evolved over the past 30 years. Following the imaging techniques, we will introduce current treatments for ischemic stroke and explain what imaging techniques need to be developed and validated for more patients to be exposed to these treatments.

4.3. Imaging Diagnosis of Ischemic Stroke

The utility of imaging as applied to ischemic stroke arises from the necessity to determine what course of therapy is most suitable for each particular patient. Because ischemic strokes are of a heterogeneous nature, stroke therapy evolves quickly tailoring unique treatments to each unique case.

Here, we introduce the different imaging modalities that have been used to image the ischemic penumbra and guide therapeutic options for patients. We begin with positron emission tomography, the first imaging modality applied to imaging ischemic stroke, and then we move to the more popular computed tomography, where a stroke exam can be finished in 10 minutes. Finally, we introduce magnetic resonance imaging and the different contrasts it offers and how they help construct a comprehensive stroke examination.

4.3.1. Positron Emission Tomography (PET)

Positron Emission Tomography (PET), developed in 1951 and applied to humans in 1953, was the first imaging modality applied to image acute stroke to view the ischemic penumbra. It relies on the injection of a radiotracer on a biologically active molecule to measure different metabolic functions of the body (depending on which radiotracer is being injected). H_2O^{15}, more commonly known as O-15 water, is a commonly used radiotracer for measuring cerebral blood flow (CBF) with PET. Figure 4.3 shows PET images from a patient who presented with right hemiparesis (8). Here, CBF was measured using a ^{15}O-water intravenous bolus method with 20 mCi, then the patient inhaled 50 mCi $^{15}O_2$ gas in a single breath. Arterial blood sampling from a radial artery catheter yielded regional values for CBF (Figure 4.3A), cerebral metabolic rate of oxygen ($CMRO_2$) (Figure 4.3B), and oxygen extraction fraction (OEF) (Figure 4.3C).

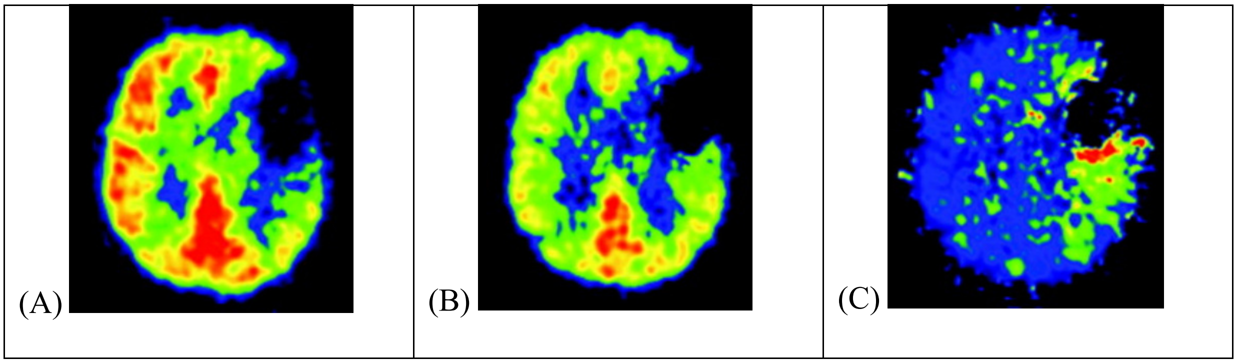

Figure 4.3. PET Imaging of Ischemic Penumbra. (A) Cerebral Blood Flow (B) Cerebral Metabolic Rate of Oxygen (C) Oxygen Extraction Fraction. Reproduced with permission from (9).

This patient has a region of the brain that has no delivery of oxygen of the brain indicated by the hypointensity in the cerebral blood flow image of figure 4.4A. A subset of the hypointensity in the cerebral blood flow image is shown to not be metabolizing oxygen in the CMRO$_2$ image of figure 4.4B. And in figure 4.4C, we see that the oxygen extraction fraction is significantly increased (red area) in the difference between the hypointensities of figure 4.4A and 4.4B and increased in other areas characterized in green. This would point out that the region that is not metabolizing oxygen has most likely irreversibly progressed to infarction (the core of the infarct). If therapy is provided to restore blood flow, then the regions in figure 4.3C denoted by red and green could possibly be salvaged (ischemic penumbra).

However, PET has a few disadvantages. First, it requires the injection of a radioactive tracer into the human body. And second, the radiotracer is not widely available and requires sophisticated equipment (^{15}O needs cyclotron) to produce.

4.3.2. Computed Tomography (CT)

Computed tomography is currently used in many emergency departments to quickly evaluate whether or not a patient is suitable for thrombolytic therapy. A typical multi-modal computed tomographic (CT) scan for an acute stroke patient takes 10 minutes and is comprised of three scans: 1) Noncontrast Head CT; 2) CT Angiography; 3) CT Perfusion. Table 4.1 summarizes each CT modality and how it is used in acute stroke diagnosis.

Table 4.1. Components of a Multimodal CT Acute Stroke Examination. (9)

Imaging Modality	**Clinical Use**
Noncontrast Head CT	- Excludes or diagnoses intracranial hemorrhage. - May identify certain stroke mimics (e.g. tumor, infection), arterial occlusion, or early signs of infarction. - Diagnoses subarachnoid hemorrhage (SAH). - Detects large ischemic strokes and infarcts.
CT Angiography	- Evaluates the intracranial and extracranial arterial circulation for occlusion or stenosis. - Evaluates for some secondary causes of intracerebral hemorrhage and vascular abnormalities in SAH (e.g. aneurysms, arteriovenous malformations).
CT Perfusion	- Quantifies cerebral blood volume, cerebral blood flow, and mean transit time for blood flow through brain tissue.

A noncontrast head CT (NCCT) is acquired on a CT scanner, which creates images using an x-ray tube mounted on one side of a rotating frame with an arc-detector on the other side. One slice is acquired when the rotating frame creates a fan beam of x-ray around the patient and detects it. This process can be repeated multiple times to acquire a volume of slices over the whole brain. CT Angiography (CTA) images are acquired by injecting an iodine-based contrast agent intravenously (typically through the arm) into the patient. This non-invasive procedure yields similar information to an angiogram, which requires a catheter to be inserted into the patient from the femoral artery to deliver contrast agent at the site of interest. CTAs reduce the risk of infection and perforation of an artery during an angiogram. CT Perfusion (CTP) images are derived by acquiring CT images also while an iodine-based contrast agent is injected intravenously into the patient. Deconvolution and other mathematical models (such as the central volume principle) can be employed to calculate maps of cerebral blood flow (CBF), cerebral blood volume (CBV), and mean transit time (MTT) based on the central volume principle. Cerebral blood volume is defined as the microvascular blood volume (introduced in section 4.2.1), the amount of blood that is in the arterioles, capillaries, and venules. As previously mentioned under conditions of reduced cerebral perfusion, cerebral autoregulatory mechanisms will release NO leading to vasodilatation of cerebral microvessels and increased cerebral blood volume. Additionally, mean transit time can be calculated as the ratio of cerebral blood volume to cerebral blood flow. Thus, MTT is a quantity with units of time and gives information about the average time it takes for blood to traverse the cerebral microvasculature. In normally perfused tissue, average mean transit times measured by CTP are around four seconds, but in ischemic regions, this can increase up to twelve seconds (11). However, the accuracy of these mathematical models and the reproducibility of CTP is currently still being debated (12).

Figure 4.4 shows state-of-the-art multimodal CT images of an acute stroke patient (13). Figure 4.4A, the noncontrast head CT image for this patient is unremarkable and shows no evidence of infarction or tissue at risk of infarction. Figure 4.4B-D show results of the perfusion CT scan, which shows reduced cerebral blood flow (CBF) (Figure 4.4B, white arrows), asymmetric cerebral blood volume (CBV) (Figure 4.4C, white arrows), and mean transit time (MTT) (Figure 4.4D) shows a region of potentially salvageable tissue (region in red surrounded by white arrows).

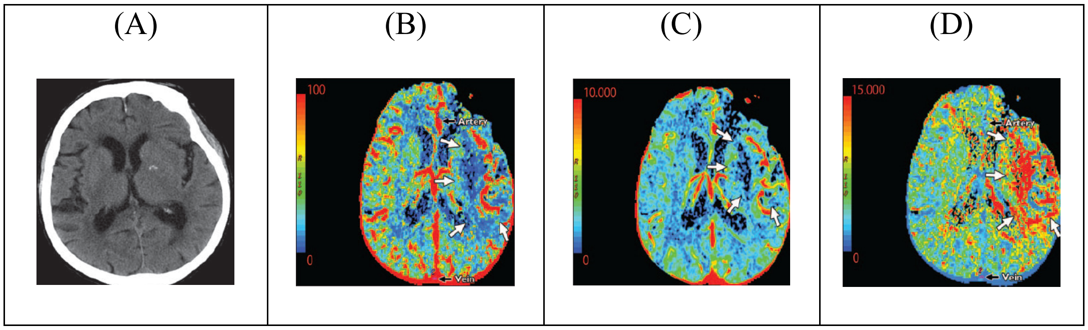

Figure 4.4. State-of-the-art Multimodal CT Images of an Acute Stroke Patient. (A) Noncontrast Head CT (B) Cerebral Blood Flow (CBF) (C) Cerebral Blood Volume (CBV) (D) Mean Transit Time (MTT). Reproduced with permission from (12).

4.3.3. Magnetic Resonance Imaging (MRI)

Although it has not yet reached a mainstream diagnostic tool for ischemic stroke, magnetic resonance imaging (MRI) has a lot of information to offer to doctors who are deciding what course of treatment to give a patient and how that treatment is progressing. Two major benefits MRI offers to the acute stroke field are: 1) non-ionizing radiation and 2) a myriad of contrast mechanisms. Unlike CT and PET, MRI scans do not leave patients with traces of harmful ionizing radiation. Additionally, MRI offers a plethora of different contrast mechanisms by varying how radiofrequency (rf) pulses are played out (or pulse sequence). A few examples of MRI contrasts that are currently used in the diagnosis of acute ischemia include

FLuid Attenuated Inversion Recovery (FLAIR), GRadient Echo (GRE), Magnetic Resonance Angiography (MRA), Diffusion Weighted Imaging (DWI), and Perfusion Weighted Imaging (PWI). Table 4.2 outlines a few of the modalities that are commonly used to image acute stroke patients and the clinical relevance of those scans.

Table 4.2. Multimodal MRI Acute Stroke Protocol Used at Johns Hopkins Hospital.

Imaging Modality	**Clinical Use**
Diffusion-Weighted Imaging (DWI)	- Assess for dense cerebral ischemia and likely cerebral infarction.
Gradient Recalled Echo (GRE)	- Assess for cerebral microbleeds. - Rule out intracerebral hemorrhage.
Perfusion-Weighted Imaging (PWI)	- Assess for cerebral ischemia and extent of tissue at risk of infarction.
Magnetic Resonance Angiography (MRA)	- Assess for intracranial vessel occlusion.
Fluid Attenuated Inversion Recovery (FLAIR) or T_2-Weighted Imaging	- Assess for extent of infarcted tissue, small vessel disease, and prior territorial infarction. - Rule out subarachnoid hemorrhage.

Diffusion-weighted imaging (DWI) uses the addition of field gradients to an MRI acquisition to sensitize it to water diffusion (14). This is mostly done using spin echo acquisition, but other approaches are also possible. In acute stroke, DWI is particularly useful to visualize regions of the brain in which there is insufficient energy (ATP) to maintain cellular ion channel patency and cytotoxic edema has occurred. Because of DWI's sensitivity to imaging water diffusion, regions where cytotoxic edema have occurred have more restricted water diffusion on average, and these regions appear hyperintense in diffusion-weighted images where the strength of the gradient is high. An example of this can be seen in figure 4.5A. Recent research has shown that hyperintense regions on diffusion-weighted images in acute stroke patients progress to infarction. This has led to the use of DWI to visualize the "core" of the stroke.

Dynamic susceptibility contrast perfusion-weighted imaging (DSC-PWI) tracks the injection of a gadolinium-based contrast agent that changes the relaxation properties of the tissue it passes through. As the contrast agent passes through the tissue of interest (in stroke, it is the brain), images are rapidly acquired (15, 16). Through equations that relate signal intensity to relaxation (T_2^*) and using the central volume principle, the data then can be reconstructed to yield maps of cerebral blood volume (CBV), cerebral blood flow (CBF), mean transit time (MTT), and time-to-peak (TTP). These images can then be used to map regions of reduced perfusion. The combination of hyperintensities in diffusion-weighted and perfusion-weighted images (known as the diffusion-perfusion mismatch (DPMM)) can yield information on the ischemic penumbra (figure 4.5A and figure 4.5B). Unfortunately, studies have analyzed the effectiveness of using the DPMM to evaluate treatment options for stroke patients and found that DSC-PWI frequently overestimates the tissue at risk of infarction (17).

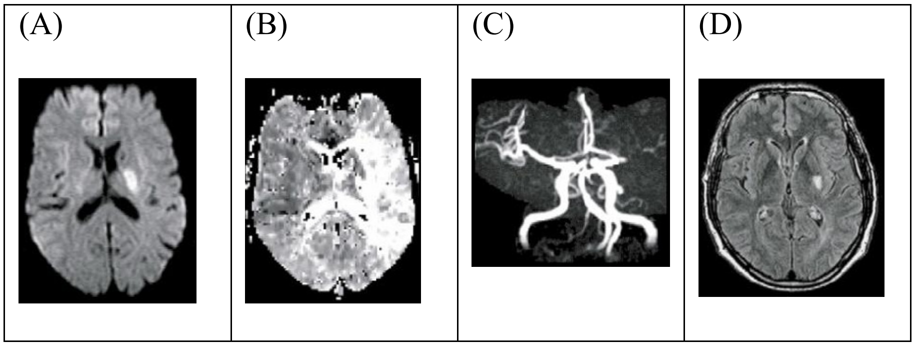

Figure 4.5. Multimodal MRI of an Acute Stroke Patient illustrating ischemic penumbra with diffusion-perfusion mismatch. (A) Diffusion-weighted Image shows a small lesion (hyperintensity) in the deep middle cerebral artery vascular territory. (B) Hyperintensity in Time-to-Peak weighted Image (calculated from Perfusion-Weighted Imaging) and (C) Magnetic Resonance Angiography show complete occlusion of the left middle cerebral artery territory. (D) Fluid-Attenuated Inversion Recovery showing final infarct. Reproduced with permission from (18).

In addition to not being effective at estimating tissue at risk of infarction, it has recently been observed that a small group patients with compromised kidney function who had received one or more exposures to gadolinium-based contrast agents (GBCA) from DSC-PWI develop nephrogenic systemic fibrosis (NSF), a fibrosing disease that mainly affects the skin and subcutaneous tissues but can also affect other organs too. Currently, there is no effective treatment for this disease, which has been fatal to some patients. Thus a set of recommendations have been developed that advises doctors not to administer gadolinium-based contrast agents to patients with a glomerular filtration rate (GFR) of less than 30 ml/min/1.73m^2 (19). Therefore, it is important to develop non-invasive techniques with higher sensitivity to detect tissue at risk of infarction. This will be done in Chapter 5, where we will use a non-invasive method to measure cerebral blood volume and apply this method to acute ischemic stroke patients to study whether relative increases in cerebral blood volume is a good indicator of tissue that may progress to infarction. We will also introduce another non-invasive method in Chapter 6 where we will use pH-weighted imaging to study pH changes in acute ischemia.

4.4. Clinical Management of Cerebral Ischemia

Before imaging technologies were available, acute stroke was deemed an untreatable disease where physicians could only make patients as comfortable as possible while they waited for patients to stabilize. Now, doctors, equipped with multiple imaging modalities and with blood thinners and clot busting agents at their side, can manage the disease as it progresses. Currently, the three most commonly used therapies include intravenous tissue plasminogen activator (IV-tPA), intra-arterial tPA (IA-tPA), and mechanical thrombectomy where devices are used to mechanically retrieve the clot.

4.4.1. Intravenous Tissue Plasminogen Activator (IV-tPA)

Tissue plasminogen activator (or tPA) is a protein involved in breaking down blood clots. It catalyzes the conversion of plasminogen to plasmin, the main enzyme responsible for the breakdown of clots to fibrin degradation products (FDPs).

Currently, tPA is the only approved drug by the United States Food and Drug Administration (USFDA) for thrombolysis of the blood clot, and it is only approved for usage within a three hour window. This means that patients must present within three hours of onset of ischemic stroke symptoms and have the contraindications of tPA ruled out in order to be eligible to receive tPA. In reality, less than 5% of patients that present with acute ischemic stroke receive tPA although many more patients could benefit from it. One disadvantage of tPA is that it causes hemorrhage in 5% of the patients that it is used in. Therefore, it is extremely important to have diagnostic tools that accurately identify patients who can benefit from tPA.

4.4.2. Intra-arterial tPA (IA-tPA)

Intra-arterial administration of thrombolytic agents offer a higher concentration of drug delivery to the therapeutic site and open the treatment window from three (treatment by IV-tPA) to six hours. IA-tPA is also used for patients who have recently had surgery or are on blood thinners. The procedure for IA-tPA begins by inserting a catheter in the groin area and threads it up to the brain. Then tPA is administered locally to break up the clot, and pieces of the clot are then physically removed from the brain using a device integrated with the catheter. Because IA-tPA requires the insertion of a catheter, IA-tPA is more invasive than IV-tPA.

4.4.3. Mechanical Thrombectomy

Beyond the tPA therapeutic windows (> 6 hours) for thrombolytic therapy, many stroke physicians have turned to mechanical thrombectomy. Currently, there are two FDA-approved devices in the United States. One of them is known as the Merci retriever device that is composed of a wire in a spring device that is positioned distal to the thrombus, then it is mechanically used to extract the thrombus from the vessel. The other device is called the penumbra system, which is used to break up the clot and aspirate the pieces through a reperfusion catheter connected to a vacuum system. Mechanical thrombectomy is the most invasive treatment.

4.5. Clinical Trials

A clinical trial, Echoplanar Imaging Thrombolysis Evaluation Trial (EPITHET), has been performed to evaluate the benefit of giving intravenous tissue plasminogen activator beyond the currently FDA-approved three hour window (19). Diffusion and Perfusion Imaging Evaluation for Understanding Stroke Evolution (DEFUSE) (20) and Diffusion and Perfusion Imaging Evaluation for Understanding Stroke Evolution-2 (DEFUSE-2) (21), are two clinical trials that have evaluated whether patients with diffusion-perfusion mismatch selectively treated with iv-TPA would have a favorable clinical outcome.

EPITHET was a double-blind clinical trial that studied whether iv-TPA was effective for patients with a DPMM beyond three hours of stroke onset. To test this hypothesis, a one hundred and one patients were enrolled and stratified into two groups: fifty-two patients received the thrombolytic agent, and forty-nine patients received a placebo three to six hours after onset of ischemic stroke. Patients were scanned on a 1.5T MRI machine with standard DWI, PWI, and MRA sequences. Imaging mismatch was defined as a perfusion to diffusion lesion ratio of 1.2 and at least a 10 mL PWI and DWI lesion volume. Reperfusion was defined as a greater than 90% attenuation of the PWI lesion between baseline and day three. A good neurological outcome was defined as a National Institutes of Health Stroke Scale of 0 or 1 at day 90 or improvement of eight or more points from baseline. A good functional outcome was defined as a modified Rankin Score at day 90 of zero to two. The primary hypothesis was patients with imaging mismatch who received iv-TPA would have larger attenuation of infarct growth. The primary method of analysis was the ratio of the geometric mean (defined as the exponential of mean log relative growth). Secondary methods of analyses included relative growth, absolute growth, and difference in cube root lesion volumes. A secondary hypothesis was that patients with imaging mismatch who received iv-TPA were more likely to reperfuse and achieve good neurological and functional outcome. Data were analyzed before revealing treatment allocation. When analyzing the data using the primary method of analysis, the authors negatively concluded (primary hypothesis) lower infarct growth in mismatch patients with iv-TPA. However, secondary methods of analyses support the primary hypothesis that iv-TPA can reduce infarct growth beyond three hours. With regards to the second hypothesis, the authors concluded that occurrence of reperfusion was significantly higher in the patients with mismatch who received iv-TPA than in those who received the placebo. However, the occurrence of good neurological and functional outcome did not differ between treatment groups. In conclusion, intravenous tissue plasminogen activator increased reperfusion in patients who presented three to six hours after symptom onset and was strongly associated with a reduction of infarct growth and good neurological and functional outcome.

The authors of the DEFUSE clinical trial hypothesized and confirmed that patients with a DPMM profile who received iv-TPA had a more favorable clinical outcome (20). In this trial, seventy-five patients were enrolled between April 2001 and April 2005. Patients were divided into four different categories based on the presentation of their DPMM: 1) A "Mismatch" profile was defined by a presentation of the PWI lesion that was 120% or greater and 10 mL or more of the DWI lesion. A subset of this group who did not have a PWI lesion of 100 mL or more with a T_{max} delay of eight seconds or longer was known as the "Target Mismatch" profile; 2) Patients with a DPMM who did have a PWI lesion of 100 mL or more with a T_{max} of eight seconds or longer were categorized as the "Malignant" profile; 3) A "Small Lesion" profile was established by DWI and PWI lesions of less than 10 mL; and 4)

A “No Mismatch” profile was defined by a PWI lesion volume of less than 120% of the DWI lesion volume. Of the fifty-four percent of patients with a “Mismatch” profile, fifty-six percent had a favorable clinical response with early reperfusion (defined as a 30% or greater and 10 mL or more reduction in the PWI lesion volume on the three to six hour follow-up scan) versus nineteen percent who did not have a favorable clinical response. It was also observed that patients with a “Small Lesion” profile typically had favorable clinical outcomes. Of the patients with a “No Mismatch” profile, none of the four patients with early reperfusion had a favorable clinical response compared to five out of seven patients who did not have early reperfusion. Furthermore, early reperfusion in “Target Mismatch” patients were associated with a favorable clinical outcome in sixty-seven percent of patients compared to nineteen percent who did not have early reperfusion. The three patients with a “Malignant” profile that received early reperfusion all had symptomatic intracranial hemorrhages and died. The authors concluded that acute MRI scans are able to identify patients that could potentially benefit from early reperfusion therapies from patients who are unlikely to benefit or may even be harmed.

In DEFUSE-2, investigators studied whether MRI can aid in identifying patients who could potentially benefit from endovascular stroke treatment (21). A hundred and four patients were studied from eight centers in the United States and one in Austria between July 2008 and September 2011. MRI scans were taken before treatment, within twelve hours of revascularization, and five days after treatment. The target DPMM was defined as a ratio of 1.8 or more between the volume of the perfusion lesion (defined as $T_{max} > 6$ s) and the volume of the diffusion lesion (defined as an apparent diffusion coefficient of less than 600×10^{-6} mm^2/s) and. A patient was considered to have early reperfusion if they had more than 50% reduction in the volume of the perfusion-weighted MRI lesion between baseline and follow-up. A favorable clinical response was defined as an improvement in the NIHSS score of eight points or more between the baseline and day thirty score. Similar to the DEFUSE trial, the authors concluded that pre-treatment (or baseline) MRI data with automated imaging analysis software can be used to stratify ischemic stroke patients into two groups: 1) patients with the target DPMM who received reperfusion had significantly better clinical outcomes than those who did not receive reperfusion; and 2) patients with no target mismatch who show no correlation between those who did or did not receive reperfusion.

4.6. Conclusion

In conclusion, because of the current availability of several treatment options for acute stroke, one has the need for imaging methods that can accurately determine the optimal course of treatment on a per patient basis. Issues that complicate this include the heterogeneity of how acute ischemic stroke presents, the time limitation of treatment options available, and the invasiveness of treatment options. Newer imaging techniques are being developed to yield more specific information so physicians can make informed decisions on how patients can be treated. In this dissertation, we will investigate how we can apply advanced imaging techniques to non-invasively image the ischemic penumbra via cerebral blood volume information (Chapter 6), tissue acidosis information (Chapter 7) and how we can possibly develop new techniques sensitive to tissue oxygenation (Chapter 8).

4.7. References

1. Barnett HJM. Stroke : pathophysiology, diagnosis, and management. 3rd ed. New York: Churchill Livingstone; 1998. xxiv, 1459 p., 12 p. of plates p.
2. Hossmann KA. Pathophysiology and therapy of experimental stroke. Cellular and molecular neurobiology. 2006;26(7-8):1057-83.
3. Hata R, Mies G, Wiessner C, Hossmann KA. Differential expression of c-fos and hsp72 mRNA in focal cerebral ischemia of mice. Neuroreport. 1998;9(1):27-32.
4. Glyceryl trinitrate vs. control, and continuing vs. stopping temporarily prior antihypertensive therapy, in acute stroke: rationale and design of the Efficacy of Nitric Oxide in Stroke (ENOS) trial (ISRCTN99414122). International journal of stroke : official journal of the International Stroke Society. 2006;1(4):245-9.
5. Girouard H, Wang G, Gallo EF, Anrather J, Zhou P, Pickel VM, Iadecola C. NMDA receptor activation increases free radical production through nitric oxide and NOX2. J Neurosci. 2009;29(8):2545-52.
6. Brennan AM, Suh SW, Won SJ, Narasimhan P, Kauppinen TM, Lee H, Edling Y, Chan PH, Swanson RA. NADPH oxidase is the primary source of superoxide induced by NMDA receptor activation. Nature neuroscience. 2009;12(7):857-63.
7. Astrup J, Symon L, Branston NM, Lassen NA. Cortical evoked potential and extracellular K+ and H+ at critical levels of brain ischemia. Stroke. 1977;8(1):51-7.
8. Baron JC, Bousser MG, Rey A, Guillard A, Comar D, Castaigne P. Reversal of focal "misery-perfusion syndrome" by extra-intracranial arterial bypass in hemodynamic

cerebral ischemia. A case study with 15O positron emission tomography. Stroke. 1981;12(4):454-9.

9. Sobesky J, Zaro Weber O, Lehnhardt FG, Hesselmann V, Neveling M, Jacobs A, Heiss WD. Does the mismatch match the penumbra? Magnetic resonance imaging and positron emission tomography in early ischemic stroke. Stroke. 2005;36(5):980-5.

10. Nentwich LM, Veloz W. Neuroimaging in acute stroke. Emergency medicine clinics of North America. 2012;30(3):659-80.

11. Kamena A, Streitparth F, Grieser C, Lehmkuhl L, Jamil B, Wojtal K, Ricke J, Pech M. Dynamic perfusion CT: optimizing the temporal resolution for the calculation of perfusion CT parameters in stroke patients. European journal of radiology. 2007;64(1):111-8.

12. Zussman BM, Boghosian G, Gorniak RJ, Olszewski ME, Read KM, Siddiqui KM, Flanders AE. The relative effect of vendor variability in CT perfusion results: a method comparison study. AJR Am J Roentgenol. 2011;197(2):468-73.

13. Lui YW, Tang ER, Allmendinger AM, Spektor V. Evaluation of CT perfusion in the setting of cerebral ischemia: patterns and pitfalls. AJNR Am J Neuroradiol. 2010;31(9):1552-63.

14. Le Bihan D, van Zijl P. From the diffusion coefficient to the diffusion tensor. NMR Biomed. 2002;15(7-8):431-4.

15. Ostergaard L, Weisskoff RM, Chesler DA, Gyldensted C, Rosen BR. High resolution measurement of cerebral blood flow using intravascular tracer bolus passages. Part I: Mathematical approach and statistical analysis. Magn Reson Med. 1996;36(5):715-25.

16. Ostergaard L, Sorensen AG, Kwong KK, Weisskoff RM, Gyldensted C, Rosen BR. High resolution measurement of cerebral blood flow using intravascular tracer bolus passages. Part II: Experimental comparison and preliminary results. Magn Reson Med. 1996;36(5):726-36.

17. Kucinski T, Naumann D, Knab R, Schoder V, Wegener S, Fiehler J, Majumder A, Rother J, Zeumer H. Tissue at risk is overestimated in perfusion-weighted imaging: MR imaging in acute stroke patients without vessel recanalization. AJNR Am J Neuroradiol. 2005;26(4):815-9.

18. Muir KW, Buchan A, von Kummer R, Rother J, Baron JC. Imaging of acute stroke. Lancet Neurol. 2006;5(9):755-68.

19. Leiner T, Kucharczyk W. NSF prevention in clinical practice: summary of recommendations and guidelines in the United States, Canada, and Europe. J Magn Reson Imaging. 2009;30(6):1357-63.

20. Davis SM, Donnan GA, Parsons MW, Levi C, Butcher KS, Peeters A, Barber PA, Bladin C, De Silva DA, Byrnes G, Chalk JB, Fink JN, Kimber TE, Schultz D, Hand PJ, Frayne J, Hankey G, Muir K, Gerraty R, Tress BM, Desmond PM. Effects of alteplase beyond 3 h after stroke in the Echoplanar Imaging Thrombolytic Evaluation Trial (EPITHET): a placebo-controlled randomised trial. Lancet Neurol. 2008;7(4):299-309.

21. Albers GW, Thijs VN, Wechsler L, Kemp S, Schlaug G, Skalabrin E, Bammer R, Kakuda W, Lansberg MG, Shuaib A, Coplin W, Hamilton S, Moseley M, Marks MP. Magnetic resonance imaging profiles predict clinical response to early reperfusion: the

diffusion and perfusion imaging evaluation for understanding stroke evolution (DEFUSE) study. Ann Neurol. 2006;60(5):508-17.

22. Lansberg MG, Straka M, Kemp S, Mlynash M, Wechsler LR, Jovin TG, Wilder MJ, Lutsep HL, Czartoski TJ, Bernstein RA, Chang CW, Warach S, Fazekas F, Inoue M, Tipirneni A, Hamilton SA, Zaharchuk G, Marks MP, Bammer R, Albers GW. MRI profile and response to endovascular reperfusion after stroke (DEFUSE 2): a prospective cohort study. Lancet Neurol. 2012;11(10):860-7.

Chapter 5: Assessing Cerebral Blood Volume Changes in Acute Ischemic Stroke Patients Using Magnetization Transfer-Enhanced Vascular Space Occupancy (MT-VASO)

5.1. Abstract

It is widely known that thrombolytic therapy (intravenous tissue plasminogen activator, tPA) if given quickly after the occurrence of an ischemic stroke can significantly improve clinical outcome. To evaluate whether a candidate should receive thrombolytic therapy, the diffusion-perfusion mismatch based on magnetic resonance imaging can be used. However, the region of reduced perfusion that is at risk of infarction is frequently overestimated with current gadolinium-based perfusion weighted imaging. Recent literature has shown that increased cerebral blood volume (CBV) may be a marker for salvageable tissue in acute ischemia patients. The hypothesis is that, following an occlusion, the body's autoregulatory mechanism will allow blood vessels in the affected region to vasodilatate to accommodate for more blood to be transported to the area. However, over time these blood vessels will exhaust their capacity and collapse.

Vascular Space Occupancy (VASO) MRI uses blood nulling to asses changes in CBV. In this study, we explore the feasibility of using magnetization transfer-enhanced VASO MRI as a diagnostic tool for evaluating the ischemic penumbra, or salvageable region, in acute stroke patients. Data for this technique is presented for three patients. Initial analysis shows that this technique is able to capture a larger region of tissue that eventually progresses to infarction, but is not as well localized as gadolinium-based mean transit time and time to

peak maps. Other drawbacks of the technique include that analysis is currently limited to white matter and can be confounded by changes in longitudinal relaxation times.

5.2. Introduction

Stroke, the third leading cause of death and leading cause of disability, affects approximately fifteen million people each year in the world (1). Acute ischemic stroke, caused by the occlusion of cerebral blood vessels by an arterial embolus or thrombus, accounts for approximately 85% of cases (2). A number of studies have shown that thrombolytic treatment with intravenous tPA to restore blood flow can be useful for reducing tissue infarction when given within the first 3-6 hours post-onset (3). However, the benefit of tPA must be weighed against the risk of intracranial hemorrhage (4-6), which occurs in approximately 6% (7) of cases in which patients are treated with tPA and frequently leads to irreversible damage. The ability to quickly and accurately assess whether patients have salvageable ischemic tissue is critical to improving functional outcome and minimizing long-term disability.

tPA has a number of contraindications for its usage (8). The most important one is evidence of hemorrhage, which can be assessed by CT or MRI. Of these, CT is faster, but MRI is more versatile in that it offers other contrasts. Diffusion-weighted imaging (DWI) and dynamic susceptibility contrast-based perfusion-weighted imaging (PWI) are MRI-based scans that are frequently used to evaluate whether a patient would be a good candidate for tPA. Specifically, DWI is able to portray regions where disruption of the cellular membrane potential has occurred. This corresponds to tissue that is likely to progress to infarction, even though exceptions are known to occur. DSC PWI employs the use of an exogenous gadolinium-based tracer; following the tracer as a function of time allows for qualitative assessment of mean transit time (MTT), time to peak (TTP), cerebral blood flow (CBF), and cerebral blood volume (CBV) (9, 10). All of the parametric maps derived from the PWI scan can be used to determine regions of the brain that are functionally intact but potentially at risk of infarction if the ischemia is not reversed. These regions are indicators of the suitability for thrombolytic treatment with tPA. Thus, the DWI/PWI mismatch, or "perfusion penumbra," can be used in principle to assess the extent of tissue that is ischemic but has not yet proceeded to infarction. However, the actual ischemic penumbra, or region at true risk of infarction, is not always easy to identify from the DWI/PWI mismatch. There have been numerous reports that the penumbra defined by PWI frequently overestimates the actual region at risk (11). This is because reductions in perfusion imaged with PWI span over two regions: (1) an oligemic region that contains benign reductions in blood flow that will eventually revert to normal perfusion, and (2) a region that, if left untreated, will progress to infarction. Recent evidence has shown that microvascular CBV (12-15) changes in the early stages of ischemia. During ischemia, microvascular CBV adjusts as a consequence of blood pH reduction (16, 17), which lead to relaxation of smooth muscle cells and vasodilatation (increased CBV).

Vascular Space Occupany (VASO) MRI is an inversion recovery-based sequence where the inversion time (TI) is equal to the nulling time of blood, and at that time while blood magnetization is zero, the magnetization of parenchyma is slightly positive (18). Figure 5.1 shows an image of the VASO pulse sequence and a graph that shows how much each spin ensemble has recovered when blood is nulled.

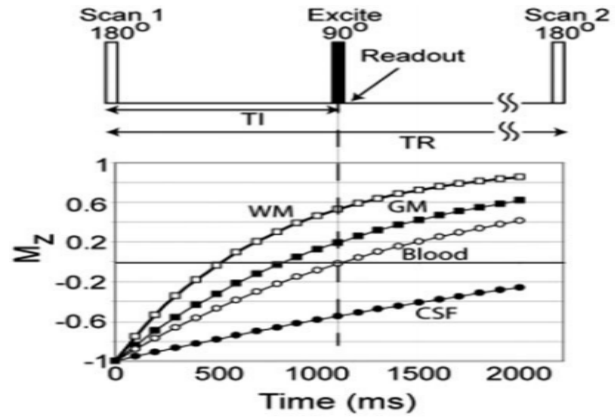

Figure 5.1. VASO MRI Pulse Sequence. Reproduced with permission from (19).

VASO has been used to assess CBV changes in fMRI, Alzheimer's disease, carotid artery stenosis patients, and leukoaraiosis (18, 20-22). One major disadvantage of VASO is its low signal-to-noise ratio (SNR). Magnetization Transfer-Enhanced VASO (MT-VASO) uses a magnetization transfer pulse at an offset far away from the center frequency of water to reduce the tissue magnetization before the inversion pulse to increase SNR by 40-50% (23). In this study, we used MT-VASO to acquire images weighted by CBV.

Our hypothesis is that patients with regions of increased CBV have not yet exhausted autoregulatory mechanisms and could benefit from thrombolysis. Here we explore the feasibility of using Magnetization Transfer (MT-VASO) to visualize tissue at risk of infarction in acute cerebral ischemia patients in a clinically feasible time frame. MT-VASO may provide a two-prong benefit to current methods for looking at the ischemic penumbra: (1) MT-VASO is a non-invasive MRI technique, while numerous studies have linked occurrences of nephrogenic systemic fibrosis (NSF) to use of gadolinium-based contrast agents in kidney patients (24). (2) MT-VASO will not highlight regions of benign oligemia.

5.3. Materials and Methods

5.3.1. Simulations

Simulations were performed using the VASO model described in Donahue et al (19) to determine how the VASO signal intensity would change for various increases in microvascular CBV. Modifications for the MT pulse from Hua et al (23) were added to account for the effects of the magnetization transfer (MT) pulse. Parameters for the simulation are listed in Table 5.1. The total MRI signal (S_{total}) in Equation 5.1 can be described using a three-compartment (gray matter parenchyma (S_{GM}), white matter parenchyma (S_{WM}), CSF (S_{CSF})) slow-exchange biophysical model.

$$S_{total} = (1 - X_{WM} - X_{CSF}) \cdot S_{GM} + X_{WM} \cdot S_{WM} + X_{CSF} \cdot S_{CSF} \qquad \text{(Equation 5.1)}$$

$$S_i \sim (C_i - CBV_i \cdot C_b) \cdot M_i^{NS}(TR,TI) \cdot e^{-\frac{TE}{T_{2,i}}} + CBV_i \cdot C_b \cdot M_b^{NS}(TR,TI) \cdot e^{-\frac{TR}{T_{2,b}}},$$

$$i = GM, WM \qquad \text{(Equation 5.2)}$$

where *b* is blood, $M^{NS}(TR,TI)$ is the longitudinal magnetization after non-selective (NS) inversion, T_2 is the transverse relaxation time, and *CBV* is the CBV fraction in units of ml blood/ml parenchyma (VASO units). The units for MR signal are magnetization/ml tissue for a given voxel, based on the units of *M* (magnetization/ml water), *X* (dimensionless), and the water density *C* (ml water/ml tissue).

The Bloch equations can be simulated to account for the effect of reducing the tissue magnetization with the MT pulse ($MT_{pulse,GM/WM}$) before the non-selective inversion.

$$\frac{dM_z^i}{dt} = \frac{M_0^i - M_z^i}{T_1^i} - R_{ij} \cdot M_z^i + R_{ji} \cdot M_z^j + \omega_1 \cdot M_y^i \qquad \text{(Equation 5.3)}$$

$$\frac{dM_x^i}{dt} = \frac{-M_x^i}{T_2^i} + 2\pi \cdot \Delta \cdot M_y^i \qquad \text{(Equation 5.4)}$$

$$\frac{dM_y^i}{dt} = \frac{-M_y^i}{T_2^i} - 2\pi \cdot \Delta \cdot M_x^i + \omega_1 \cdot M_z^i \qquad \text{(Equation 5.5)}$$

Where M^i is the proton magnetization of the bulk water (w) or macromolecule (m) pools, respectively, that is exchange with the other pool (j), T_1^i is the T_1 in pool i, T_2^i is the T_2 in pool i, R_{ij} is the exchange rate constant, and Δ is the chemical shift offset for the particular pool.

However, this has been derived elsewhere so we will not review it detail here (23). After accounting for the effect of the MT pulse ($MT_{pulse,j}$), we get to equation 5.6.

$$M_j^{NS}(TR, TI) = M_0\left(1 - 2 * MT_{pulse,j} * e^{-\frac{TI}{T_{1,j}}} + e^{-\frac{TR}{T_{1,j}}}\right)$$

$$j = CSF, GM, WM, b \qquad \text{(Equation 5.6)}$$

Notice that MT_{pulse} is listed for CSF, GM, WM, and blood. However, previous work has shown that the MT pulse does not affect blood (23). The contributions to MR water signal from CSF and the parenchymal compartments (extravascular tissue signal + microvascular blood signal) are given by Equation 5.1. Under steady-state conditions, the effect of the non-selective (NS) inversion is described by Equation 5.2. Simulations were performed based on information from Derdeyn et al that microvascular CBV changes up to 150% can occur under the autoregulatory range (25). The inversion time (TI) for blood was calculated to be 1081 ms given a repetition time (TR) of 6000 ms using Equation 5.2. All simulations were written in MATLAB® R2008a (The Mathworks, Natick, MA).

Table 5.1. Simulation Parameters and Values.

Simulation Parameters		Value	Units	Source
Echo time		12.25	ms	Sequence parameter
T_1	Gray matter	1209	ms	(26)
	White matter	758	ms	(26)
	Blood	1627	ms	(26)
	Cerebrospinal Fluid	4300	ms	(26)
T_2	Gray matter	70.8	ms	(19)
	White matter	81	ms	(26)
	Arterial Blood	123	ms	(19)
	Venular Blood	34	ms	(19)
	Cerebrospinal Fluid	1442	ms	(19)
C	Gray matter	0.89	mL H_20/mL compartment	(27)
	White matter	0.73	mL H_20/mL compartment	(28)
	Blood	0.87	mL H_20/mL compartment	(28)
	Cerebrospinal Fluid	1	mL H_20/mL compartment	(28)
CBV	Gray matter	0.053	mL/100 g parenchyma	(19)
	White matter	0.02	mL/100 g parenchyma	(19)
MT pulse	Duration	240	ms	Sequence Parameter
	Strength (B_1)	2	µT	Sequence Parameter
	Offset	-40	ppm	Sequence Parameter

5.3.2. Derivation of VASO Model to Estimate Ipsilateral CBV in Acute Stroke

We begin with the VASO model equations (Equations 5.2 and 5.3).

$$S_i \sim (C_i - CBV_i \cdot C_b) \cdot M_i^{NS}(TR,TI) \cdot e^{-\frac{TE}{T_{2,i}}} + CBV_i \cdot C_b \cdot M_b^{NS}(TR,TI) \cdot e^{-\frac{TE}{T_{2,b}}},$$

$$i = GM, WM$$

$$M_j = M_0\left(1 - 2 \cdot MT_{pulse,j} \cdot e^{-TI/T_{1,j}} + e^{-TR/T_{1,j}}\right), j = GM, WM, CSF, blood$$

In a VASO experiment, data is acquired when blood is nulled so we can set this equation to 0.

$$\boldsymbol{CBV_i \cdot C_b \cdot M_b^{NS}(TR,TI) \cdot e^{-TE/T_{2,b}} = 0} \qquad \text{(Equation 5.7)}$$

$$S_{WM} \sim (C_{WM} - CBV_{WM} \cdot C_b) \cdot M_0 \cdot \left(1 - 2 \cdot e^{-\frac{TI}{T_{1,WM}}} + e^{-\frac{TR}{T_{1,WM}}}\right) \cdot e^{-\frac{TE}{T_{2,WM}}} + \mathbf{0}$$

(Eq. 5.8)

This equation is problematic because we do not have a way of quantifying M_0 from our data. If we assume that the signal on the ipsilateral side of the brain will be different from the signal on the contralateral side of the brain due to hypothesized increased microvascular cerebral blood volume, then we can further write down these next two equations.

$$S_{WM,ipsi} = \left(C_{WM,ipsi} - CBV_{WM,ipsi} \cdot C_b\right) \cdot M_0 \cdot$$

$$(1 - 2 \cdot e^{-\frac{TI}{T_{1,WM,ipsi}}} + e^{-\frac{TR}{T_{1,WM,ipsi}}}) \cdot e^{-\frac{TE}{T_{2,WM,ipsi}}} \qquad \text{(Eq. 5.9)}$$

$$S_{WM,contra} = \left(C_{WM,contra} - CBV_{WM,contra} \cdot C_b\right) \cdot M_0 \cdot$$

$$(1 - 2 \cdot e^{-\frac{TI}{T_{1,WM,contra}}} + e^{-\frac{TR}{T_{1,WM,contra}}}) \cdot e^{-\frac{TE}{T_{2,WM,contra}}} \qquad \text{(Eq. 5.10)}$$

If we assume that the T_1 and T_2 of the white matter on both sides of the brain is the same (i.e. tissue relaxation has not begun to change in the ipsilateral side so $T_{1,WM,contra} = T_{1,WM,ipsi}$ and $T_{2,WM,contra} = T_{2,WM,ipsi}$, then $M_0(1 - 2e^{-TI/T_{1,WM}} + e^{-TR/T_{1,WM}}) \cdot e^{-TE/T_{2,WM}}$ will cancel out on the numerator and the denominator. If we assume a normal value for WM CBV (2 mL/100 g parenchyma) on the contralateral side, then we can solve for CBV on the ipsilateral side (29).

$$\frac{S_{WM,contra}}{S_{WM,ipsi}} = \frac{(C_{WM,contra} - CBV_{WM,contra} \cdot C_b)}{(C_{WM,ipsi} - CBV_{WM,ipsi} \cdot C_b)} \qquad \text{(Eq. 5.11)}$$

$$\left(C_{WM,ipsi} - CBV_{WM,ipsi} \cdot C_b\right) = \frac{S_{WM,ipsi}}{S_{WM,contra}}\left(C_{WM,contra} - CBV_{WM,contra} \cdot C_b\right)$$

(Eq. 5.12)

$$CBV_{WM,ipsi} \cdot C_b = C_{WM,ipsi} - \frac{S_{WM,ipsi}}{S_{WM,contra}}\left(C_{WM,contra} - CBV_{WM,contra} \cdot C_b\right)$$

(Eq. 5.13)

$$CBV_{WM,ipsi} = \frac{C_{WM,ipsi} - \frac{S_{WM,ipsi}}{S_{WM,contra}}\left(C_{WM,contra} - CBV_{WM,contra} \cdot C_b\right)}{C_b} \qquad \text{(Eq. 5.14)}$$

5.3.3. Imaging Parameters

Eighteen acute ischemic stroke patients were consented under an Institutional Review Board (IRB) and scanned on a 3T MRI scanner (Achieva, Philips Medical Systems, Best, The Netherlands) at the Washington Hospital Center (Washington DC, USA) with body coil transmit and 8-channel head coil with sensitivity encoding (SENSE). Diffusion tensor images (DTI), fluid attenuated inversion recovery (FLAIR), and dynamic susceptibility contrast-based (DSC) perfusion weighted images (PWI) were also acquired. Individual scan parameters can be found in Table 5.2.

Table 5.2. Sequence parameters for sequences acquired on acute ischemic stroke patients.

Scan	**Duration (mins)**	**Resolution (mm^3)**	**TR (ms)**	**TE (ms)**	**Other parameters**
Diffusion Tensor Imaging (DTI)	2:15	2x2x3.5	4418	62	max b-value = 1000, 16 directions
Gradient Echo (GRE)	2:13	0.7x0.7x3.5	800	12	
Fluid Attenuated Inversion Recovery (FLAIR)	1:48	1x1x3.5	9000	120	TI = 2600 ms
Magnetic Resonance Angiography (MRA)	2:09	0.7x0.7x0.7	23	3.5	FH = 60 mm
Transverse Relaxation Time (T_2)	1:12	1x1x7	3000	90	
Magnetization Transfer Enhanced VASO (MT-VASO)	2:45	2x2x3.5	6000	14	TI = 1081 ms, MT pulse offset = -40 ppm, MT pulse B_1 = 2 μT, MT pulse duration = 240 ms
DSC Perfusion Weighted Imaging (PWI)	1:24	3x3x7	1000	25	80 acquisitions, 20 mL of Magnevist (Bayer HealthCare)
T1 Post-contrast	1:25	0.7x0.7x7	450	8	

The MT-VASO scan was acquired using a field-of-view of 240x240x140 mm^3 with an imaging matrix of 80x80x40. The data was reconstructed to 256x256 to allow for co-registration with other imaging modalities. A 240 ms MT pulse (B_1 = 2 μT, offset frequency = -40 ppm) was applied before the 180^0 inversion pulse to attenuate the tissue magnetization at inversion and increase tissue SNR after TI. Other parameters include TI/TR/TE = 1081/6000/14 ms, which resulted in a total scan time of two minutes and forty-five seconds. The MT-VASO scan is described in detail elsewhere (23).

A follow-up FLAIR scan was acquired between 20 and 26 hours after the acute scan to verify tissue that progressed to infarction and to determine the size of the final infarct. The scan parameters of the follow-up FLAIR were identical to that of the acute FLAIR scan.

5.4. Data Processing

All data was processed using in-house written MATLAB® R2008a (The Mathworks, Natick, MA) routines. The different MRI modalities, DTI, FLAIR, DSC PWI, and MT-VASO, were coregistered using CATNAP (Coregistration, Adjustment, and Tensor-Solving – a Nicely Automated Program, https://masi.vuse.vanderbilt.edu/index.php/, developed at Johns Hopkins University, Baltimore, Maryland, USA, maintained by Vanderbilt University) (30). After co-registration, mean diffusion weighted (MDW), apparent diffusion coefficient (ADC), and fractional anisotropy (FA) parametric maps were generated automatically by CATNAP.

5.4.1. MT-VASO data processing

To allow for comparison between imaging modalities, we interpolated all scans to the same resolution (0.94 x 0.94 x 3.5 mm^3). Since small reductions in VASO signal intensity may be difficult to see with the naked eye, we automated the data analysis as follows. First, an in-house written region-growing algorithm was generated to create a white matter (WM) mask. Then, a region in contralateral normal appearing white matter (CNAWM) was selected. A t-statistic map of the ipsilateral side was calculated to assess difference with respect to CNAWM. The t-statistic was calculated on a voxel-by-voxel basis using the following equation:

$$t_{voxel} = \frac{x_{voxel} - \mu_{CNAWM}}{\sigma_{CNAWM}/n} \qquad \text{(Equation 5.15)}$$

Where x_{voxel} is defined as each voxel's VASO signal intensity, μ_{CNAWM} is defined as the mean VASO signal intensity over the CNAWM region, σ_{CNAWM} is defined as standard deviation of the VASO signal intensity over the CNAWM region, and n is defined as the number of voxels in the CNAWM region. In essence, what this equation mean is, every voxel was compared to the mean and standard deviation of the CNAWM. If the signal intensity of a particular voxel is comparable to CNAWM region, then its t-statistic will be close to zero. However, if a voxel contains increased microvascular CBV, then its signal intensity will be lower than that of the mean of the CNAWM region, which will lead to an increased t-statistic.

One issue with this method is deep gray matter. Because MT-VASO is an inversion recovery sequence, it is highly sensitive to differences in T_1. Since deep gray matter has a longer T_1 than white matter and less MT effect, it results in lower signal intensity than white matter for the MT-VASO sequence. This can lead to the misunderstanding that deep gray matter has higher CBV changes. To fix this problem, we compared the contralateral deep gray matter region with the ipsilateral gray matter region. This led to a more reasonable t-statistic value in the deep gray matter. Thus, we can use equation 4.6 to identify tissue with increased CBV that may be salvageable. Finally, one standard deviation above the mean of the CNAWM of the t-statistic map was used to threshold the entire t-statistic map, and this was overlaid on the original MT-VASO image. Figure 4.2 outlines this process in a flow chart. To interpret these images, one should look for asymmetries between the ipsilateral and contralateral side.

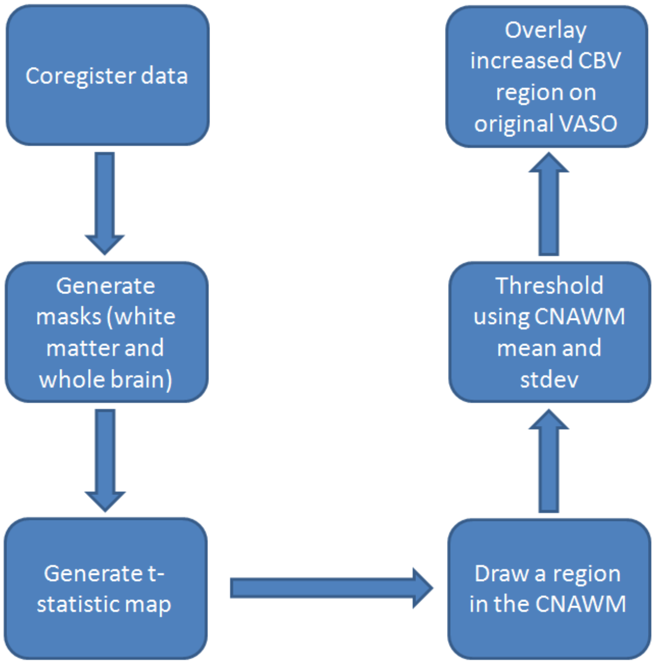

Figure 5.2. Flow-chart of data processing of MT-VASO Scan.

5.4.2. Determination of DWI/PWI/FLAIR lesions

Hyperintensities on the mean diffusion weighted images, time to peak weighted images, and 24-hour follow-up FLAIR images were manually delineated and chosen to represent the diffusion cores, perfusion penumbra, and final infarct in MIPAV (Medical Image Processing, Analysis, and Visualization, NIH).

5.4.3. Analysis of Infarct Percentage

Further data analysis was performed by analyzing the percentage of voxels that progressed to infarction. To determine this, the region of final infarct (determined by the hyperintensity in the FLAIR image) was subtracted from the region of hyperintensity on the mean diffusion weighted image to get the region of voxels that progressed to infarction. In this region, the number of voxels defined by the time to peak (DSC PWI) and MT-VASO scans were divided by the total number of voxels in this region to analyze the predictive power of the two techniques.

5.5. Results and Discussion

5.5.1. Patients

In total, six females (Age: 66±15 years old) and twelve males (Age: 60±12 years old) were scanned. Demographics for these patients include twelve African-Americans and five Caucasians.

Fifteen patients were scanned within fifteen hours of the ischemic event and before thrombolytic treatment (either with tPA or surgery). The other three patients were scanned 15 hours, 17 hours, and 21 hours after the ischemic event. One patient had severe leukoaraiosis (LA), which interfered with our ability to properly process the data because LA changes the T_1 relaxation time so this patient was excluded from the analysis. Background information on each patient can be found in Table 5.3.

Table 5.3. Background information about each patient.

Patient	Age	Gender	Time of MRI Scan with respect to 'Last Seen Normal'	NIH Stroke Scale (Admit/ Discharge)	Stroke Location	Vascular Territory	Treatment
1	50	F	1 hour 37 minutes	26/10	frontal lobe, parietal lobe	left MCA	IV tPA
2	62	M	2 hours 11 minutes	15/14	frontal lobe, parietal lobe, centrum semiovale	right MCA	Stenting, mechanical thrombectomy
3	57	F	19 hours 7 minutes	18/13	frontal lobe, parietal lobe	right MCA	
4	61	M	4 hours 31 minutes	20/19	frontal lobe, parietal lobe, temporal lobe, occipital lobe, caudate, putamen, internal capsule, globus pallidus, centrum semiovale, thalamus	right MCA, right PCA	IV tPA
5	66	M	3 hours 56 minutes	16/13†	frontal lobe	left MCA	IV tPA
6	50	M	9 hours 15 minutes	27/11	midbrain, pons, cerebellum	basilar	Stenting, angioplasty, ReoPro
7	76	M	7 hours 10 minutes	10/1	pariental lobe	right MCA	IV tPA
8	53	M	2 hours 23 minutes	21/42	frontal lobe, parietal lobe, temporal lobe	right ACA, right MCA	IV tPA
9*	76	F	6 hours 12 minutes	22/4	frontal lobe	left MCA	IV tPA

10	64	M	4 hours 41 minutes	10/8	frontal lobe, temporal lobe	right MCA	
11	62	F	0 hours 57 minutes	12/42	frontal lobe, parietal lobe, caudate, putamen, centrum semiovale, cerebellum	right MCA	Stent
12	63	M	5 hours 30 minutes	22/9†	frontal lobe, parietal lobe, temporal lobe, caudate, putamen, internal capsule, globus pallidus, centrum semiovale, thalamus	right MCA	IV tPA
13	85	F	2 hours 2 minutes	21/28†	frontal lobe, temporal lobe	left MCA	
14	49	M	1 hour 33 minutes	15/0	frontal lobe	left MCA	IV tPA
15	53	M	4 hours 4 minutes	7/3	internal capsule, thalamus	right lenticulostriate	IV tPA
16	84	M	3 hours 35 minutes	21/5	frontal lobe, parietal lobe	right MCA	IV tPA
17	78	F	6 hours 31 minutes	17/2	frontal lobe, parietal lobe, temporal lobe, caudate	left MCA	IV tPA
18	44	M	0 hour 48 minutes	7/7	frontal lobe, parietal lobe, temporal lobe	left MCA	IV tPA

* This dataset was discarded because this patient had leukoaraiosis, which changed tissue T_1 and interfered with the MT-VASO analysis.

† These datasets did not have discharge NIHSS information so 30-day NIHSS information was used.

5.5.2. Simulations

Figure 5.3 shows the results for expected changes in the VASO signal based on 30% incremented increases of white matter microvascular blood volume. In Donahue et al, assumptions were made on the size of the different compartments (white matter, gray matter, and CSF) (19). However, in our particular application of this technique, because of the partial voluming issue with gray matter and CSF and given the limits of our resolution, we limit our analysis to white matter. Thus, our simulations assumed that voxels contain 100% white matter. The simulations showed that for white matter, microvascular CBV increases of 30%, 60%, 90%, 120%, and 150%, respectively, will manifest in reductions of the VASO signal intensity from baseline CBV conditions by 1%, 2%, 3%, 4%, and 5%, respectively.

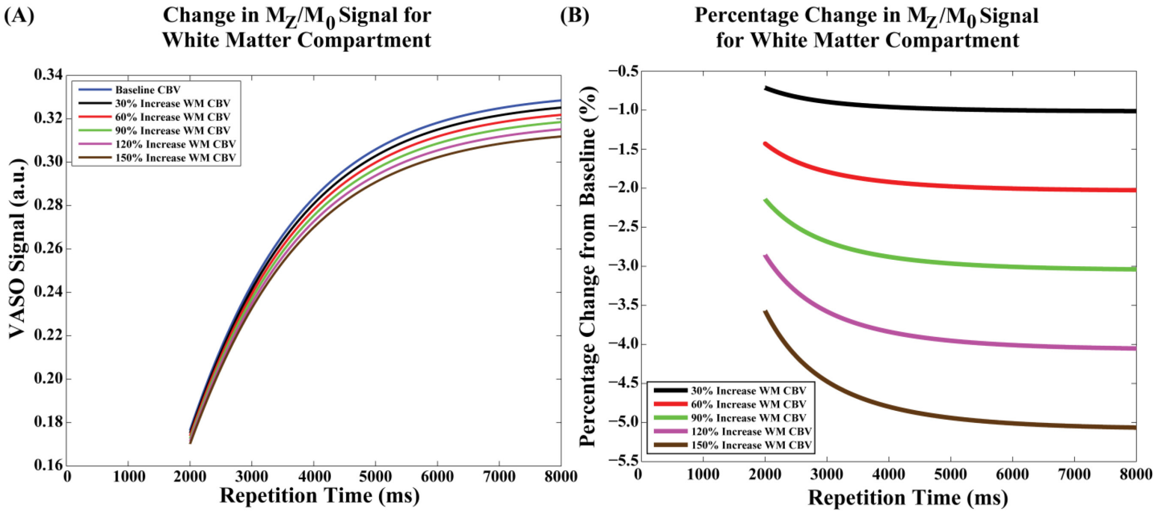

Figure 5.3. Simulated decrease in MT-VASO signal intensity due to different increases in microvascular cerebral blood volume (CBV).

Because of the time-sensitive nature of acute ischemia patients, I was only able to scan for 2 minutes and 45 seconds, which gave me a resolution of 2x2x3.5 mm^3. However, at this resolution, partial voluming effects (PVE) do not allow adequate resolution of gray matter so we restrict our analysis to white matter for patients.

5.5.3. Patient 1

Figure 5.4 shows data from a patient who was scanned one hour and thirty-seven minutes after last seen normal. The acute FLAIR scan shows no visible signs of infarct. The diffusion weighted scan shows a hyperintensity in the left hemisphere (radiological convention used in display) that spans across multiple slices indicating an area that may eventually progress to infarction. Time-to-peak weighted images show a region below the diffusion lesion that may progress to infarction if left untreated. The processed VASO images highlight a region similar to the hyperintensity on the time to peak weighted map. The follow-up FLAIR scan acquired 24 hours after the acute scans show evidence of infarction where the diffusion lesion was as well as where there were some perfusion abnormalities.

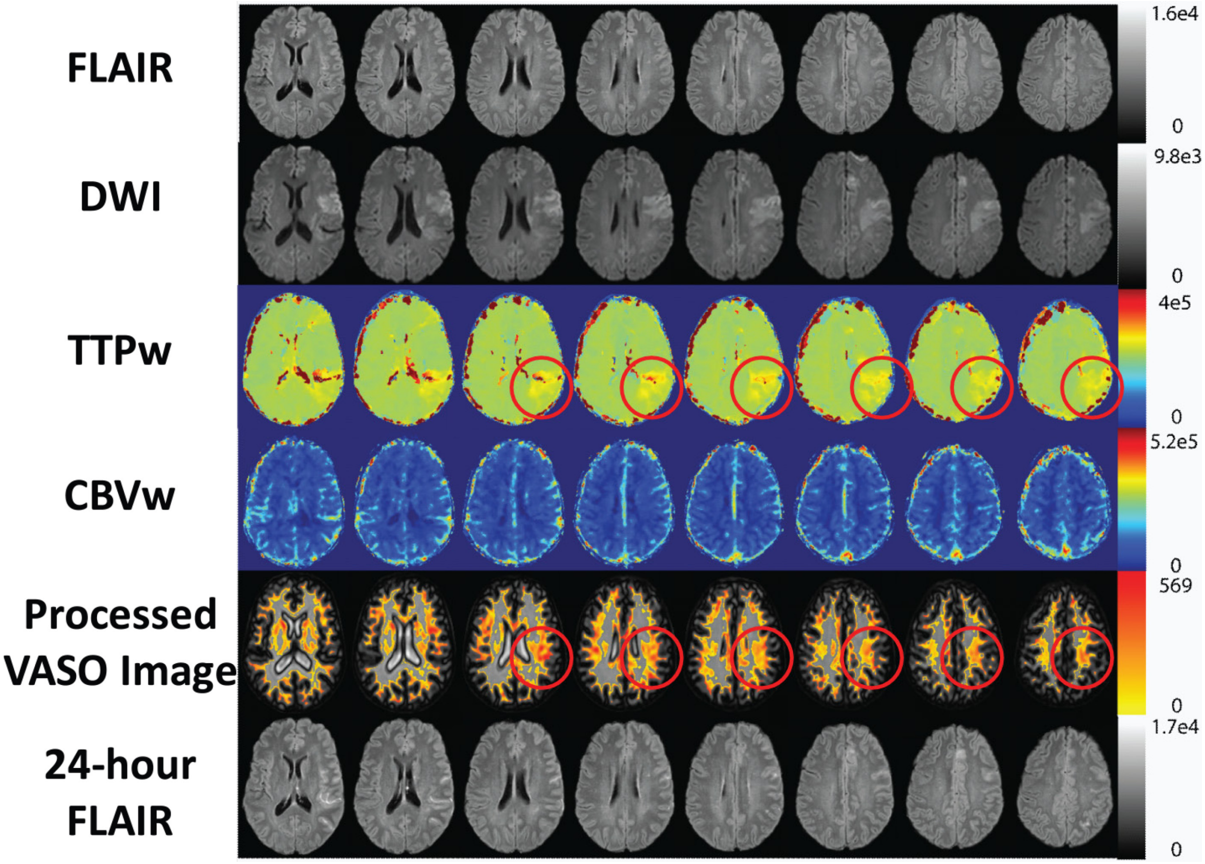

Figure 5.4. Images from patient 1, scanned 1 hour 36 minutes after last seen normal.

In this particular case, the processed VASO image is highly useful in showing asymmetries in multiple slices that could be due to increases in microvascular CBV caused by the occlusion in this patient. Additionally, it is interesting to notice asymmetries in the processed VASO map in the region where there are hyperintensities on the TTP-weighted images. Furthermore, the region of elevated time to peak and increased microvascular CBV do not appear to have progressed to infarction based on the follow-up FLAIR acquired one day later. Because this patient was treated with IV-tPA, one hypothesis would be that blood flow was restored to the regions of elevated microvascular CBV before blood vessels in that region collapsed allowing cerebral perfusion to be restored before cytotoxic edema occurred. Also, the hypothesis is that the regions are still viable when CBV is increased, which would be confirmed by this result.

5.5.4. Patient 2

Figure 5.5 shows data from a patient who was scanned two hours and eleven minutes after they were last seen normal. The acute FLAIR scan shows no evidence of changes in T_2 yet. However, a hyperintensity can be seen in the acute DWI. The DSC time-to-peak weighted image shows large regions of perfusion abnormalities. The DSC CBV weighted image shows elevated microvascular CBV in the ipsilateral region of the patient. The processed VASO image shows abnormalities in the same location of increased CBV. The follow-up FLAIR scan shows a lesion where the asymmetry in the processed VASO image was.

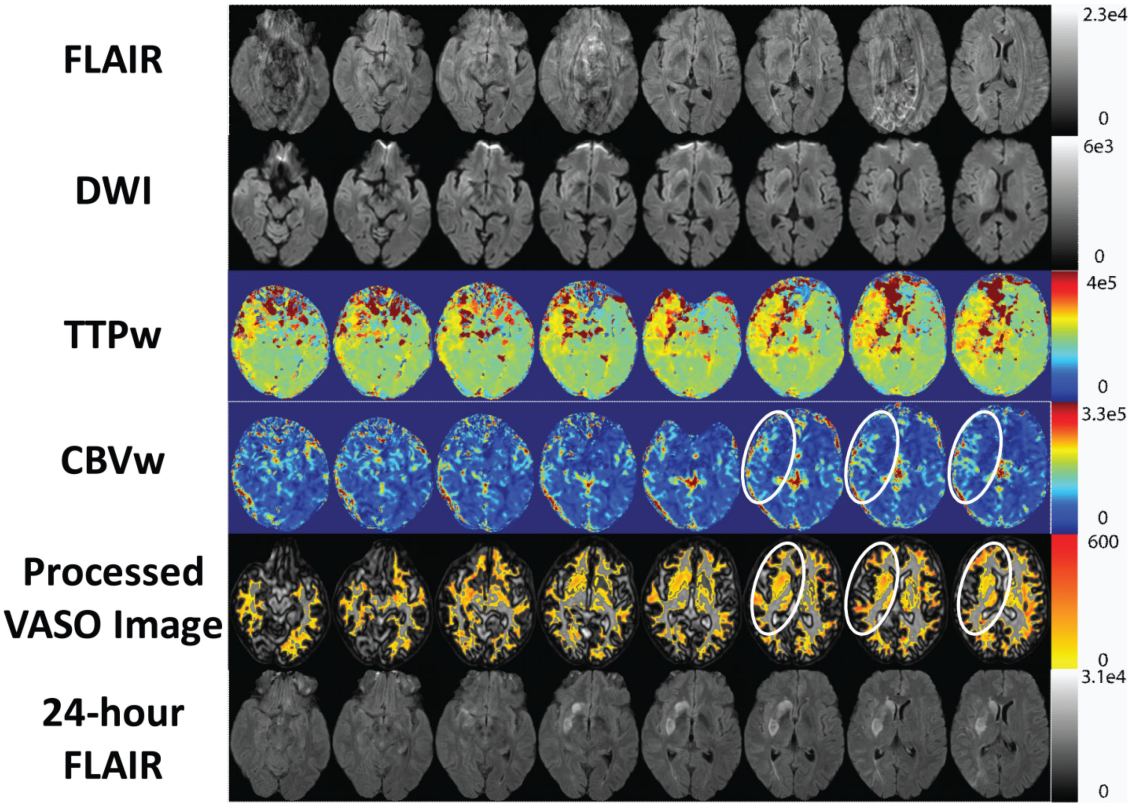

Figure 5.5. Images from patient 2, who was scanned 2 hours and 11 minutes after last seen normal.

In this second patient, the VASO image correlates well with the gadolinium-based dynamic susceptibility contrast weighted cerebral blood volume and time to peak parametric maps. Asymmetries in the VASO image are noted in regions with increased TTP and hyperintensities in the CBV parametric maps.

5.5.5. Patient 3

Figure 5.6 shows data from a patient who was scanned nineteen hours and seven minutes after she was last seen normal. In this patient, the acute FLAIR scan shows a hyperintensity, which is indicative of T_2 relaxation time increases. The acute mean diffusion weighted scan shows larger region of hyperintensity than the acute

FLAIR scan, which may imply that the ischemic region is larger than the infarct and more infarction may occur. The acute time to peak weighted scan shows two distinct regions: a core region that is in the same location as the diffusion lesion, as well as a penumbral region larger than the region of restricted diffusion. The DSC CBV image shows a region of reduced CBV where the blood vessels may have already collapsed and is not being perfused anymore. Our processed VASO map shows a distinct asymmetry. The 24-hour follow-up FLAIR scan shows a region of infarction as large as the region of perfusion deficit.

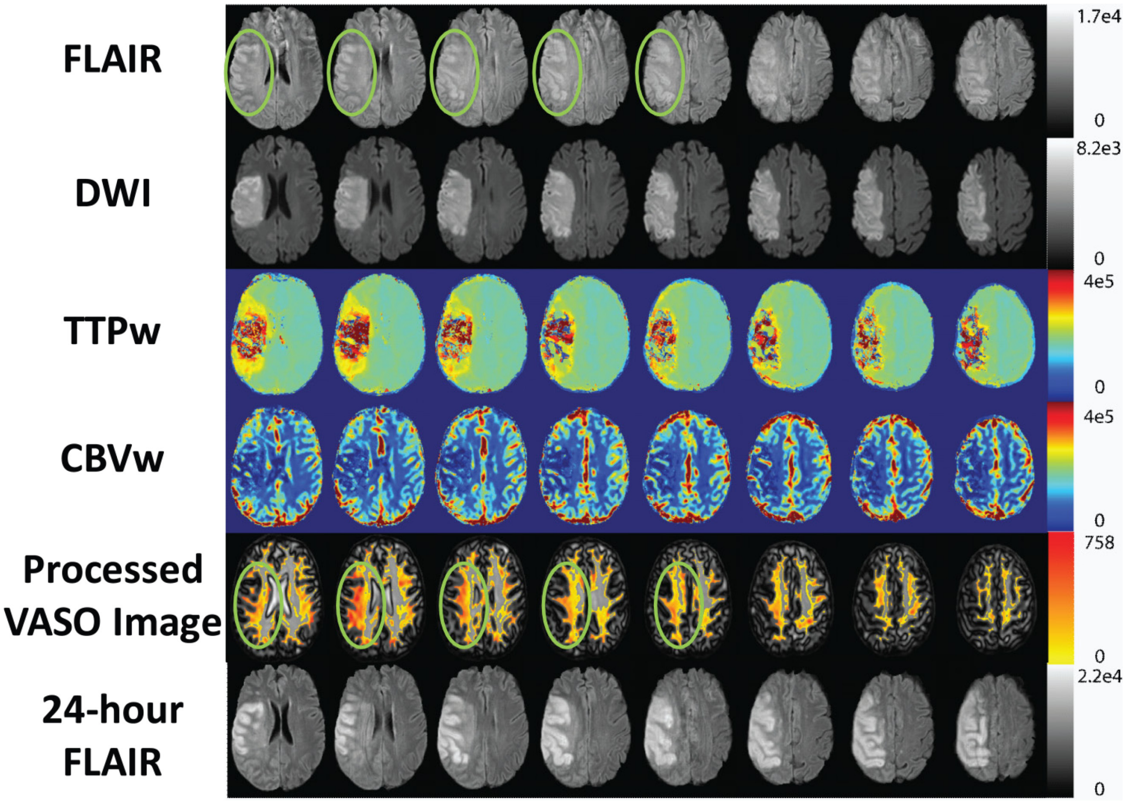

Figure 5.6. Images from patient 3, scanned 19 hours and 7 minutes after last seen normal.

The data from this particular patient shows that our technique may only be useful during the hyperacute phase of ischemia. After changes in the relaxation times

(T_1 and T_2) have begun to occur, it is difficult to distinguish these changes from CBV changes. Additionally, changes of T_1 and T_2 lead to the collapse of assumptions surrounding the model derived in section 5.3.2.

5.5.6. Group Analysis

Figure 5.6 shows the percentage of voxels that progressed to infarction. Patients 5 and 14 show no voxels that progressed to infarction based on the penumbra determined by the PWI.

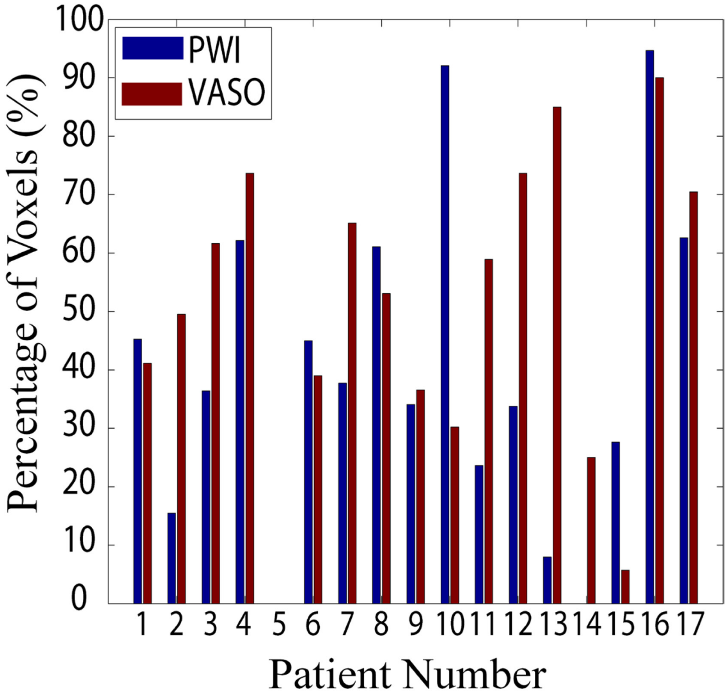

Figure 5.7. Percentage of Penumbral Voxels in White Matter that Progress to Infarction.

Except for patient 15, the results show that the area at risk of infarction judged from the VASO analysis is more predictive than that from the PWI/DWI mismatch. However, the VASO method is more tedious than the PWI approach.

There are a number of limitations with this study. First, we only investigated 18 patients. To determine if this technique is useful clinically, a study on a much larger scale would need to be conducted. Second, a limitation of this technique is its dependence on T_1. This causes problems if T_1 changes in stroke patients occur, which typically occurs if the blood clot is not treated in time. Additionally, because many stroke patients are older, other pathologies such as leukoaraiosis that causes T_1 changes may mask our ability to use this technique to analyze relative cerebral blood volume.

5.6. Conclusion

We developed a new method to image possible increases in microvascular cerebral blood volume and T_1 in white matter. MT-VASO can add information about regions of increased CBV, which may imply regions at-risk-of infarction in the perfusion penumbra. Drawbacks of this technique include (1) sensitivity to T_1 changes, which when past a certain time window could lead to a false interpretation of the data, and (2) limited analysis to white matter and deep gray matter because of insufficient signal-to-noise and resolution (in a clinically acceptable time frame) in the gray matter.

5.7. References

1. Mathers CD, Loncar D. Projections of global mortality and burden of disease from 2002 to 2030. PLoS Med. 2006;3(11):e442.

2. Rymer MM, Thrutchley DE. Organizing regional networks to increase acute stroke intervention. Neurol Res. 2005;27 Suppl 1:S9-16.

3. Furlan A, Higashida R, Wechsler L, Gent M, Rowley H, Kase C, Pessin M, Ahuja A, Callahan F, Clark WM, Silver F, Rivera F. Intra-arterial prourokinase for acute ischemic stroke. The PROACT II study: a randomized controlled trial. Prolyse in Acute Cerebral Thromboembolism. JAMA. 1999;282(21):2003-11.

4. Knight RA, Barker PB, Fagan SC, Li Y, Jacobs MA, Welch KM. Prediction of impending hemorrhagic transformation in ischemic stroke using magnetic resonance imaging in rats. Stroke. 1998;29(1):144-51.

5. Brinker G, Pillekamp F, Hossmann KA. Brain hemorrhages after rt-PA treatment of embolic stroke in spontaneously hypertensive rats. Neuroreport. 1999;10(9):1943-6.

6. Busch E, Kruger K, Allegrini PR, Kerskens CM, Gyngell ML, Hoehn-Berlage M, Hossmann KA. Reperfusion after thrombolytic therapy of embolic stroke in the rat: magnetic resonance and biochemical imaging. J Cereb Blood Flow Metab. 1998;18(4):407-18.

7. Hacke W, Donnan G, Fieschi C, Kaste M, von Kummer R, Broderick JP, Brott T, Frankel M, Grotta JC, Haley EC, Jr., Kwiatkowski T, Levine SR, Lewandowski C, Lu M, Lyden P, Marler JR, Patel S, Tilley BC, Albers G, Bluhmki E, Wilhelm M,

Hamilton S. Association of outcome with early stroke treatment: pooled analysis of ATLANTIS, ECASS, and NINDS rt-PA stroke trials. Lancet. 2004;363(9411):768-74.

8. Blakeley JO, Llinas RH. Thrombolytic therapy for acute ischemic stroke. J Neurol Sci. 2007;261(1-2):55-62.

9. Ostergaard L, Weisskoff RM, Chesler DA, Gyldensted C, Rosen BR. High resolution measurement of cerebral blood flow using intravascular tracer bolus passages. Part I: Mathematical approach and statistical analysis. Magn Reson Med. 1996;36(5):715-25.

10. Ostergaard L, Sorensen AG, Kwong KK, Weisskoff RM, Gyldensted C, Rosen BR. High resolution measurement of cerebral blood flow using intravascular tracer bolus passages. Part II: Experimental comparison and preliminary results. Magn Reson Med. 1996;36(5):726-36.

11. Kucinski T, Naumann D, Knab R, Schoder V, Wegener S, Fiehler J, Majumder A, Rother J, Zeumer H. Tissue at risk is overestimated in perfusion-weighted imaging: MR imaging in acute stroke patients without vessel recanalization. AJNR Am J Neuroradiol. 2005;26(4):815-9.

12. Sorensen AG, Copen WA, Ostergaard L, Buonanno FS, Gonzalez RG, Rordorf G, Rosen BR, Schwamm LH, Weisskoff RM, Koroshetz WJ. Hyperacute stroke: simultaneous measurement of relative cerebral blood volume, relative cerebral blood flow, and mean tissue transit time. Radiology. 1999;210(2):519-27.

13. Hatazawa J, Shimosegawa E, Toyoshima H, Ardekani BA, Suzuki A, Okudera T, Miura Y. Cerebral blood volume in acute brain infarction: A combined study with dynamic susceptibility contrast MRI and 99mTc-HMPAO-SPECT. Stroke. 1999;30(4):800-6.

14. Iadecola C. Bright and dark sides of nitric oxide in ischemic brain injury. Trends Neurosci. 1997;20(3):132-9.

15. Gally JA, Montague PR, Reeke GN, Jr., Edelman GM. The NO hypothesis: possible effects of a short-lived, rapidly diffusible signal in the development and function of the nervous system. Proc Natl Acad Sci U S A. 1990;87(9):3547-51.

16. Moro MA, Cardenas A, Hurtado O, Leza JC, Lizasoain I. Role of nitric oxide after brain ischaemia. Cell Calcium. 2004;36(3-4):265-75.

17. Back T, Hoehn M, Mies G, Busch E, Schmitz B, Kohno K, Hossmann KA. Penumbral tissue alkalosis in focal cerebral ischemia: relationship to energy metabolism, blood flow, and steady potential. Ann Neurol. 2000;47(4):485-92.

18. Lu H, Golay X, Pekar JJ, Van Zijl PC. Functional magnetic resonance imaging based on changes in vascular space occupancy. Magn Reson Med. 2003;50(2):263-74.

19. Donahue MJ, Lu H, Jones CK, Edden RA, Pekar JJ, van Zijl PC. Theoretical and experimental investigation of the VASO contrast mechanism. Magn Reson Med. 2006;56(6):1261-73.

20. Uh J, Lewis-Amezcua K, Martin-Cook K, Cheng Y, Weiner M, Diaz-Arrastia R, Devous M, Sr., Shen D, Lu H. Cerebral blood volume in Alzheimer's disease and correlation with tissue structural integrity. Neurobiol Aging. 2010;31(12):2038-46.

21. Donahue MJ, van Laar PJ, van Zijl PC, Stevens RD, Hendrikse J. Vascular space occupancy (VASO) cerebral blood volume-weighted MRI identifies hemodynamic impairment in patients with carotid artery disease. J Magn Reson Imaging. 2009;29(3):718-24.

22. Uh J, Yezhuvath U, Cheng Y, Lu H. In vivo vascular hallmarks of diffuse leukoaraiosis. J Magn Reson Imaging. 2010;32(1):184-90.
23. Hua J, Donahue MJ, Zhao JM, Grgac K, Huang AJ, Zhou J, van Zijl PC. Magnetization transfer enhanced vascular-space-occupancy (MT-VASO) functional MRI. Magn Reson Med. 2009;61(4):944-51.
24. Agarwal R, Brunelli SM, Williams K, Mitchell MD, Feldman HI, Umscheid CA. Gadolinium-based contrast agents and nephrogenic systemic fibrosis: a systematic review and meta-analysis. Nephrol Dial Transplant. 2009;24(3):856-63.
25. Derdeyn CP, Videen TO, Yundt KD, Fritsch SM, Carpenter DA, Grubb RL, Powers WJ. Variability of cerebral blood volume and oxygen extraction: stages of cerebral haemodynamic impairment revisited. Brain. 2002;125(Pt 3):595-607.
26. Lu H, Nagae-Poetscher LM, Golay X, Lin D, Pomper M, van Zijl PC. Routine clinical brain MRI sequences for use at 3.0 Tesla. J Magn Reson Imaging. 2005;22(1):13-22.
27. Lu H, Golay X, van Zijl PC. Intervoxel heterogeneity of event-related functional magnetic resonance imaging responses as a function of T(1) weighting. Neuroimage. 2002;17(2):943-55.
28. Herscovitch P, Raichle ME. What is the correct value for the brain--blood partition coefficient for water? J Cereb Blood Flow Metab. 1985;5(1):65-9.
29. Leenders KL, Perani D, Lammertsma AA, Heather JD, Buckingham P, Healy MJ, Gibbs JM, Wise RJ, Hatazawa J, Herold S, et al. Cerebral blood flow, blood volume and oxygen utilization. Normal values and effect of age. Brain. 1990;113 (Pt 1):27-47.

30. Farrell JA, Landman BA, Jones CK, Smith SA, Prince JL, van Zijl PC, Mori S. Effects of signal-to-noise ratio on the accuracy and reproducibility of diffusion tensor imaging-derived fractional anisotropy, mean diffusivity, and principal eigenvector measurements at 1.5 T. J Magn Reson Imaging. 2007;26(3):756-67.

Chapter 6: Application of Steady State Pulsed CEST to Image Acute Ischemic Stroke Patients

6.1. Abstract

It is widely known that thrombolytic therapy (intravenous tissue plasminogen activator), if given quickly after the occurrence of ischemia, can significantly improve clinical outcome. Currently, to evaluate whether a patient is a candidate for receiving thrombolytic therapy, the diffusion-perfusion mismatch based on magnetic resonance imaging can be used. However, the region of reduced perfusion that is at risk of infarction is frequently overestimated with current gadolinium-based perfusion weighted imaging, due to part of the area being due to benign oligemia. This can result in patients being taken for aggressive therapy when it may not actually be needed. Tissue pH reductions are expected to be a better marker for at risk tissue in acute ischemia patients that is still salvageable because they reflect impaired aerobic metabolism. In this chapter, we explore using a modified steady-state pulsed chemical exchange saturation transfer imaging sequence to analyze pH changes in acute ischemic stroke patients.

6.2. Introduction

Stroke, the third leading cause of death and leading cause of disability, affects approximately fifteen million people each year in the world (1). Acute ischemic stroke, caused by the occlusion of cerebral blood vessels by an arterial embolus or thrombus, accounts for approximately 85% of cases (2). A number of studies have shown that thrombolytic treatment with intravenous tissue plasminogen activator (tPA) to restore blood flow can be useful for reducing tissue infarction when given within the first 3-6 hours post-onset (3). However, the benefit of tPA must be weighed against the risk of intracranial hemorrhage (4-6), which occurs in approximately 6% (7) of cases in which patients are treated with tPA and frequently leads to irreversible damage. The ability to quickly and accurately assess whether patients have salvageable ischemic tissue is critical to improving functional outcome and minimizing long-term disability.

tPA has a number of contraindications for its usage (8). One of the most important contraindications before giving tPA is evidence of hemorrhage, which can be assessed by CT or MRI. Of these, CT is faster and more convenient, but MRI is much more versatile and can offer other contrasts. Diffusion-weighted imaging (DWI) and dynamic susceptibility contrast-based perfusion-weighted imaging (PWI) are MRI-based scans that are frequently used to evaluate whether a patient would be a good candidate for tPA. Specifically, DWI is able to portray regions where disruption of cellular membrane potential has occurred. This corresponds to tissue that is likely to progress to infarction. DSC PWI employs the use of an exogenous gadolinium-based tracer; following the tracer as a function of time allows for qualitative assessment of mean transit time (MTT), time to peak (TTP), cerebral blood flow (CBF), and cerebral blood volume (CBV) (9, 10). The parametric maps derived from the PWI scan can be used to determine regions of the brain that are functionally intact but at risk of infarction if the ischemia is not reversed. Patients with these regions are ideal candidates for thrombolytic treatment with tPA. Thus, the DWI/PWI mismatch, or "perfusion penumbra," can be used in principle to assess the extent of tissue that is ischemic but has not yet proceeded to infarction. However, the actual ischemic penumbra, i.e. region at risk of infarction, is not straightforward to identify from the DWI/PWI mismatch. There have been numerous reports that the penumbra defined by PWI frequently overestimates the true region at risk (11). This is because reductions in perfusion imaged with PWI actually cover two regions: (1) an oligemic region that contains benign reductions in blood flow that will eventually revert on its own to normal perfusion, and (2) a region that, if left untreated, will progress to infarction. Recent evidence has shown that intracellular pH is reduced in regions of the brain with cerebral blood flow low enough such that functional integrity is maintained, but cellular respiration changes from aerobic respiration (with oxygen) to anaerobic respiration, which leads to a build up of lactic acid and reduced pH.

Chemical exchange saturation transfer (CEST) MRI has recently been shown to be sensitive to changes in pH (12-15), especially the use of so-called amide proton transfer (APT) MRI, in which the combined signals of amide protons in brain tissue are detected via their exchange with the water signal detected by MRI. Preclinical ischemia models have confirmed that APT may predict areas that go to infarction better than PWI or DWI (15).

Our hypothesis is that patients with regions of reduced blood flow and reduced pH and no diffusion impairment have tissue that is at risk of infarction if not properly reperfused. Here we explore the feasibility of using a Steady State Pulsed Chemical Exchange Saturation Transfer (SSP-CEST) to visualize tissue at risk of infarction in acute cerebral ischemia patients in a clinically feasible time frame. CEST offers several benefits to current methods for looking at the ischemic penumbra: (1) CEST is a non-invasive technique. Numerous studies have linked occurrences of nephrogenic systemic fibrosis (NSF) to use of gadolinium-based contrast agents; (2) CEST will not highlight regions of benign oligemia because pH contrast is derived from cellular anaerobic respiration caused by reduced cerebral blood flow making it potentially more accurate than the currently used DSC-PWI.

6.3. Materials and Methods

CEST MRI generally involves the acquisition of a so-called saturation spectrum or Z-spectrum (16) in which the ratio of the saturated (S_{sat}) and unsaturated (S_0) water signals is plotted as a function of saturation frequency difference ($\Delta\omega$) with water. Because the exchangeable protons tend to resonate downfield (at higher frequency) from water and in an effort to remove the symmetric effects from direct water saturation (DS), CEST data are commonly analyzed using asymmetry analysis with respect to the water frequency set at $\Delta\omega=0$ and normalized to unsaturated signal (S_0). Defining the MT ratio (MTR) as $1 - S_{sat}/S_0$, this gives:

$$MTR_{asymmetry}(\Delta\omega) = MTR(\Delta\omega) + MTR(-\Delta\omega) = \frac{S_{sat}(-\Delta\omega) - S_{sat}(\Delta\omega)}{S_0}$$ (Equation 6.1)

Obviously such an analysis will not be completely correct if any MT effects occur upfield from water. This unfortunately is the case in vivo where MT effects of semi-solid tissue components (conventional MT contrast or MTC) cause a strong, broad (tens of ppm) and asymmetric component to the Z-spectrum (17, 18). To complicate matters, a recent study of glycosaminoglycans (19) indicated the presence of an additional upfield MT effect. This was attributed to nuclear Overhauser enhancements (NOE) in the NMR spectral range for aliphatic and olefinic protons, ranging from 0-5 ppm in the proton spectrum or -5 to 0 ppm in the Z-spectrum (20-22). This was later confirmed by others (23, 24). Assuming removal of the DS, the asymmetry thus needs to be described by:

$$MTR_{asymmetry}(\Delta\omega) = MTR^{CEST}_{asymmetry}(\Delta\omega) + MTR^{MTC}_{asymmetry}(\Delta\omega) + MTR^{NOE}_{asymmetry}(\Delta\omega)$$

(Equation 6.2)

Notice that the MTC effects in (semi)-solid tissue components originate from fast dipolar transfer of NOEs through spin diffusion followed by transfer to water and are hidden in a broad solid-state spectrum. The sharper NOE-based signals measured in the aliphatic and olefinic spectral range, on the other hand, are from mobile macromolecular components with finite linewidth (20, 21). The fact that signals originating from non-exchangeable protons appear in the Z-spectrum indicates the presence of a transfer mechanism to water, which has been attributed to either direct through-space dipolar transfer (19, 24) or a relay mechanism via exchangeable protons (22). Irrespective of this, the opportunity to detect NOE-relayed signals based in mobile macromolecules offers an opportunity to study such compounds non-invasively with high sensitivity in vivo.

One problem to address is how these NOEs can be detected without too much MTC interference. Fortunately, the relative contributions of MTC and CEST effects can be tuned (25, 26) by varying saturation pulse length (t_{sat}) and field strength (B_1). We recently showed that this approach can be optimized to detect slower transfer processes, such as due to exchanging amide protons and NOE-relayed effects, with minimal MTC interference (23). This can be accomplished by performing a low-power steady state pulsed CEST experiment and removing the DS contribution using a Lorentzian difference analysis (LD).

6.3.1. Simulations

Simulations were performed using the 3-pool model (a = bulk water pool, b = bound water pool, and c = amide proton pool) of the chemical exchange modified Bloch equations (Equations 6.1-6.9) (27). Analysis was performed of how much amide proton exchange rate and proton transfer ratio (PTR) drops when tissue acidosis occurs. Recent research from positron emission tomography (PET) and as well as other research techniques have shown that during ischemia, pH can drop to 6.4 to 6.6 if serum glucose is still in the normal range (28). However, with plasma hyperglycemia, tissue pH can drop down to 6.0 or 6.1 because of continued delivery of glucose and production of lactate during anaerobic glycolysis (28). Furthermore, when pH drops to 5.9, tissue infarction occurs (29). Both gray matter and white matter values were simulated. Table 6.1 summarizes a list of parameters that were used for this simulation.

$$\frac{dM_x^a}{dt} = -(\omega_a - \omega)M_y^a - k_{2a}M_x^a + C_bM_x^b + C_cM_x^c \tag{Equation 6.3}$$

$$\frac{dM_x^b}{dt} = -(\omega_b - \omega)M_y^b - k_{2b}M_x^b + C_{ab}M_x^a \tag{Equation 6.4}$$

$$\frac{dM_x^c}{dt} = -(\omega_c - \omega)M_y^c - k_{2c}M_x^c + C_{ac}M_x^a \tag{Equation 6.5}$$

$$\frac{dM_y^a}{dt} = (\omega_a - \omega)M_x^a - k_{2a}M_y^a + C_bM_y^b + C_cM_y^c - \omega_1M_z^a \tag{Equation 6.6}$$

$$\frac{dM_y^b}{dt} = (\omega_b - \omega)M_x^b - k_{2b}M_y^b + C_{ab}M_y^a - \omega_1M_z^b \tag{Equation 6.7}$$

$$\frac{dM_y^c}{dt} = (\omega_c - \omega)M_x^c - k_{2c}M_y^c + C_{ac}M_y^a - \omega_1M_z^c \tag{Equation 6.8}$$

$$\frac{dM_z^a}{dt} = \frac{M_0^a}{T_1^a} - k_{1a}M_z^a + C_bM_z^b + C_cM_z^c + \omega_1M_y^a \tag{Equation 6.9}$$

$$\frac{dM_z^b}{dt} = \frac{M_0^b}{T_1^b} - k_{1b}M_z^b + C_{ab}M_z^a + \omega_1M_y^b \tag{Equation 6.10}$$

$$\frac{dM_z^c}{dt} = \frac{M_0^c}{T_1^c} - k_{1c}M_z^c + C_{ac}M_z^a + \omega_1M_y^c \tag{Equation 6.11}$$

Where M_x^i, M_y^i, and M_z^i (i = a, b, c) represents the magnetization in the x, y, and z directions for pool i , T_{1i} and T_{2i} (i = a, b, c) is the longitudinal and transverse relaxation times in the absence of exchange for pool i, ω is the RF irradiation frequency, ω_i (i = a, b, c) is the Larmor frequency of pool i, ω_1 is the nutation rate of the RF irradiation, C_{ab} is the transition rate of pool A protons leaving pool A and entering pool B, and C_{ac} is the transition rate of pool A protons leaving pool A and entering pool C. Due to mass conservation, the following equalities also hold true:

$$C_{ab} = (\frac{M_0^b}{M_0^a})C_b \qquad \text{(Equation 6.12)}$$

$$C_{ac} = (\frac{M_0^c}{M_0^a})C_c \qquad \text{(Equation 6.13)}$$

$$C_a = C_{ab} + C_{ac} \qquad \text{(Equation 6.14)}$$

Where M_0^i is the equilibrium magnetization for pool i (i = a, b, c) that are proportional to the concentrations of the three pools, and equations for k_{1i} (i = a, b, c) and k_{2i} (i = a, b, c) are the following:

$$k_{1i} = \frac{1}{T_{1i}} + C_i \qquad \text{(Equation 6.15)}$$

$$k_{2i} = \frac{1}{T_{2i}} + C_i \qquad \text{(Equation 6.16)}$$

Table 6.1 shows parameters used in the simulations.

Table 6.1. Simulation Parameters

	Free Water Pool (GM)	Free Water Pool (WM)	Bound Water Pool (pool b)	Amide Proton Pool (pool c)
T_1 (ms)	1209(30)	758(30)	1200	590ǂ
T_2 (ms)	70.8(30)	81(30)	0.011(18)	33
Exchange Rate, C_{ab} and C_{ac} (1/s)	0	0	14	28(12)
Chemical Shift (ppm)	0	0	0	3.5(12)

ǂ This value could not be found in literature for the 3T field strength; thus, it was estimated using published values at 4.7T. At 4.7T, $R_{1,amide}$ = 1.3 s ($T_{1,amide}$ = 0.77 s) (31)

A simulation (figure 6.1) of the steady state pulsed CEST sequence over a variety of CEST saturation pulse parameters (using a sinc-gauss saturation pulse) shows that the pulse duration and pulse B_1 that maximize the CEST effect 17 ms and 1.2 μT, respectively.

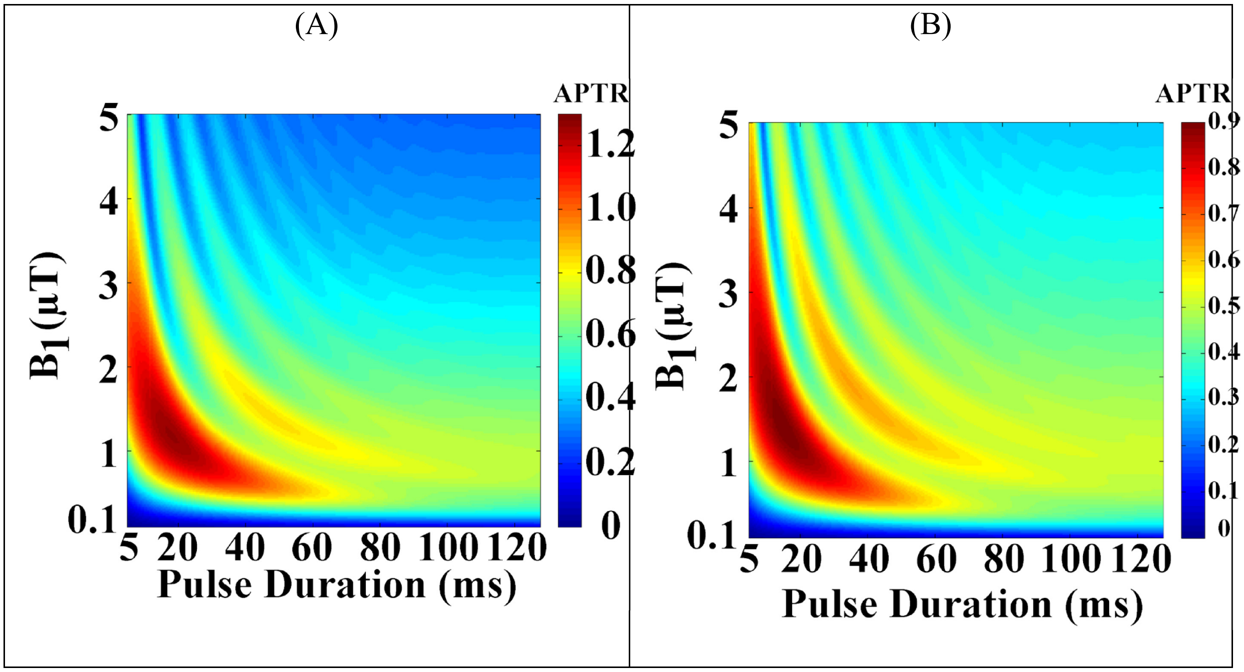

Figure 6.1. Analysis of Optimal CEST Saturation Pulse Parameters Based on 3-pool Bloch-McConnell Simulation for (A) Gray Matter and; (B) White Matter

However, when using this combination to simulate a z-spectra, it was found that a 17.5 ms pulse is not selective enough and leads to a significant amount of direct saturation, particularly around the irradiation offset frequency of interest ($\omega = +3.5$ ppm). This makes using the Lorentzian Difference Analysis (LDA) to process z-spectra quite difficult because the resulting z-spectrum is not in the form of a Lorentzian (23). Therefore, further investigation was performed to find a more selective saturation pulse and a saturation pulse B_1 that would yield a z-spectrum with a lineshape that could be fit with a Lorentzian and could maximize the CEST effect. Further analysis showed that a sinc-gauss saturation pulse duration of 25 ms and a saturation pulse B_1 of 1 µT fulfills this criteria.

Using this optimal saturation pulse duration (25 ms) and optimal saturation pulse B_1 (1 µT), it was explored how pH changes the exchange rate of amide protons and how this affects the APT effect. Using the base-catalyzed equation (Equation 6.15) determined by Zhou et al using phosphorus spectroscopy, we substituted several relevant pHs (6.0 to 7.4, increment 0.1) for ischemia and calculated the exchange rate for those respective pHs (12). These exchange rates were evaluated in the context of the 3-pool model to see how the APT effect changes for reductions in pH.

$$C_{ac} = 5.57 * 10^{pH-6.4} \qquad \text{(Equation 6.17)}$$

The resulting CEST z-spectra for those simulations are shown in figure 6.2.

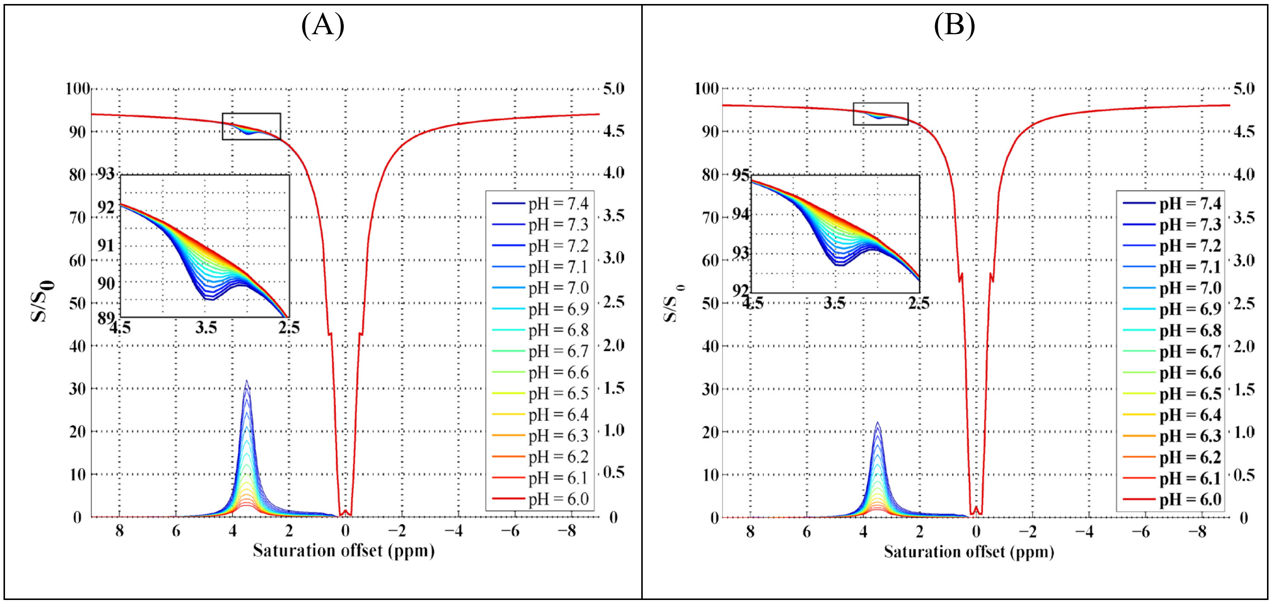

Figure 6.2. Simulation of 3-pool Bloch-McConnell Equation for Changes in pH (A) in a voxel with 100% Gray Matter and (B) in a voxel with 100% White Matter.

Futhermore when using MRI to acquire images of the brain, one of the issues that we frequently run into is partial volume effects. Because the signals that we are trying to detect are very small (based on simulations, on the order of 0.2-1.3%), it is important to acquire larger voxels to increase the signal-to-noise ratio (SNR). However, when larger voxels are acquired, one voxel has multiple compartments including gray matter, white matter, cerebrospinal fluid (CSF), and blood. When a voxel has multiple compartments, we have partial volume effects and need to account for this in our model. In order to simulate the APT signal in cases where partial volume effects leads to multiple compartments in each voxel, we simulated a voxel with 20% gray matter and 80% white matter. Results from this simulation are displayed in table 6.2.

Table 6.2. Table of APT values at Different pHs and the Difference from Normal.

pH	k_{sw} (1/s)	APT in 100% GM	Change from Normal pH	APT in 100% WM	Change from Normal pH	APT in 20% GM, 80% WM	Change from Normal pH
7.4	55.7	1.60	0%	1.11	0%	1.21	0%
7.3	44.2	1.50	-5.92%	1.05	-6.05%	1.14	-6.02%
7.2	35.1	1.38	-14.00%	0.96	-14.23%	1.04	-14.16%
7.1	27.9	1.22	-23.60%	0.85	-23.91%	0.92	-23.83%
7.0	22.1	1.06	-33.88%	0.73	-34.23%	0.80	-34.14%
6.9	17.6	0.90	-44.00%	0.62	-44.37%	0.68	-44.27%
6.8	14.0	0.75	-53.36%	0.52	-53.73%	0.56	-53.63%
6.7	11.1	0.61	-61.64%	0.42	-62.00%	0.46	-61.90%
6.6	8.8	0.50	-68.72%	0.35	-69.06%	0.38	-68.97%
6.5	7.0	0.41	-74.66%	0.28	-74.97%	0.30	-74.89%
6.4	5.6	0.33	-79.56%	0.23	-79.84%	0.25	-79.77%
6.3	4.4	0.26	-83.56%	0.18	-83.81%	0.20	-83.75%
6.2	3.5	0.21	-86.80%	0.14	-87.03%	0.16	-86.97%
6.1	2.8	0.17	-89.41%	0.12	-89.62%	0.13	-89.57%
6.0	2.1	0.14	-91.52%	0.09	-91.70%	0.10	-91.65%

6.3.2. Phantom Creation

A 10% BSA phantom was created by dissolving 42 g of BSA (66.5 kD; Sigma–Aldrich, St Louis, MO) in 420 mL of phosphate-buffered solution, giving a

1.5 mM solution. The resulting mixture was poured into eight 50-mL Falcon tubes and the pH was titrated (Seven Compact, Mettler Toledo) to 5.70, 6.01, 6.33, 6.61, 7.01, 7.29, 7.60, and 8.00. A ninth tube was filled with PBS as a control. A solution of 0.2% sodium azide (Sigma-Alderich, St. Louis, MO) was added to each of the nine tubes to preserve the phantoms. All tubes were capped and sealed with Parafilm (Lab Depot, Dawsonville, GA, USA). The phantoms were then placed in a larger container (The Container Store**,** Plano, TX, USA), and the large container containing the eight pH phantoms and PBS were placed in the 32 channel head coil on the 3T Philips system.

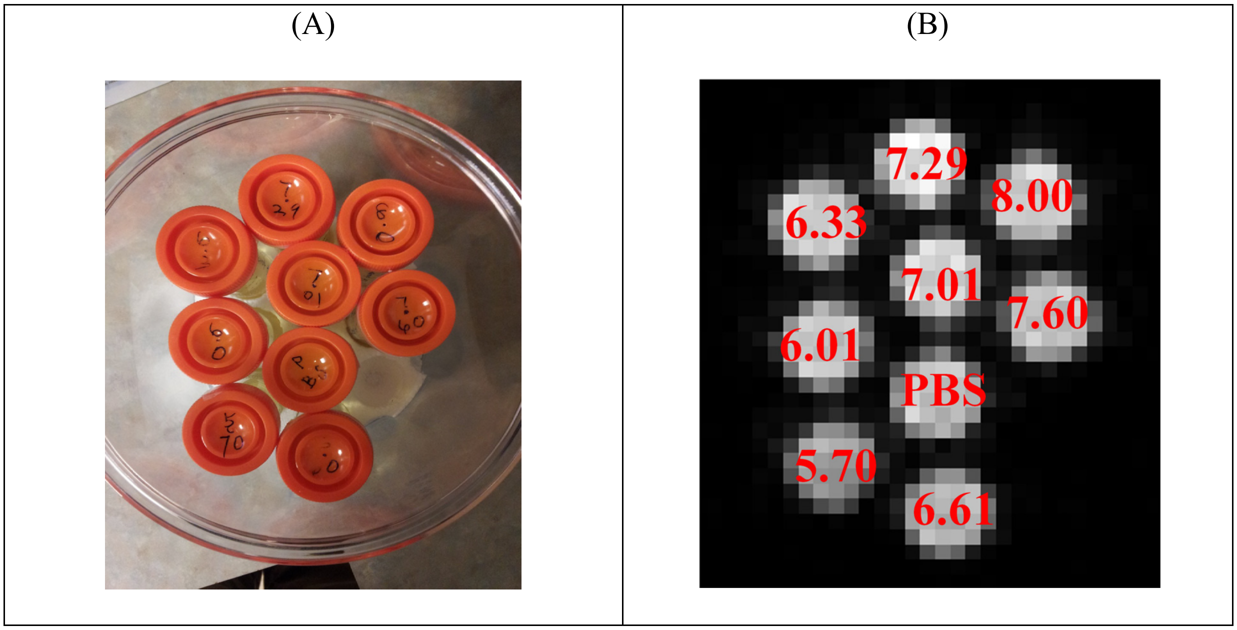

Figure 6.3. Images of pH phantoms (A) Arrangement of phantoms asymmetrically in large container, and (B) Corresponding MRI image of phantoms.

6.3.3. Phantom Scan

The phantoms were scanned on a 3T Philips Achieva scanner using a 32-channel receive only SENSitivity-Encoded (SENSE) head coil to detect the signal. For the phantom scan, a steady state pulsed CEST sequence was run with the following parameters: saturation pulse duration = 25 ms, saturation pulse B_1 = 1 μT. The spatial resolution was 4.4x4.4x4.4 mm^3. A random number generator was used to generate the order of frequencies that the scan was run. The randomly ordered saturation frequency offsets (in ppm, relative to the water frequency set to 0) were unsaturated (unsat), unsat, -5.6, -10, -0.5, 7, 14.4, unsat, 10.4, -0.4, -2.7, -11.4, -0.9, unsat, -11.6, -3.3, -6, 1.1, -7.4, unsat, -5.2, 6.4, -1.4, 11.2, -5.8, unsat, 12.4, 4.9, -1.9, 5.7, -3.1, unsat, -10.6, -1.3, -4.3, 12, -32, unsat, -3.9, -4.4, -28, -6.8, -9.6, unsat, -8.8, -0.3, 3.9, -4.6, 36, unsat, 0.7, -3, 4.5, 0.5, 3.7, unsat, -14.4, 14.2, 3.2, 5.6, 3.8, unsat, 4, -7.2, 3.5, 9, -0.8, unsat, 8, -3.2, 40, -2.9, -1.6, unsat, -15, -14.2, -18, -24, 5, unsat, -5, 11.4, 5.3, 6.6, -8.4, unsat, -4.5, -12.6, 0.3, 5.8, 3.3, unsat, 1.7, 4.2, -9.2, 5.9, 13.8, unsat, 11.6, -9.8, -2.2, -14.6, 2.6, unsat, -3.6, -13.6, -0.7, 10, 0.8, unsat, -2, 2.3, -12, -1.7, 9.8, unsat, -5.1, -3.4, -1.5, 5.1, -2.8, unsat, 6, 4.4, -4.8, 4.1, 1.5, unsat, 4.8, -5.9, 1.6, -7.6, 0.1, unsat, 8.2, -10.2, 3.4, -13.8, 15, unsat, 1.4, 7.6, 9.2, -2.3, -2.4, unsat, 12.8, 14.8, 6.2, 1.8, 1.9, unsat, -3.5, 8.8, -9, -11.2, 2.5, unsat, -6.4, 8.6, 0.2, -36, -13, unsat, -4, 2.9, -11.8, -10.4, -1, unsat, 32, 7.8, -4.1, -13.2, 3.1, unsat, 5.2, -8.6, 5.4, 18, -14, unsat, 20, -3.7, 3, 9.4, 0.9, unsat, 2.2, 0, -0.2, 12.6, -8.2, unsat, 9.6, 11.8, 0.6, -8, 14, unsat, 5.5, 13.2, 12.2, 7.4, -0.1, unsat, 14.6, 0.4, -7.8, -12.2, -12.4, unsat, -5.5, 1.3, 13, -11, 1, unsat, -1.8, -9.4, 2.1, 11, -4.9, unsat, 6.8, 28, 2.4, -16, -5.4, unsat, 2, -0.6, -6.6, -13.4, -20, unsat, 3.6, -3.8, 24, -5.3, -4.2, unsat, 2.8, 10.6, 13.6, -2.1, -2.6, unsat, 13.4, 16, 4.6, -4.7, 10.8, unsat, -7, -12.8, 4.3, 7.2, -14.8, unsat, 1.2, -10.8, 2.7, -1.2, -2.5, unsat, -1.1, -40, -5.7, 8.4, 4.7, unsat, 10.2, -6.2, unsat, unsat. Total acquisition time was 97 minutes 59 seconds. The unsaturated references were acquired using the same sequence as the saturated volume (including the TR) except with the RF saturation pulse turned off.

6.3.4. CEST Baseline Correction

It was observed that the intensive gradient switching in this sequence led to a baseline signal intensity drift that affected the measured CEST effects. To measure such scanner drift, a multishot gradient echo scan (7 lines of k-space acquired each shot) was run continuously for 65 minutes on a standard issue Philips “blue head” phantom, which was subsequently used to verify drift on two of our 3T Philips scanners (XMR and MR1). To quantify this drift, signal intensities were normalized to the first point and multiplied by 100 to convert it into a percentage.

In order to correct for this drift in the pH phantoms, we acquired S_0 volumes every five frequencies (see frequency list in section 5.3.3). To perform baseline correction, we fitted a smoothed spline to the S_0 points as a function of scan time elapsed on a voxel-wise basis. Then between each pair of S_0 points, the spline fit was linearly interpolated, and this information was used to correct the data acquired. This method was applied to the pH phantoms to verify that it removed biases caused by scanner drift.

6.3.5. Healthy Volunteers

Three healthy volunteers (Age: 45 ± 18) were consented and scanned on a Philips Achieva 3T MRI scanner using a 32-channel SENSE receive only head coil for signal reception. Demographics of healthy volunteers include two females and one male, one Asian and two Caucasians. Healthy volunteers received a FLuid Attenuated Inversion Recovery (FLAIR) scan, a Gradient Recalled Echo (GRE) scan, a steady-state pulsed CEST, a Magnetic Resonance Angiography (MRA) scan, and a Diffusion Tensor Imaging (DTI) scan.

6.3.6. Patients

Five acute stroke patients (Age: 55 ± 23) were consented and scanned on a Philips Achieva 3T MRI scanner using a 32-channel SENSE receive only head coil. One dataset had to be repeated due to excessive motion. Patients received the following scans: 1) Acute FLAIR, to confirm evidence infarction; 2) DTI, to see if there are regions that will progress to infarction; 3) SSP-CEST, to study pH changes; and 4) PWI, to study the perfusion diffusion mismatch. A follow-up FLAIR was acquired at least 24 hours after the initial scan. Two patients did not receive a follow-up FLAIR scans because they were discharged from the hospital before a follow-up could be acquired and could not be reached. Other relevant patient information can be found in Table 5.

Upon admission, patients were evaluated with the National Institutes of Health Stroke Scale (NIHSS), a tool used by physicians to quantify the degree of impairment of stroke patients. The NIHSS rates patients over eleven categories including level of consciousness, horizontal eye movement, visual field test, facial palsy, motor arm, motor leg, limb ataxia, sensory, language, dysarthria, extinction and inattention. Most categories are rated from zero to four (some are zero to two, some zero to three), where zero represents normal function and four represents severe impairment. Scores from each category are summed together to arrive at the comprehensive NIHSS score. The maximum score is 42, and the minimum score is 0.

Table 6.3. Relevant Patient Information.

Patient	**Age**	**Gender**	**NIHSS (Admit)**	**'Last Seen Normal' (with respect to imaging)**	**Stroke Location**	**Treatment**
1*	86	F	10	62 hours	Right MCA	hypertension
2	40	F	4	36 hours	Occlusion of MCA above bifurcation	Heparin
3*	57	M	Not performed	24 hours† 7 days	Multiple ACA/MCA and MCA/PCA strokes, left ICA stenosis	Anticoagulant, hypertension

* Patients that did not receive follow-up FLAIR scans.

† This patient was scanned twice due to excessive motion. This is the time of the first scan.

6.3.7. Imaging Parameters

Individual scan parameters were: FLAIR: 1.1 mm in-plane resolution, 4.4 mm slice thickness, TE/TR/TI = 100/7000/2500 ms; DTI: 2.2 mm isotropic voxels, b-value = 700 mT/m, 32 directions, TE/TR = 71/7043 ms, 70 slices acquired; PWI: 2.2x2.2x4.4 mm^3 voxels, TE/TR = 40/1500 ms, 80 dynamics acquired, 22 slices acquired. SSP-CEST was used to acquire images weighted by pH (16). SSP-CEST parameters include: 4.4 mm^3 isotropic voxels, saturation pulse duration = 25 ms, saturation pulse B_1 = 1 μT, TR/TE = 65/7 ms, 35 slices acquired. A binomial excitation pulse (1-2-1) with flip angle 12° was used for fat suppression by exciting only water spins while leaving fat spins unperturbed. One patient (patient 1) received a SSP-CEST scan that had a resolution of 2.2 mm^2 in plane, but 4.4 mm slice thickness. Pulsed CEST images were acquired at 61 frequencies: ±9 , ±7 , ±5 , ±4.5 , ±4.3 , ±4.1, ±3.9 , ±3.7, ±3.5, ±3.3, ±3.1, ±2.9, ±2.7, ±2.5, ±2.0, ±1.5, ±1.4, ±1.3, ±1.2, ±1.1, ±1.0, ±0.9, ±0.8, ±0.7, ±0.6, ±0.5, ±0.4, ±0.3, ±0.2, ±0.1, and 0 ppm (relative to the water frequency). Four unsaturated volumes were acquired with the same sequence with the RF saturation pulse turned off and averaged together to get S_0. Additionally, a navigator was acquired to correct for physiological noise (32). Total scan time for pulsed CEST was 10 minutes 34 seconds. The steady state pulsed CEST sequence is shown in figure 5.4.

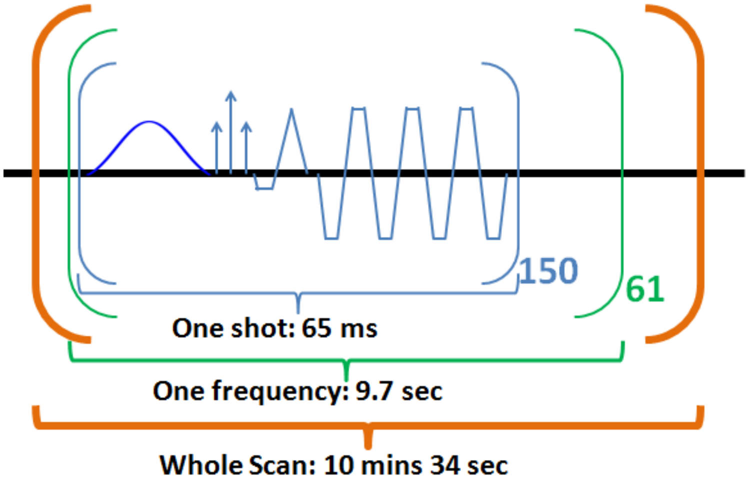

Figure 6.4. Steady-state pulsed CEST Pulse Sequence with navigator.

6.4. Data Processing

All data was processed using in-house written MATLAB® R2008a (The Mathworks, Natick, MA) routines. The different MRI modalities, DTI, FLAIR, DSC PWI, and MT-VASO, were coregistered using CATNAP (Coregistration, Adjustment, and Tensor-Solving – a Nicely Automated Program, https://masi.vuse.vanderbilt.edu/index.php/, developed at Johns Hopkins University, Baltimore, Maryland, USA, maintained by Vanderbilt University) (33). After coregistration, mean diffusion weighted (MDW), apparent diffusion coefficient (ADC), and fractional anisotropy (FA) parametric maps were generated automatically by CATNAP. Additionally, the images were skull-stripped using the brain extraction algorithm from FSL (34).

6.4.1. Pulsed CEST data processing

The pulsed CEST data were processed on a voxel-wise basis as follows: 1) The center frequency shift map was determined by fitting a Lorentzian lineshape to a sub-spectrum of the following frequencies: ±9 , ±7 , ±5, ±1.0, ±0.9, ±0.8, ±0.7, ±0.6, ±0.5, ±0.4, ±0.3, ±0.2, ±0.1, and 0 ppm (known as the Lorentzian Difference Analysis (LDA)) (23). 2) Using the center frequency shift map, the z-spectra were shifted so that the center frequency of each voxel was at 0 ppm. 3) Next, magnetization transfer ratios, (MTR) at +3.5 ppm and -3.5 ppm were calculated by averaging signal intensities at ±3.7, ±3.5, and ±3.3 ppm. 4) MTR asymmetry ($MTR_{asymmetry}$(+3.5 ppm)) maps were calculated by subtracting MTR(-3.5 ppm) from MTR(+3.5 ppm) (12). 5) Finally, APT and NOE maps were calculated by averaging the LDA(+3.3, +3.5, +3.7) and LDA(-2, -2.5, -2.7, -2.9, -3.1, -3.3, -3.5, -3.7, -3.9, -4.1, -4.5, -5), respectively.

6.4.2. Determination of DWI lesions

Voxels exhibiting signal intensity greater than one and a half standard deviations above the mean of the mean diffusion image were designated as diffusion lesions.

6.4.3. Perfusion Weighted Imaging Data Processing

PWI data were computed on a voxel-wise basis to generate a time to peak (TTP) map for each patient. For one stroke patient, the TTP map was further processed by generating a TTP delay map using the contralateral normally perfused tissue as reference (35). Furthermore, cutoffs of the TTP delay map were applied at ≥2, ≥3, ≥4, ≥5, and ≥6 seconds. These cutoffs were chosen because recent publications comparing PET and MR methods for identifying penumbral blood flow have confirmed that a TTP delay of four seconds corresponds closely to the PWI penumbra (35-37). The other stroke patient did not have a pH-weighted lesion so we did not perform this analysis for that patient.

6.4.4. Estimation of Infarct Percentage

To study how the pH penumbra estimates tissue at risk of infarction differently than the PWI penumbra, we applied two thresholds ($MTR_{asymmetry}(+3.5\ \text{ppm}) \leq -2$ and $MTR_{asymmetry}(+3.5\ \text{ppm}) \leq -3$) to determine the pH penumbra for the stroke patient that had a pH lesion and overlapped the pH penumbra mask with maps at the different TTP delay cutoffs.

6.5. Results and Discussion

6.5.1. CEST Baseline Correction

Results of the 65 minute scan to analyze scanner drift can be seen in figure 6.5.

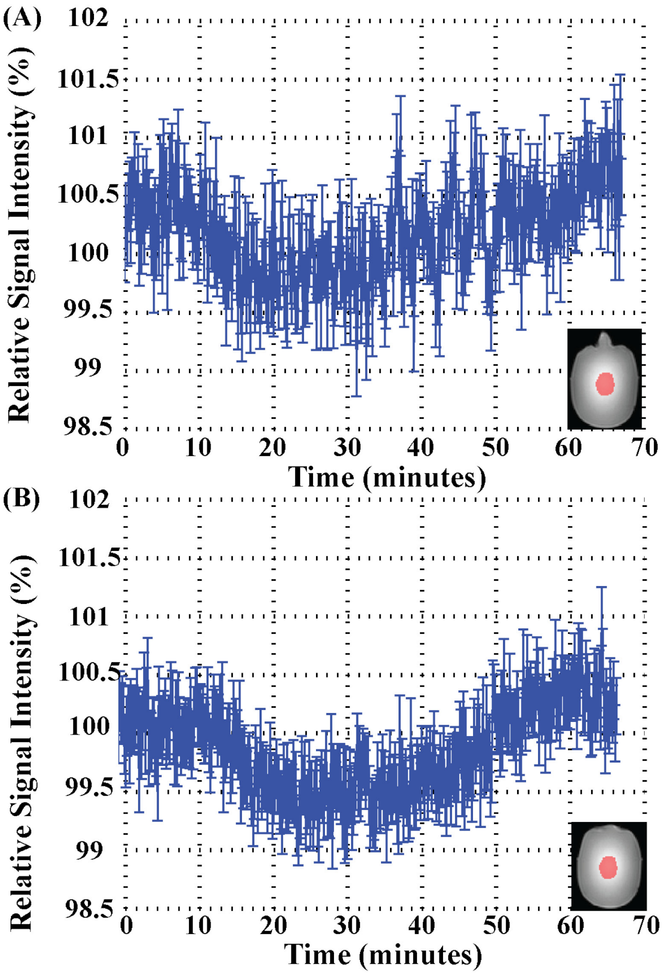

Figure 6.5. Scanner Drift (A) XMR (B) MR1

It can be seen that scanner drift can potentially shift relative signal intensities by ±1%. However, this is problematic because small changes in pH are reflected in changes of a fraction of a percent in the APT signal (refer to figure 6.2).

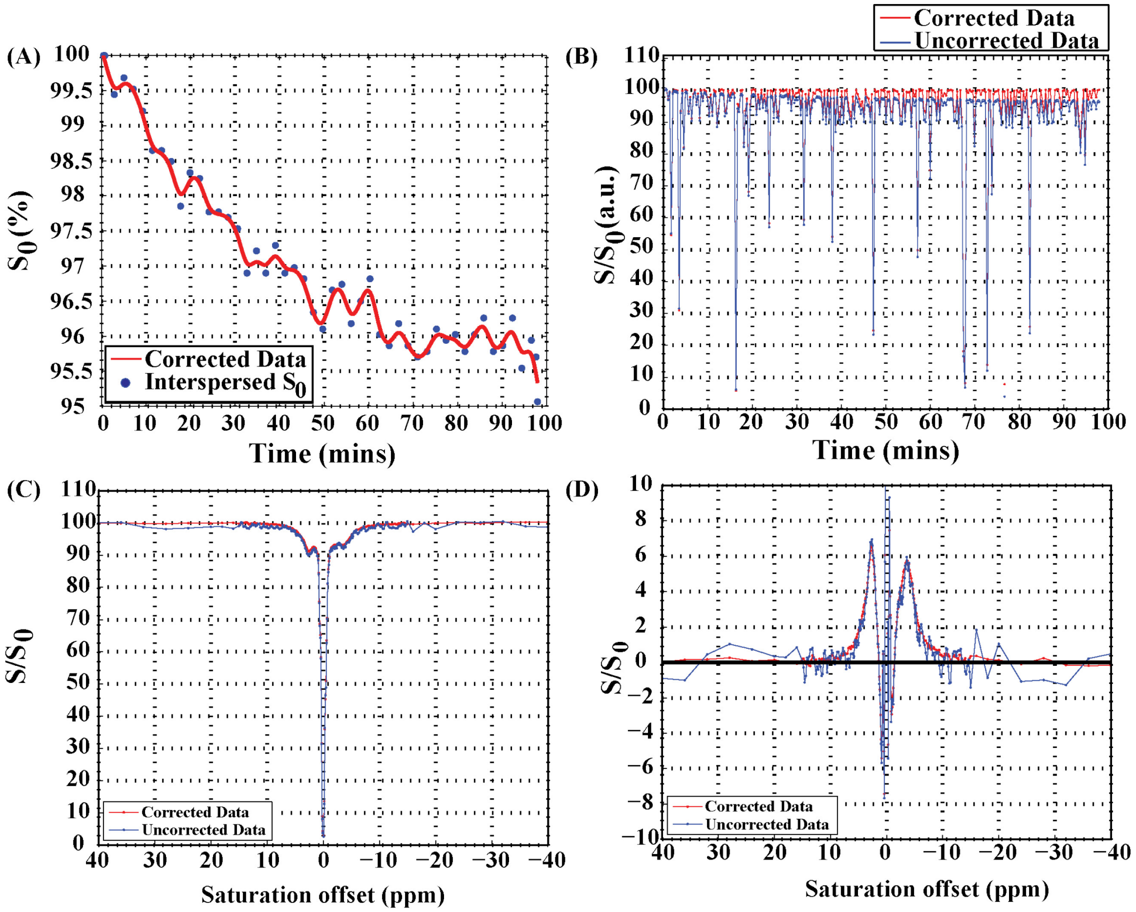

Figure 6.6. CEST Baseline Correction: Comparison of Corrected and Uncorrected for pH 6.3 10% BSA phantom. (A) S_0 points and Fitted Spline (B) Corrected and Uncorrected Acquired Data (C) Uncorrected and Baseline Corrected CEST spectra (D) Uncorrected and Corrected LDA

The proposed method for CEST baseline correction was applied to pH phantoms and worked well to correct baseline inconsistencies. In figure 6.6A, the S0 points are displayed as blue points and a smooth spline (red line) is fitted through those points as a function of time. In figure 6.6B, the uncorrected and corrected data are displayed in blue and red, respectively. Notice how the blue line drifts down approximately 5%. The baseline CEST correction method corrects this to ensure that normalized S_0 intensities remain at 100%. Figure 6.6C shows the CEST spectra before and after baseline correction. The uncorrected data (blue line) is noticeably noisier towards the ends (points greater than 10 ppm and less than -10 ppm) of the spectrum. The Lorentzian Difference Analysis (LDA) can be performed to analyze CEST effects. The LDA for uncorrected and baseline corrected CEST spectra is shown in figure 6.6D. After subtracting the raw data from the fitted Lorentzian, the baseline corrected CEST spectra yields a clean baseline.

6.5.2. Phantom Study

Figure 6.7 shows the results of the phantom study.

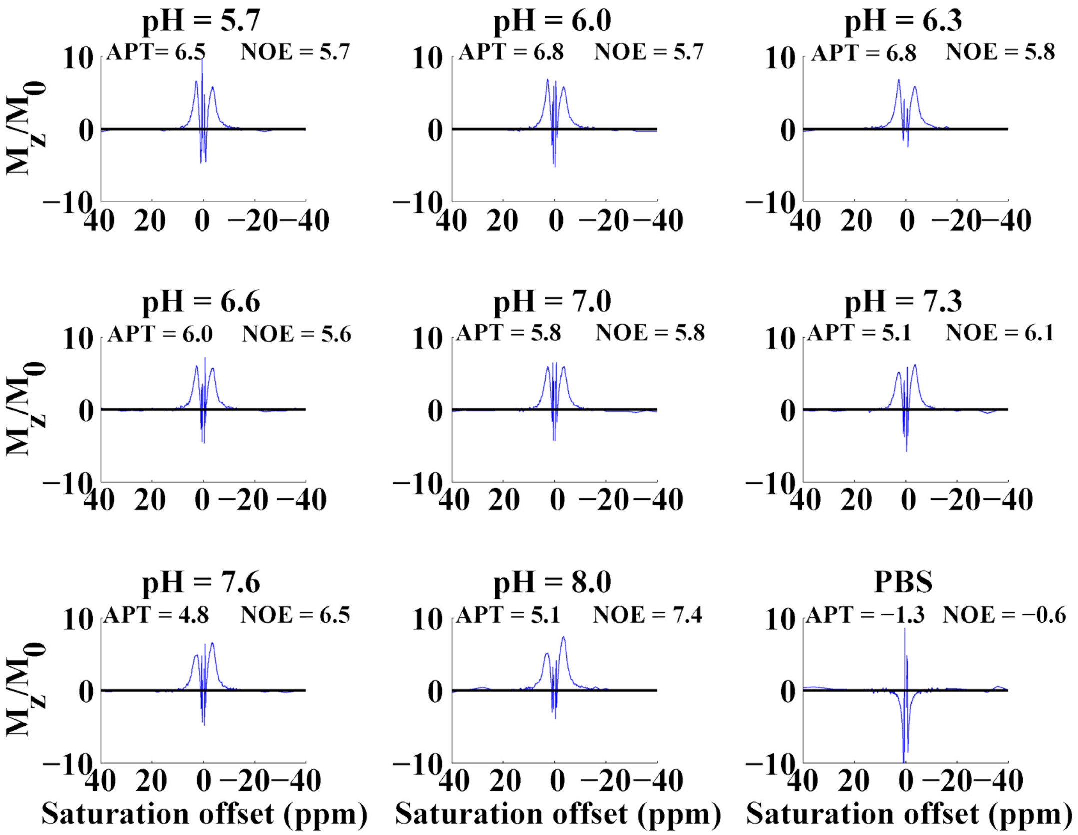

Figure 6.7. Lorentzian Difference Analysis (LDA) of the different pH phantoms. In this figure, APEX is defined as amine proton exchange, which is the average of the LDA at (ω=+2.5, +2.6, +2.7, +2.8, and +2.9 ppm), and NOE is defined as the Nuclear Overhauser Effects, which is the average of the LDA at (ω=-2.9, -2.8, -2.7, -2.6, and -2.5 ppm).

The Lorentzian Difference Analysis gives us a clear distinction of exchangeable protons in BSA. Two main peaks are seen: one from amines and amides (downfield from water) and one from Nuclear Overhauser Effects (NOE) (upfield from water). Additionally, a correlation plot was made to verify that the steady state pulsed CEST sequence was indeed sensitive to differences in pH. Figure 6.8 shows the correlation of pH versus Lorentzian Difference Analysis.

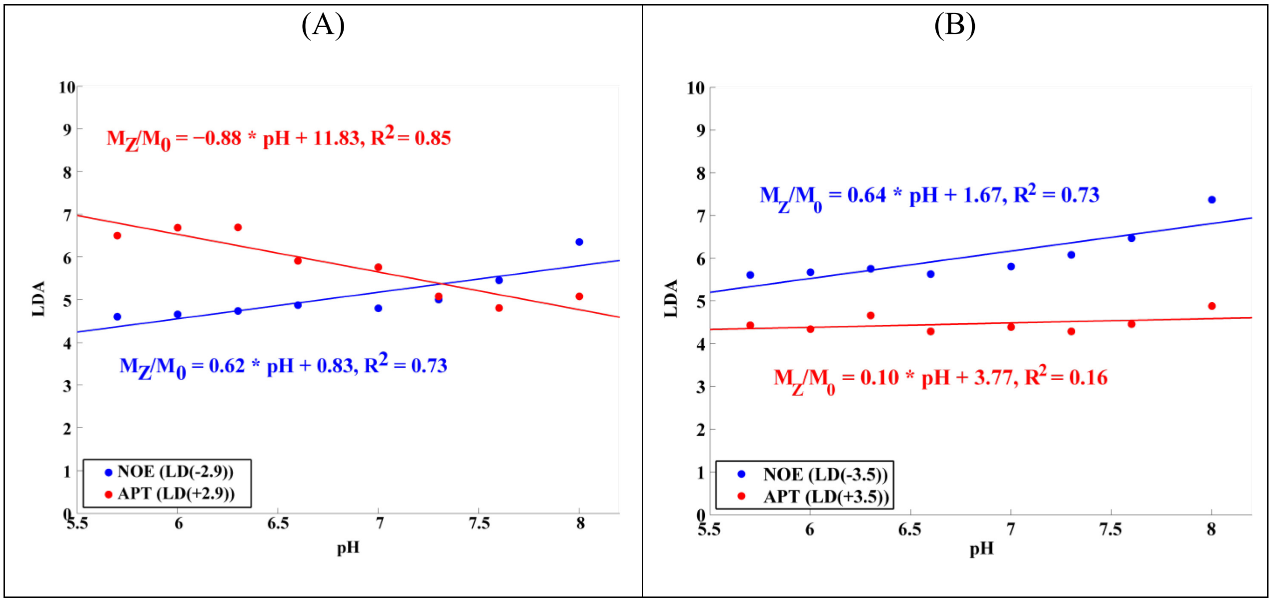

Figure 6.8. Correlation Graph of pH versus Lorentzian Difference (A) at Δω=±2.9 ppm; and (B) at Δω=±3.5 ppm.

Figure 6.8A shows that amine protons, which resonate 2.9 ppm downfield from water, show a strong negative pH dependence, which is expected based on current literature (24) yet NOEs show a strong positive pH dependence. In figure 6.8B, amide protons show a weaker positive pH dependence yet NOEs still show a strong positive pH dependence. This is important because traditionally analysis of CEST spectra was performed using $MTR_{asymmetry}$. However, if there is pH dependence in both the $S_{sat}(-\Delta\omega)$ and $S_{sat}(\Delta\omega)$ terms, then care should be taken when interpreting the combination of these images.

6.5.3. Controls

Data from all controls did not have hyperintensities in mean diffusion weighted images and FLAIR images (in other words, control data was diffusion and

FLAIR negative). Figures 6.9 and 6.10 present results from two of the controls over six slices that cover the whole brain. pH-weighted images (MTR$_{asymmetry}$(3.5 ppm), APT, and NOE) also show symmetry between the right and left hemispheres and in both datasets.

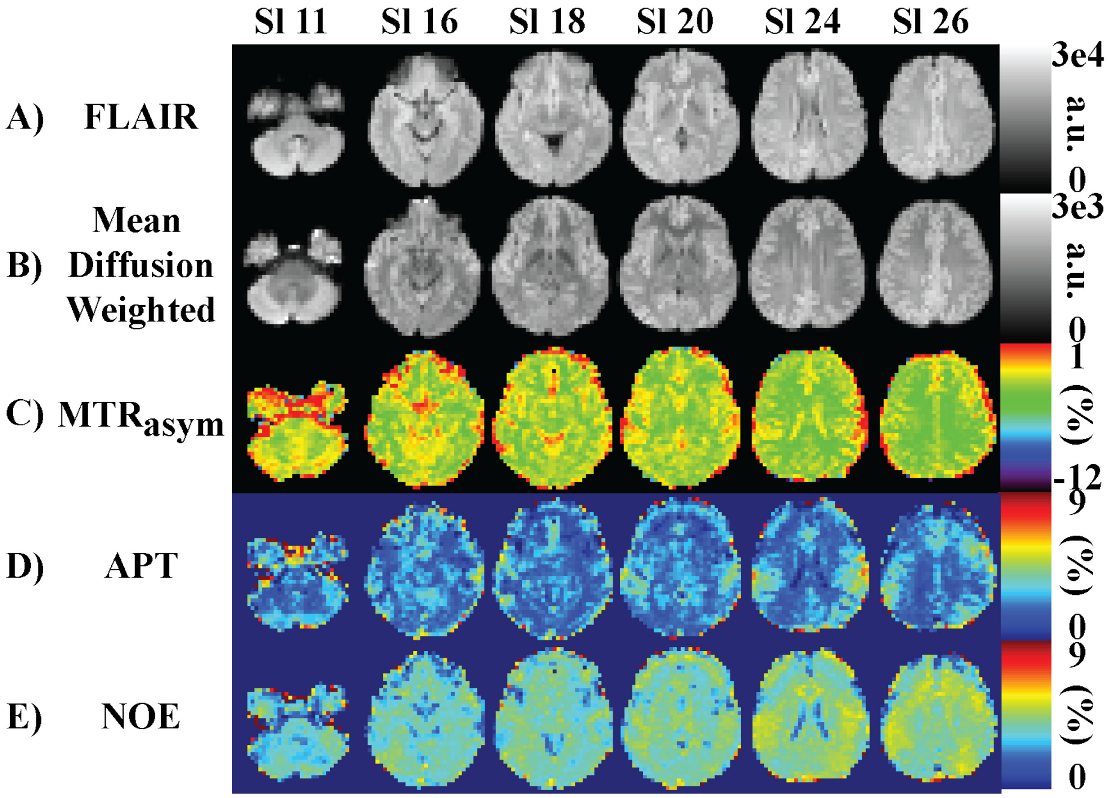

Figure 6.9. Data acquired on a healthy control subject. Select slices from the (A) FLAIR scan, (B) Mean Diffusion Weighted Image, (C) MTR$_{asymmetry}$(3.5 ppm) processed from the Steady State Pulsed CEST (pH-weighted), (D) APT processed from the Steady State Pulsed CEST scan, and (E) NOE processed from the Steady State Pulsed CEST scan.

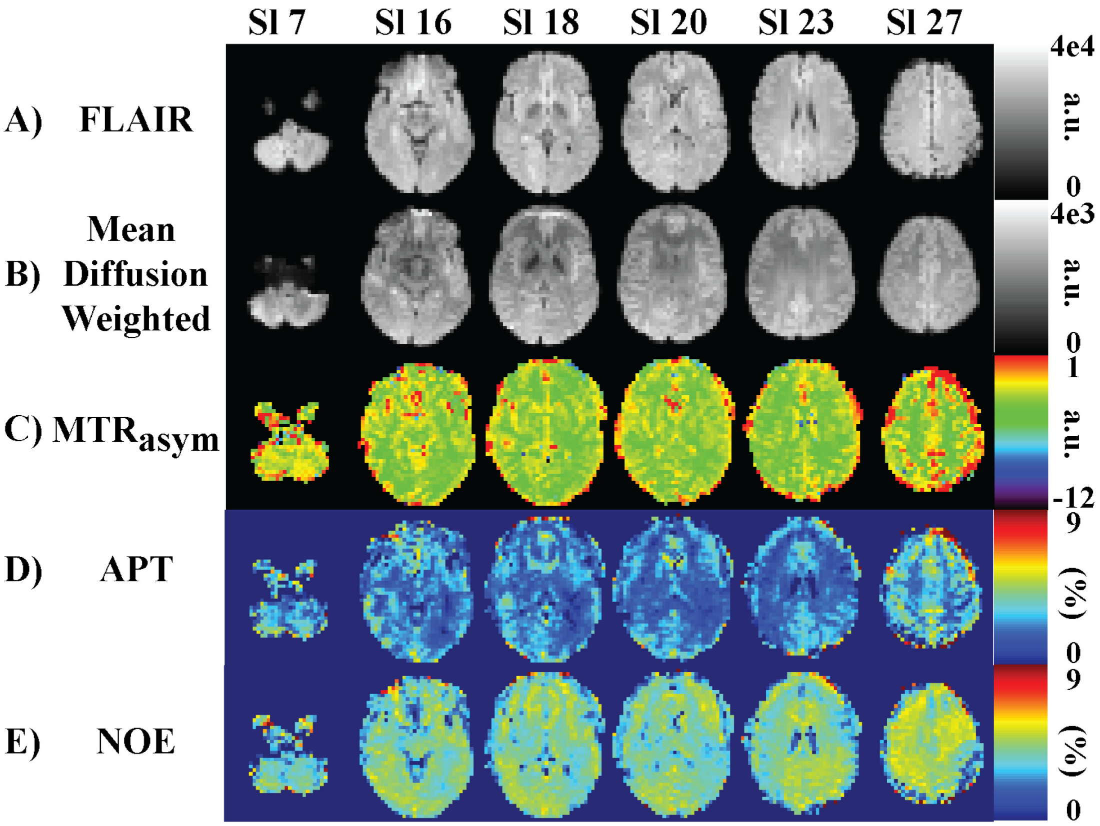

Figure 6.10. Data acquired on another healthy control subject. Select slices from the (A) FLAIR scan, (B) Mean Diffusion Weighted Image, (C) $\text{MTR}_{\text{asymmetry}}$(3.5 ppm) processed from the Steady State Pulsed CEST (pH-weighted), (D) APT processed from the Steady State Pulsed CEST scan, and (E) NOE processed from the Steady State Pulsed CEST scan.

6.5.4. Patient 1

Figure 6.11 shows data for an 84 year old female imaged 62 hours after symptoms onset, presented with several diffusion positive regions (Figure 6.11A) and a perfusion deficit covering the entire vascular territory of the right anterior cerebral artery (Figure 6.11B) in the acute scan. This can be seen by an increase in the time to peak of the patient's right hemisphere (left in image; radiological convention). In figure 6.12, a healthy control's $\mathrm{MTR}_{\mathrm{asymmetry}}$(+3.5 ppm) image (Figure 6.12A) is compared to the patient's $\mathrm{MTR}_{\mathrm{asymmetry}}$(+3.5 ppm) image (Figure 6.12B) over a similar region of interest. Notice that the healthy control's $\mathrm{MTR}_{\mathrm{asymmetry}}$(+3.5 ppm) image is symmetric between the two hemispheres whereas the ischemic patient's $\mathrm{MTR}_{\mathrm{asymmetry}}$(+3.5 ppm) image is asymmetric because of possible tissue acidosis in the right hemisphere.

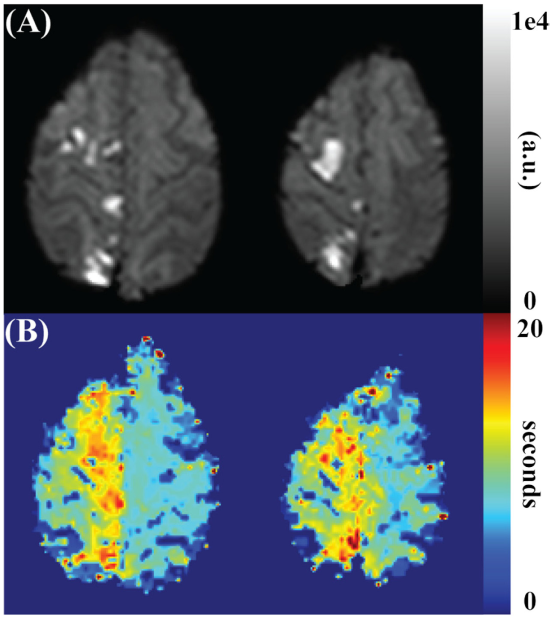

Figure 6.11. (A) Diffusion weighted scan (mean diffusion weighted image) and (B) Perfusion weighted scan of ischemic stroke patient (time to peak image).

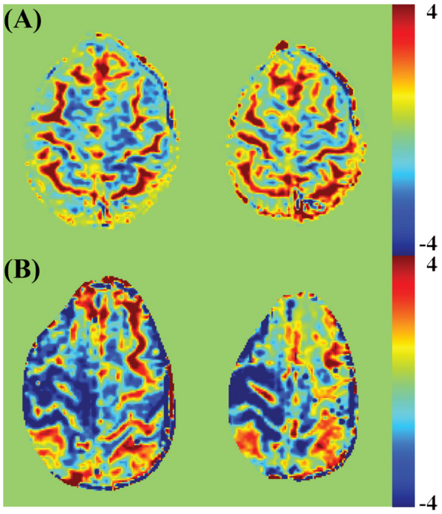

Figure 6.12. MTR$_{asymmetry}$ (+3.5 ppm) image of (A) healthy volunteer and (B) ischemic stroke patient.

In figure 6.13, two different thresholds for the pH weighted images from patient 1 are used (Figure 6.13A: MTR$_{asymmetry}$ (+3.5 ppm) $\leq$ -3 and figure 6.13B: MTR$_{asymmetry}$ (+3.5 ppm)$\leq$ -2) to determine the pH penumbra. Notice that the pH penumbra is contained around the diffusion lesions. Additionally, the PWI penumbra appears to overestimate the tissue at risk of infarction.

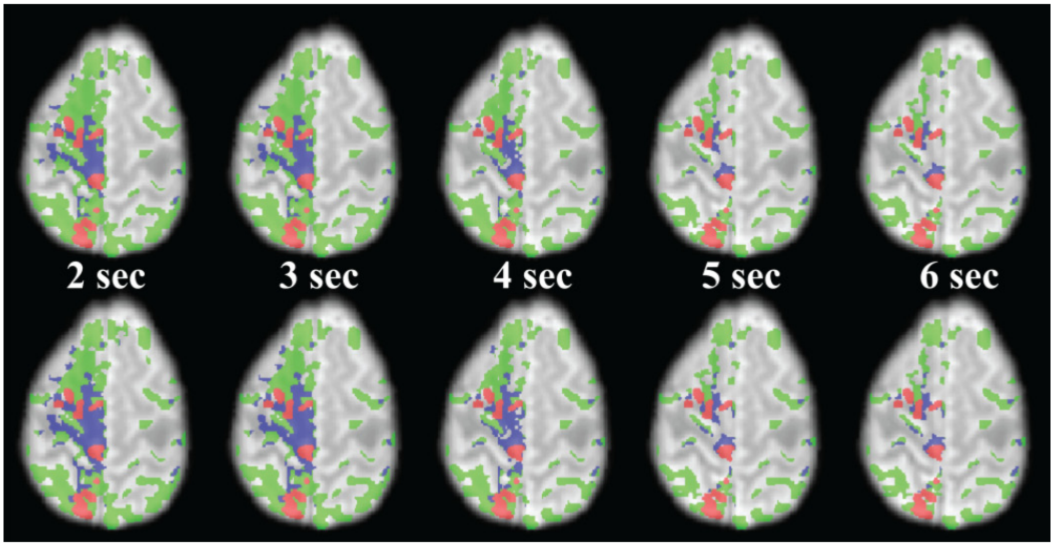

Figure 6.13. Images of diffusion lesion (red), possible pH penumbra (blue), and perfusion penumbra (green) overlaid on CEST M_0 image. Top row: pH penumbra was determined with $MTR_{asymmetry}(+3.5\ ppm) \leq -3$. Bottom row: pH penumbra was determined with $MTR_{asymmetry}\ (+3.5\ ppm) \leq -2$.

Unfortunately, this patient did not receive a follow-up FLAIR scan so we could not correlate whether or not the region found to have reduced pH progressed to infarction.

6.5.5. Patient 2

This patient presented with right middle cerebral artery (MCA) infarct and right carotid artery occlusion. Figures 6.14 and 6.15 display this patient's acute FLAIR scan (figure 6.14A&6.15A), acute mean diffusion weighted scan (figure 6.14B&6.15B), time to peak image (figure 6.14C&6.15C), $MTR_{asymmetry}(3.5\ ppm)$ (figure 6.14D&6.15D), APT (figure 6.14E&6.15E), NOE (figure 6.14F&6.15F) and follow-up FLAIR scan (figure 6.14G&6.15G).

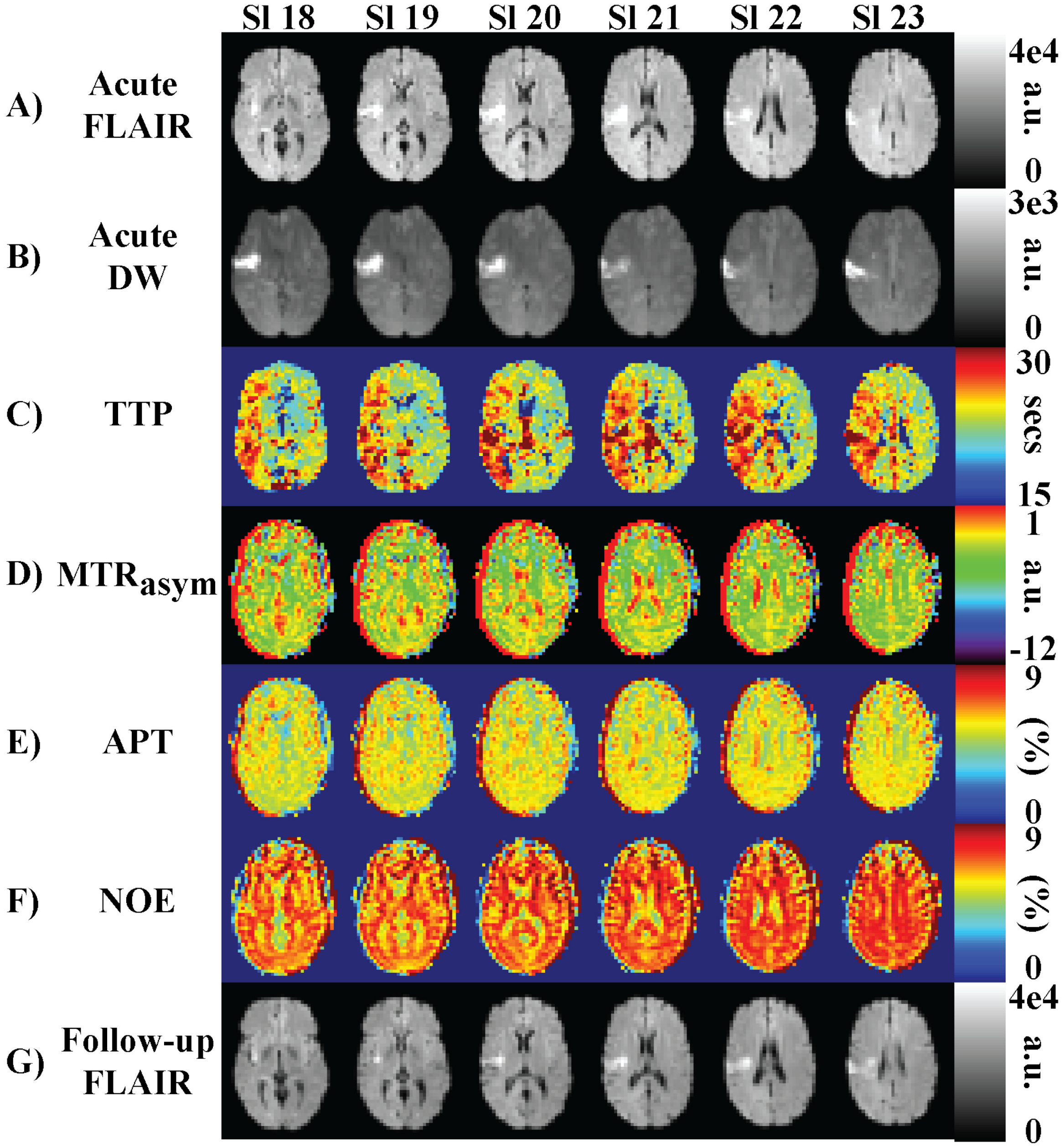

Figure 6.14. Slices 18 to 23 for Patient 1. (A) Acute FLAIR scan. (B) Acute mean diffusion weighted image. (C) Time-to-peak image. (D) $\text{MTR}_{\text{asymmetry}}$(3.5 ppm). (E) APT. (F) NOE (G) Follow-up FLAIR.

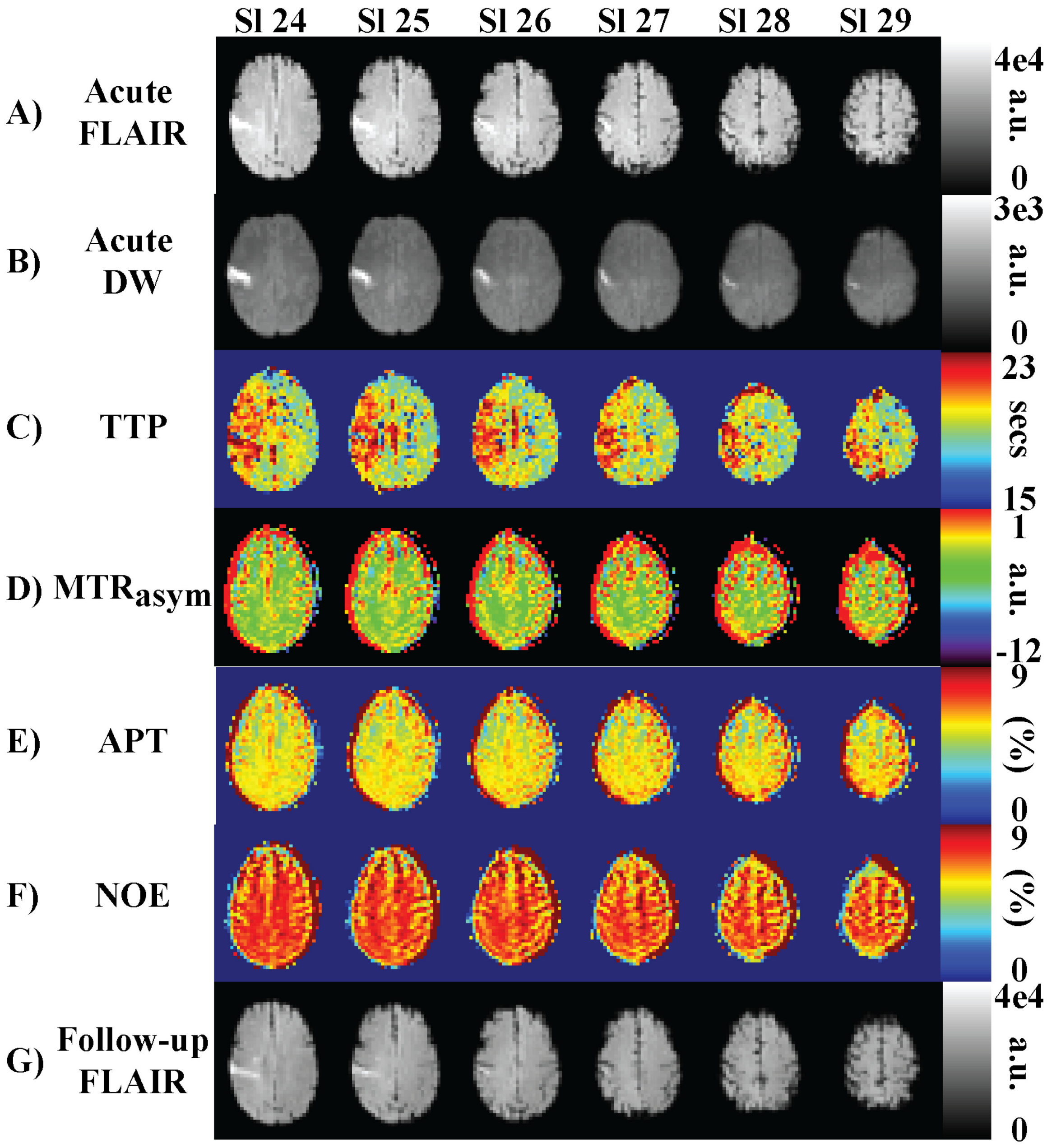

Figure 6.15. Slices 24 to 29 for Patient 2. (A) Acute FLAIR scan. (B) Acute mean diffusion weighted image. (C) Time-to-peak image. (D) $MTR_{asymmetry}$(3.5 ppm). (E) APT. (F) NOE (G) Follow-up FLAIR.

Notice in the acute FLAIR scan, the hyperintensity is evidence that tissue T_2 has already begun to change in the hyperintense region of the mean diffusion weighted image. However, the time to peak image shows an asymmetry in cerebral perfusion between the two hemispheres. Furthermore, the hyperintense region in the time to peak image is significantly larger than the diffusion lesion (a diffusion-perfusion mismatch), which would imply that there is a large region of tissue at risk of infarction. However, when analyzing the pH-weighted images ($MTR_{asymmetry}$(3.5 ppm), APT, and NOE), the two hemispheres appear symmetric implying that the hyperintense region in the time to peak is benign oligemia. This is confirmed in the follow-up FLAIR images where final infarct region is limited to the original lesion on the diffusion–weighted image.

6.5.6. Patient 3

This patient (57 year old male) presented with aphasia and right side weakness. Acute MRI confirmed a previous stroke in the right hemisphere and acute infarcts in the left watershed distribution region followed with a much larger region of reduced perfusion at risk of infarction. We were interested in understanding whether or not this patient's perfusion deficit would progress to infarction so the patient was scanned using the acute stroke MRI protocol with pH-weighted imaging. This patient received a scan 24 hours after being admitted. However, this patient was uncooperative and moved around a lot during the initial scan. He was taken out of the scanner and scanned seven days later. An example of the motion is shown in figure 6.16 on the DTI scan. Figures 6.17-6.19 detail the results of the scans performed seven days after the initial scan.

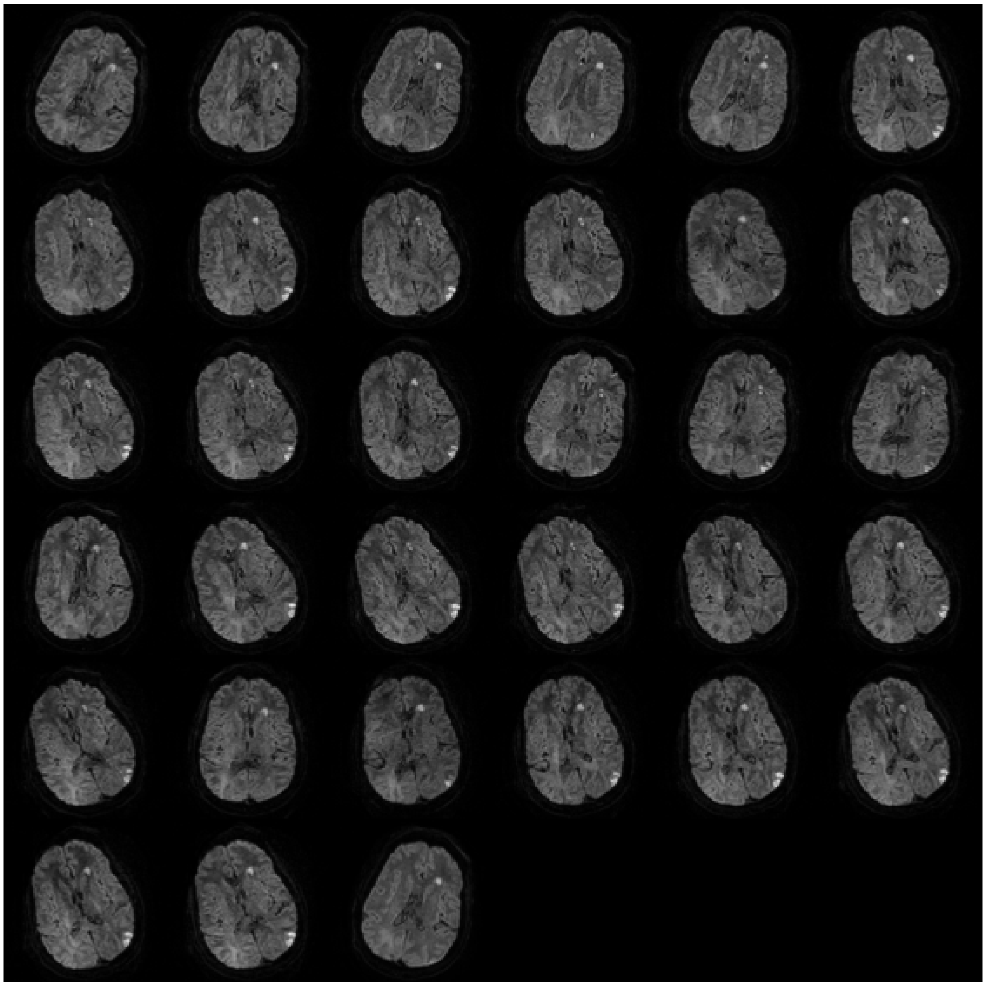

Figure 6.16. Example of patient motion on DTI scan. This image contains a single slice of the DTI scan. The 33 images are from the different gradient directions that were acquired. The B_0 image was left off of this image so signal intensity scaling could be maintained at one level for this group of images.

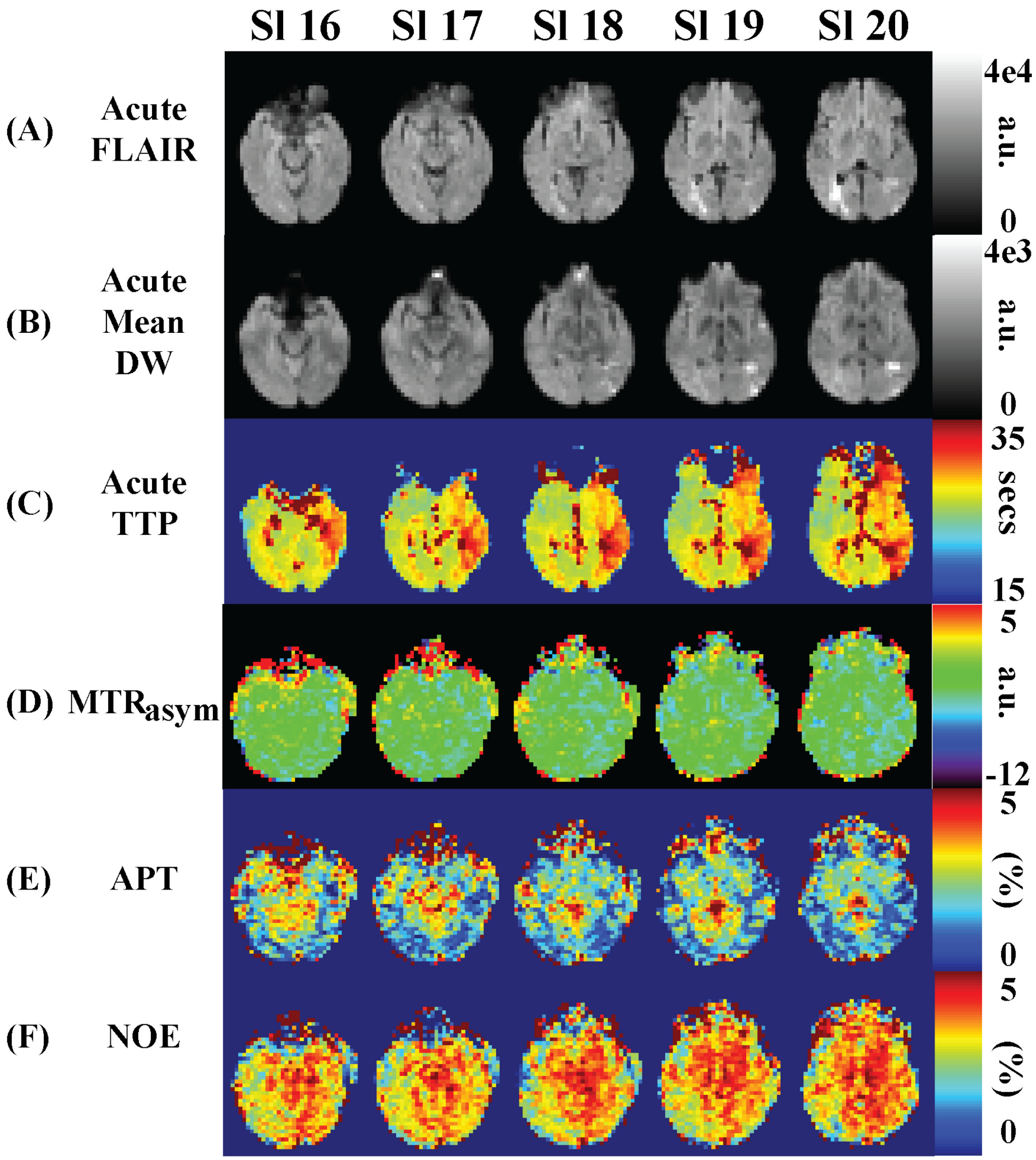

Figure 6.17. Processed data for carotid artery stenosis patient (Slices 16-20) (displayed in radiologic convention). (A) Acute FLAIR scan (B) Acute Mean Diffusion Weighted scan (C) Acute Time to Peak scan (D) $\mathrm{MTR}_{\mathrm{asymmetry}}$(3.5 ppm) (pH-weighted) (E) APT (F) NOE

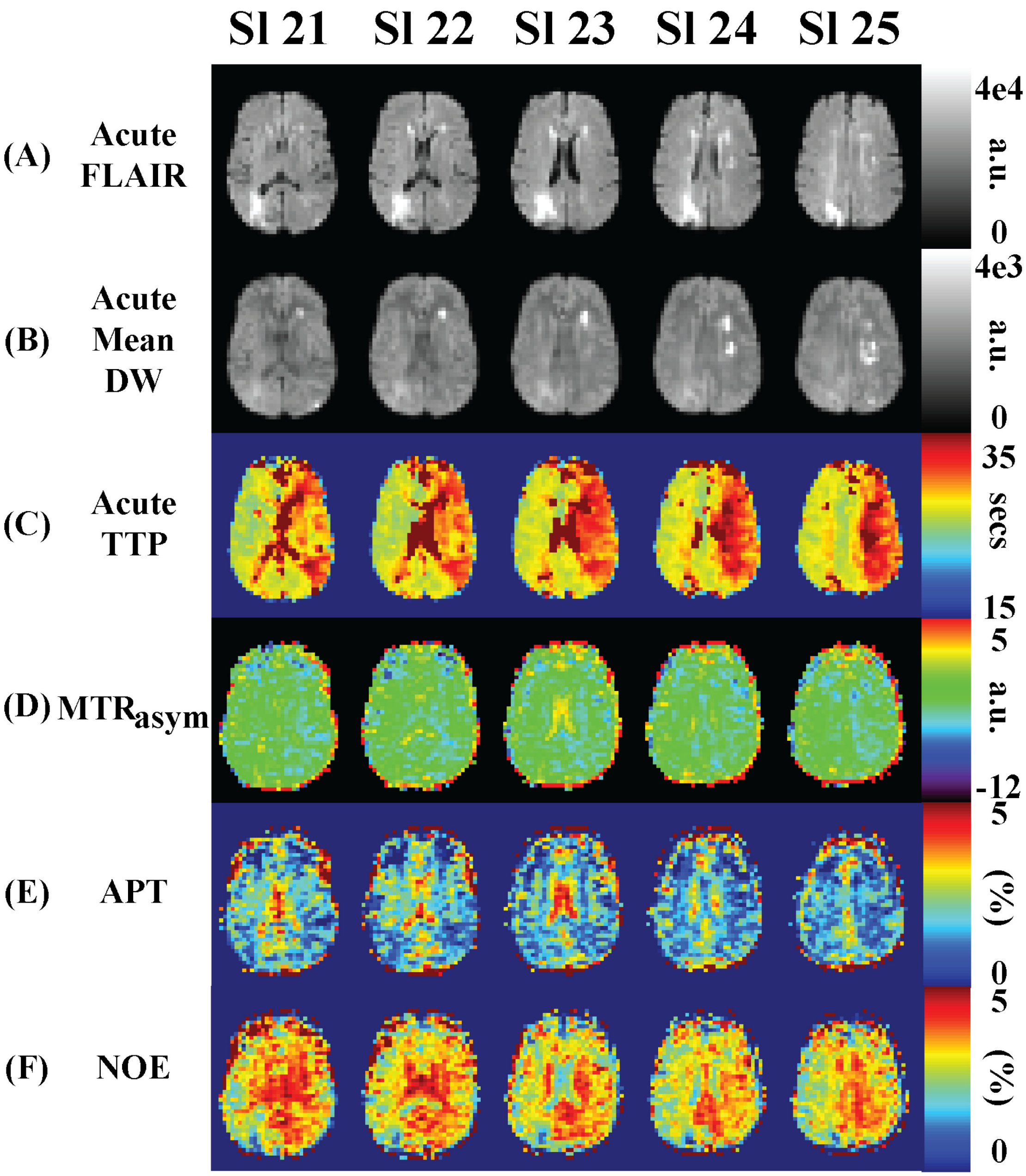

Figure 6.18. Processed data for carotid artery stenosis patient (Slices 21-25) (displayed in radiologic convention). (A) Acute FLAIR scan (B) Acute Mean Diffusion Weighted scan (C) Acute Time to Peak scan (D) $\text{MTR}_{\text{asymmetry}}$(3.5 ppm) (pH-weighted) (E) APT (F) NOE

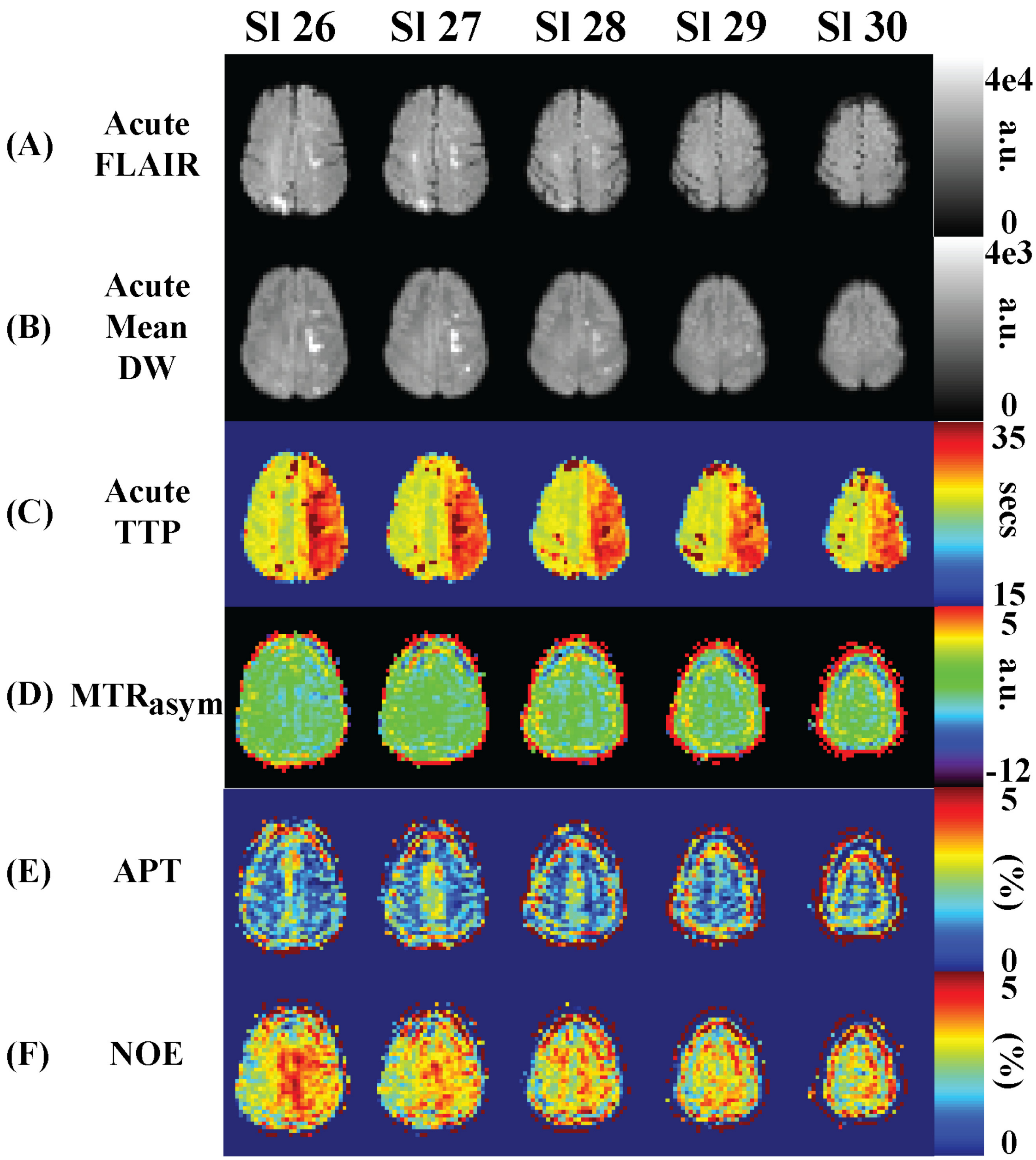

Figure 6.19. Processed data for carotid artery stenosis patient (Slices 26-30) (displayed in radiologic convention). (A) Acute FLAIR scan (B) Acute Mean Diffusion Weighted scan (C) Acute Time to Peak scan (D) MTR$_{asymmetry}$(3.5 ppm) (pH-weighted) (E) APT (F) NOE

The patient's old stroke in the right parietal-occipital region can be seen in the FLAIR scan between slices 18-28. Mean diffusion weighted images show hyperintensities between slices 18-29 in the left hemisphere, and time to peak images show a large region at risk of infarction covering the entire MCA distribution on the left hemisphere. $\mathrm{MTR}_{\mathrm{asymmetry}}$(3.5 ppm) images shows regions of possible reductions in pH. These regions appear to be smaller in size than the perfusion deficit, which may indicate that not all tissue that is indicated to be hypoperfused by the time to peak image is at risk of infarction.

6.6. Conclusion

We present an initial application of using pulsed CEST to image different pHs in 10% BSA pH phantoms and translated this to healthy volunteers and eventually to acute ischemic stroke patients. Comparison of $\mathrm{MTR}_{\mathrm{asymmetry}}$(+3.5 ppm) images between a healthy volunteer and an ischemic stroke patient showed a reduction in the $\mathrm{MTR}_{\mathrm{asymmetry}}$(+3.5 ppm) in the region of delayed perfusion that was attributed to tissue acidosis, and comparison of the pH penumbra to the PWI penumbra (by using different TTP delay thresholds) shows that the pH penumbra localizes a region smaller than the PWI penumbra. Therefore, APT MRI shows sensitivity to pH changes that are not visible using diffusion or perfusion imaging. A patient with a large perfusion penumbra that was believed to be benign oligemia was also imaged. pH-weighted imaging ($\mathrm{MTR}_{\mathrm{asymmetry}}$(+3.5 ppm)) showed symmetric hemispheres similar to what was seen for normal volunteers. Follow-up FLAIR imaging confirmed that the large perfusion penumbra was indeed benign oligemia as infarction was confined to regions of diffusion hyperintensities. And finally, pulsed CEST was applied to a patient with a stenosed left internal carotid artery that appeared to localize pH changes around diffusion lesions.

6.7. References

1. Mathers CD, Loncar D. Projections of global mortality and burden of disease from 2002 to 2030. PLoS Med. 2006;3(11):e442.
2. Rymer MM, Thrutchley DE. Organizing regional networks to increase acute stroke intervention. Neurol Res. 2005;27 Suppl 1:S9-16.
3. Furlan A, Higashida R, Wechsler L, Gent M, Rowley H, Kase C, Pessin M, Ahuja A, Callahan F, Clark WM, Silver F, Rivera F. Intra-arterial prourokinase for acute ischemic stroke. The PROACT II study: a randomized controlled trial. Prolyse in Acute Cerebral Thromboembolism. JAMA. 1999;282(21):2003-11.
4. Knight RA, Barker PB, Fagan SC, Li Y, Jacobs MA, Welch KM. Prediction of impending hemorrhagic transformation in ischemic stroke using magnetic resonance imaging in rats. Stroke. 1998;29(1):144-51.
5. Brinker G, Pillekamp F, Hossmann KA. Brain hemorrhages after rt-PA treatment of embolic stroke in spontaneously hypertensive rats. Neuroreport. 1999;10(9):1943-6.
6. Busch E, Kruger K, Allegrini PR, Kerskens CM, Gyngell ML, Hoehn-Berlage M, Hossmann KA. Reperfusion after thrombolytic therapy of embolic stroke in the rat: magnetic resonance and biochemical imaging. J Cereb Blood Flow Metab. 1998;18(4):407-18.
7. Hacke W, Donnan G, Fieschi C, Kaste M, von Kummer R, Broderick JP, Brott T, Frankel M, Grotta JC, Haley EC, Jr., Kwiatkowski T, Levine SR, Lewandowski C, Lu M, Lyden P, Marler JR, Patel S, Tilley BC, Albers G, Bluhmki E, Wilhelm M,

Hamilton S. Association of outcome with early stroke treatment: pooled analysis of ATLANTIS, ECASS, and NINDS rt-PA stroke trials. Lancet. 2004;363(9411):768-74.

8. Blakeley JO, Llinas RH. Thrombolytic therapy for acute ischemic stroke. J Neurol Sci. 2007;261(1-2):55-62.
9. Ostergaard L, Weisskoff RM, Chesler DA, Gyldensted C, Rosen BR. High resolution measurement of cerebral blood flow using intravascular tracer bolus passages. Part I: Mathematical approach and statistical analysis. Magn Reson Med. 1996;36(5):715-25.
10. Ostergaard L, Sorensen AG, Kwong KK, Weisskoff RM, Gyldensted C, Rosen BR. High resolution measurement of cerebral blood flow using intravascular tracer bolus passages. Part II: Experimental comparison and preliminary results. Magn Reson Med. 1996;36(5):726-36.
11. Kucinski T, Naumann D, Knab R, Schoder V, Wegener S, Fiehler J, Majumder A, Rother J, Zeumer H. Tissue at risk is overestimated in perfusion-weighted imaging: MR imaging in acute stroke patients without vessel recanalization. AJNR Am J Neuroradiol. 2005;26(4):815-9.
12. Zhou J, Payen JF, Wilson DA, Traystman RJ, van Zijl PC. Using the amide proton signals of intracellular proteins and peptides to detect pH effects in MRI. Nature medicine. 2003;9(8):1085-90.
13. Ward KM, Balaban RS. Determination of pH using water protons and chemical exchange dependent saturation transfer (CEST). Magn Reson Med. 2000;44(5):799-802.
14. Zhou J, van Zijl PC. Defining an Acidosis-Based Ischemic Penumbra from pH-Weighted MRI. Translational stroke research. 2011;3(1):76-83.

15. Sun PZ, Zhou J, Sun W, Huang J, van Zijl PC. Detection of the ischemic penumbra using pH-weighted MRI. J Cereb Blood Flow Metab. 2007;27(6):1129-36.
16. Bryant RG. The dynamics of water-protein interactions. Annual review of biophysics and biomolecular structure. 1996;25:29-53.
17. Pekar J, Jezzard P, Roberts DA, Leigh JS, Jr., Frank JA, McLaughlin AC. Perfusion imaging with compensation for asymmetric magnetization transfer effects. Magn Reson Med. 1996;35(1):70-9.
18. Hua J, Jones CK, Blakeley J, Smith SA, van Zijl PC, Zhou J. Quantitative description of the asymmetry in magnetization transfer effects around the water resonance in the human brain. Magn Reson Med. 2007;58(4):786-93.
19. Ling W, Regatte RR, Navon G, Jerschow A. Assessment of glycosaminoglycan concentration in vivo by chemical exchange-dependent saturation transfer (gagCEST). Proc Natl Acad Sci U S A. 2008;105(7):2266-70.
20. Mori S, Eleff SM, Pilatus U, Mori N, van Zijl PC. Proton NMR spectroscopy of solvent-saturable resonances: a new approach to study pH effects in situ. Magn Reson Med. 1998;40(1):36-42.
21. van Zijl PC, Zhou J, Mori N, Payen JF, Wilson D, Mori S. Mechanism of magnetization transfer during on-resonance water saturation. A new approach to detect mobile proteins, peptides, and lipids. Magn Reson Med. 2003;49(3):440-9.
22. van Zijl PC, Yadav NN. Chemical exchange saturation transfer (CEST): what is in a name and what isn't? Magn Reson Med. 2011;65(4):927-48.

23. Jones CK, Polders D, Hua J, Zhu H, Hoogduin HJ, Zhou J, Luijten P, van Zijl PC. In vivo three-dimensional whole-brain pulsed steady-state chemical exchange saturation transfer at 7 T. Magn Reson Med. 2012;67(6):1579-89.

24. Jin T, Wang P, Zong X, Kim SG. Magnetic resonance imaging of the Amine-Proton EXchange (APEX) dependent contrast. Neuroimage. 2012;59(2):1218-27.

25. Desmond KL, Stanisz GJ. Understanding quantitative pulsed CEST in the presence of MT. Magn Reson Med. 2012;67(4):979-90.

26. Song X, Gilad AA, Joel S, Liu G, Bar-Shir A, Liang Y, Gorelik M, Pekar JJ, van Zijl PC, Bulte JW, McMahon MT. CEST phase mapping using a length and offset varied saturation (LOVARS) scheme. Magn Reson Med. 2012;68(4):1074-86.

27. Woessner DE, Zhang S, Merritt ME, Sherry AD. Numerical solution of the Bloch equations provides insights into the optimum design of PARACEST agents for MRI. Magn Reson Med. 2005;53(4):790-9.

28. Barnett HJM. Stroke : pathophysiology, diagnosis, and management. 3rd ed. New York: Churchill Livingstone; 1998. xxiv, 1459 p., 12 p. of plates p.

29. Kraig RP, Pulsinelli WA, Plum F. Hydrogen ion buffering during complete brain ischemia. Brain Res. 1985;342(2):281-90.

30. Donahue MJ, Lu H, Jones CK, Edden RA, Pekar JJ, van Zijl PC. Theoretical and experimental investigation of the VASO contrast mechanism. Magn Reson Med. 2006;56(6):1261-73.

31. Zhou J, Wilson DA, Sun PZ, Klaus JA, Van Zijl PC. Quantitative description of proton exchange processes between water and endogenous and exogenous agents for WEX, CEST, and APT experiments. Magn Reson Med. 2004;51(5):945-52.

32. Versluis MJ, Peeters JM, van Rooden S, van der Grond J, van Buchem MA, Webb AG, van Osch MJ. Origin and reduction of motion and f0 artifacts in high resolution T2*-weighted magnetic resonance imaging: application in Alzheimer's disease patients. Neuroimage. 2010;51(3):1082-8.

33. Farrell JA, Landman BA, Jones CK, Smith SA, Prince JL, van Zijl PC, Mori S. Effects of signal-to-noise ratio on the accuracy and reproducibility of diffusion tensor imaging-derived fractional anisotropy, mean diffusivity, and principal eigenvector measurements at 1.5 T. J Magn Reson Imaging. 2007;26(3):756-67.

34. Smith SM. Fast robust automated brain extraction. Hum Brain Mapp. 2002;17(3):143-55.

35. Neumann-Haefelin T, Wittsack HJ, Wenserski F, Siebler M, Seitz RJ, Modder U, Freund HJ. Diffusion- and perfusion-weighted MRI. The DWI/PWI mismatch region in acute stroke. Stroke. 1999;30(8):1591-7.

36. Sobesky J, Zaro Weber O, Lehnhardt FG, Hesselmann V, Thiel A, Dohmen C, Jacobs A, Neveling M, Heiss WD. Which time-to-peak threshold best identifies penumbral flow? A comparison of perfusion-weighted magnetic resonance imaging and positron emission tomography in acute ischemic stroke. Stroke. 2004;35(12):2843-7.

37. Zaro-Weber O, Moeller-Hartmann W, Heiss WD, Sobesky J. Maps of time to maximum and time to peak for mismatch definition in clinical stroke studies validated with positron emission tomography. Stroke. 2010;41(12):2817-21.

Chapter 7: Using CEST and Frequency-Labeled Exchange Transfer (FLEX) MRI to Image Blood Oxygenation Dependent Exchangeable Protons in Blood (boldCEST/boldFLEX)

7.1. Abstract

Blood oxygenation is an important pathophysiological parameter that changes in numerous pathological states including ischemia. Previously mentioned in Chapter 1, hemoglobin is the protein responsible for binding oxygen in the lungs where there is a high partial pressure of oxygen (it becomes oxyhemoglobin here) and for transporting oxygen to various parts of the body where oxygen diffuses out of the blood stream (because of a low partial pressure of oxygen in tissue) to engage in metabolic processes. Over the past decades, high resolution NMR has been used to identify a number of exchangeable proton resonances on hemoglobin, some of which have a frequency dependence on oxygenation. Until recently, the only way to measure these exchangeable protons was through spectroscopy, which offered good specificity, but poor sensitivity. Recently, chemical exchange saturation transfer MRI has been proposed as a novel way of increasing sensitivity of MR to exchangeable protons. And even more recently, a more powerful technique, frequency labeled exchange transfer (dubbed FLEX) MRI, not only increases sensitivity to exchangeable protons but can also measure multiple protons simultaneously and quantify exchange rates. In this chapter, we aim to use chemical exchange saturation transfer and frequency-labeled exchange transfer to image these signals.

7.2. Introduction

Oxygenation is an important pathophysiological parameter that changes in many pathological states such as ischemia and chronic obstructive pulmonary disease. Oxygenation can be imaged using positron emission tomography (PET) and magnetic resonance imaging (MRI). PET imaging of oxygenation involves injecting a radiotracer into the body and tracking the tracer as it decays. On the other hand, MRI is capable of imaging oxygenation non-invasively with non-ionizing radiation, which makes it the ideal modality of imaging when tracking the course of a heterogeneous disease such as acute ischemic stroke.

Currently, magnetic resonance techniques that are sensitive to blood oxygenation include blood oxygenation level dependent (BOLD) functional magnetic resonance imaging (BOLD fMRI), T_2 relaxation under spin tagging (TRUST), global oxygen extraction fraction (OEF) measurement at internal jugular vein, Gradient Echo Sampling of Spin Echo (GESSE), and quantitative imaging of extraction of oxygen and tissue consumption (QUIXOTIC) (1-5). BOLD fMRI uses a gradient echo sampling scheme with an echo time of approximately 25 ms at 3 Tesla to be sensitive to decreases in paramagnetic deoxyhemoglobin between a resting state and activated state (where a subject is asked to perform a certain task). Theory has been developed to show that these decreases in paramagnetic deoxyhemoglobin arises from increased cerebral blood flow (CBF), cerebral blood volume (CBV), and oxygen extraction fraction (6). TRUST MRI and the global OEF measurement at the internal jugular vein measures the transverse relaxation time (T_2) of venous blood and uses a calibration curve to map the T_2 to the oxygen extraction fraction (OEF). Issues with these methods are that they are not spatially resolved and only give whole brain oxygenation values. GESSE (otherwise known as quantitative BOLD) uses a gradient echo sampling scheme to sample magnetization around a spin echo and uses susceptibility theory to data to parameters OEF, deoxygenated blood volume, ratio of interstitial fluid and cerebrospinal fluid, R_2 (inverse of transverse relaxation time, T_2) of brain tissue, frequency shift, and brain concentration of deoxyhemoglobin. One issue with the GESSE technique is its high number of fitting variables, which can lead to high degrees of freedom where multiple solutions are possible. And finally, QUIXOTIC uses velocity selective modules (RF pulses and associated gradients) to define a bolus of blood leaving the capillaries and then label this bolus in a similar manner as arterial spin labeling described earlier in Chapter 4. The labeled bolus is then subtracted from a control bolus defined similarly. Because velocity selective modules can be spatially resolved, QUIXOTIC offers spatially resolved information about oxygenation in the brain. However, it suffers from low signal-to-noise ratios.

One method that has not been exploited to image oxygenation in the body is by using exchangeable proton signals in blood, which is responsible for delivering oxygen throughout the body so organs can produce energy and function and transporting waste products to be disposed of. Blood has four main constituents: erythryocytes, plasma, leukocytes, and thrombocytes. Hemoglobin, found in erythrocytes, is the protein in the body responsible for the transport of oxygen. It is a large molecule (65 kiloDalton) composed of two α strands (each with 144 amino acids) and two β strands (each with 146 amino acids) and has many exchangeable protons on it that have been studied in detail by many groups using nuclear magnetic resonance (NMR) (7-14). A good review that summarizes much of the work that has been done on exchangeable protons in oxyhemoglobin, deoxyhemoglobin, and carbonmonoxy-hemoglobin using NMR between the 1970s and 1980s was written by Drs. Chien Ho and Dr. Janice Perussi in 1994 published in Methods in Enzymology (15).

Recently, chemical exchange saturation transfer (CEST) MRI has been introduced to provide amplification of micromolar concentrations of exchangeable protons (16, 17). CEST MRI does this by capitalizing on the chemical exchange trait of certain protons (OH, NH) in molecules. CEST uses a saturation pulse to irradiate protons resonating at a particular frequency, which makes them "invisible" to MR detection. If enough of the irradiated protons exchange with bulk water, then the ultimate effect will be a reduction in the detected water signal. By utilizing the exchange with bulk water, CEST is a powerful technique with the capability of amplifying millimolar concentrations of compounds to be detected with the molar water signal of MRI. CEST has been demonstrated to be sensitive to changes in pH, protein content, and temperature and has been applied in the clinic to study brain tumors and acute stroke (18-21). CEST MRI has also been used to study exchangeable protons in the serine protease system (22). However, CEST MRI has not yet been used to study exchangeable protons on hemoglobin, which has a high intracellular concentration (~5 mM) in erythrocytes and a sufficiently large number of exchangeable protons to make it a suitable target for applying CEST MR imaging to.

Frequency-labeled exchange (FLEX) transfer MRI is a novel imaging technique that has recently been shown to be sensitive to slowly and quickly exchanging protons (23-25). FLEX MRI modulates the water intensity by encoding the chemical shift of exchangeable proton groups through label transfer modules (LTMs), which consist of four parts: 1) a selective 90°_{x} pulse that excites protons over a large range of frequencies and minimizes excitation of water; 2) a delay during which excited protons undergo chemical shift evolution; 3) a selective 90°_{-x}pulse that flips the magnetization back to the longitudinal axis; and 4) another delay for labeled protons to exchange into the bulk water pool. Sensitivity enhancement for low concentrations of exchangeable protons can be achieved by increasing the number of LTMs. Because of the flexibility of the FLEX sequence (can be tuned to detect slowly or quickly exchanging protons, RF pulse placed closer to water can detect exchangeable resonances close to water or further away can detect exchangeable proton resonances over a larger range), we applied FLEX MRI to image blood to look for exchangeable proton resonances in blood.

In this chapter, we aim to use CEST and FLEX MRI to try to detect blood oxygenation dependent exchangeable protons in bovine blood.

7.3. Materials

In this chapter, two types of hemoglobin were investigated: adult human hemoglobin bound to carbon monoxide and bovine hemoglobin. In the next section (Section 7.4.1), we will describe why the use of bovine blood is more advantageous than human blood for this particular project.

7.3.1. Sample: Why Bovine Blood?

Bovine blood was used as the main model system for this study. Bovine blood has similar characteristics as human blood (14). One advantage for using bovine blood over human blood in this is that human blood contains 2,3-diphosphoglycerate (2,3-DPG), which is used for control of oxygenation. However, when human blood is removed from the body, the concentration of 2,3-DPG becomes depleted very quickly, which makes it more difficult to externally control the binding of oxygen.

7.3.2. Carbonmonoxy Hemoglobin

Because of carbon monoxide's high binding constant to hemoglobin (250x that of oxygen), carbonmonoxy hemoglobin is an ideal sample to use when developing and optimizing pulse sequences. Hemoglobin can be purified, dissolved in PBS, ligated to carbon monoxide, and stored away in a sealed glass tube for an extended period of time. Additionally, it serves as a good control for exchangeable protons of oxyhemoglobin and deoxyhemoglobin because of conformational differences between these three structures (15). This results in different chemical shifts for each of exchangeable protons on each protein.

Human adult blood samples were obtained from a local blood bank. Human adult hemoglobin (Hb A) was isolated and purified by established methods in Dr. Chien Ho's laboratory (15). All Hb A samples used were in the CO-ligated form in 0.1 M sodium phosphate buffer at pH 7.4, and the Hb A concentrations (in terms of tetramer) used in this study were about 2.4 mM and 4.9 mM.

7.3.3. Whole Blood

Fresh bovine blood was provided by a local slaughterhouse. The blood was collected into a container filled with a distilled de-ionized water solution of the anticoagulant sodium citrate to give a final concentration of 25 mM. Blood was filtered to remove clots and impurities accumulated during the procedure of blood collection.

Whole blood samples of 44% hematocrit were prepared by spinning down whole blood using a centrifuge (Beckman Coulter Avanti Centrifuge J-25I, Rotor

Number: JA-10) at 10,000 G for 15 minutes. Plasma and packed erythrocytes were combined and mixed to create a sample with 44% hematocrit. Oxygenation of the 44% hematocrit sample was manipulated by using a gas tank (Airgas) filled with 94% nitrogen, 5% oxygen, and 1% carbon dioxide. pH of the sample was manipulated by using a gas tank (Airgas) filled with 100% carbon dioxide. Hematocrit, pH and methemoglobin (MetHb) values, together with the blood oximetry parameters sO_2, pO_2 and pCO_2 were measured with a blood gas analyzer (Radiometer ABL 700 series, Radiometer, Copenhagen, Denmark). All blood samples were stored at 4°C and used within a week after preparation. During that time, none of the samples exhibited any formation of blood clots or increase in MetHb levels.

7.3.4. Washed Erythrocytes

Because whole blood is largely constituted of plasma and erythrocytes, it is possible that detected signals using whole blood could come from proteins in plasma. Therefore, it is important to verify that detected exchangeable proton signals are indeed coming from hemoglobin. One way of doing this is to wash whole blood using phosphate buffer solution. The resulting sample would have no plasma with erythrocytes suspended in buffer solution.

Washed erythrocytes were prepared by centrifuging (Beckman Coulter Avanti Centrifuge J-25I, Rotor Number: JA-10) whole blood at 10,000 G for 15 minutes, extracting plasma, and replacing immediately with phosphate buffer solution (PBS). The solution was hand mixed for 10 minutes to ensure adequate mixing between packed erythrocytes and PBS and centrifuged again at 10,000 G for 15 minutes. PBS was extracted and replaced immediately with new PBS. This solution was mixed for 30 minutes to ensure adequate mixing between packed erythrocytes and PBS. This mixture was centrifuged at 10,000 G for 15 minutes, and PBS was extracted and replaced with new PBS to give a solution of 44% hematocrit washed erythrocytes. The first time we performed the procedure, we put a smear of cells under a microscope (Olympus, IX71) at 40x magnification to verify that erythrocytes maintained their shape after washing (figure 8.1).

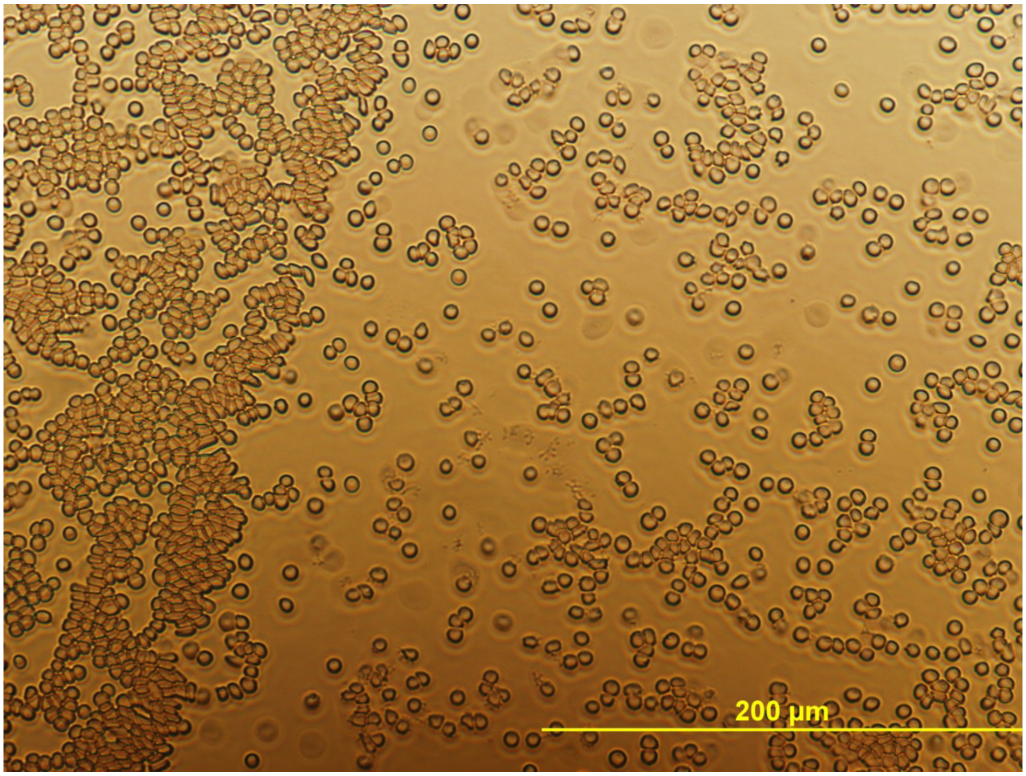

Figure 7.1. Washed Cells Under a Microscope at 40x Magnification.

It can be seen that the washing process did not perturb the isotonicity of erythrocytes. This is important as we want to study erythrocytes in their normal environment, and the washing process is just to remove plasma from the sample.

7.3.5. Experimental Set-up

Blood was circulated in a gas exchange perfusion system at a controlled physiological temperature (37 °C) within the 700 MHz spectrometer. Details of the perfusion system setup were described previously (15). Blood was sampled right before and after the MR measurements and oxygenation determined using a blood gas analyzer (Radiometer, ABL700) to ensure less than 2% difference of oxygenation. Additionally, blood pO_2 was monitored during the MR measurement with a needle-encased sensor (Oxford Optronix, Oxford, UK) placed close to the spectrometer.

7.3.6. Flow Analysis

There are two reasons why we flowed blood through a perfusion system for these measurements: (1) CEST experiments require sweeping over a wide range of frequencies and can take up to an hour and sometimes more (more details on this later). Erythrocyte sedimentation rates (as a measure of how quickly erythrocytes settle in a test tube in 1 hour) of normal blood are in the range of 10-30 mm/hr (26)**.** Without flow, erythrocytes would quickly settle to the bottom of a sample tube and the distribution of erythrocytes and plasma would be uneven (erythrocytes as the bottom and plasma on top). (2) Blood is constantly flowing through the body. Any technique developed for the measurement of oxygenation should take this into account. However, both CEST and FLEX MRI have several seconds of "labeling" where radiofrequency pulses are used to "label" exchangeable spins in the blood. If flow is turned on during labeling periods, we need to be sure that the sample that is being "labeled" does not flow out of the detection coil before it is being imaged.

Therefore, we performed a quick analysis to determine the optimal flow speeds for this experiment.

To experimentally determine the flow speed of the motor (which has 3 settings: 1-3), we pumped phosphate buffer throughout the tubing, dripped it into a 14 mL Falcon tube, and timed how long it took (at three different flow settings) for the 14 mL Falcon tube to be immersed with buffer. Table 7.1 displays the results of the flow speed tests.

Table 7.1. Data from Flow Speed Tests

Flow Setting	Try 1 (s)	Try 2 (s)	Try 3 (s)	Summary (s)	Calculated Flow Speed
1	82	86	85	84±2	0.17 mL/s
2	45	45	45	45±0	0.31 mL/s
3	28	30	29	29±1	0.48 mL/s

In order to calculate how long we should label, we need to calculate the volume of blood that is labeled with the RF coil. To derive this number, we can use the volume of a cylinder equation:

$$V = \pi * radius^2 * Length = 3.14 * (0.5\ cm)^2 * 3\ cm = 2.36\ cm^3 \quad \text{(Equation 7.1)}$$

Then the percentage of label flown out can be calculated by multiplying the flow speed by the flow rate divided by the volume of the coil. The data is presented in table 7.2.

Table 7.2. Percentage of Label Flown at for Different Flow Speeds

Flow Setting and (Speed)	**1 s label**	**2 s label**	**3 s label**	**4 s label**	**5 s label**
1 (0.17 mL/s)	7.1%	14%	21%	28%	35%
2 (0.31 mL/s)	13%	26 %	40%	53%	66%
3 (0.48 mL/s)	20%	41%	61%	82%	102%

It can be seen that with a five second label duration at a flow speed of 3 (0.48 mL/s), all of the label will have flowed out. Therefore, a five second CEST labeling duration at a flow speed of 3 would only waste time. Thus, we decided to try CEST labeling durations of one, two, and three seconds. More details about this will be described later.

7.4. Methods – Part 1

All MR experiments were carried out on a 700 MHz (16.4 T) Bruker Avance Spectrometer (Billerica, MA) equipped with a 1000 W amplifier and a 30 mm imaging transceiver coil connected through a 300 W combiner for dual channel quadrature detection.

7.4.1. Optimizing Spin Echo

When choosing an acquisition method for a sequence, it is important to consider speed (gradient echo is a faster sequence that will allow shorter echo times to be used, resulting in higher signal to noise if samples have a short T_2) and signal-to-noise (spin echo has a higher signal to noise because of ability to refocus inhomogeneities caused by paramagnetic species, such as the deoxyhemoglobin we plan on imaging). In CEST imaging, exchangeable protons yield signals that depend on a number of different factors such as concentration, exchange rate, saturation pulse B_1, and saturation pulse duration. However, because these signals are typically on the order of a few percent, imaging sequences with high signal-to-noise are especially important and we therefore chose to use a spin echo acquisition scheme.

When imaging, it is important to excite a homogeneous slab of signal to image. To do this, we can use slice selection gradients with the 90° and 180° pulse and use a read-out gradient to create a 1-dimensional profile of the sample (shown in figure 7.2).

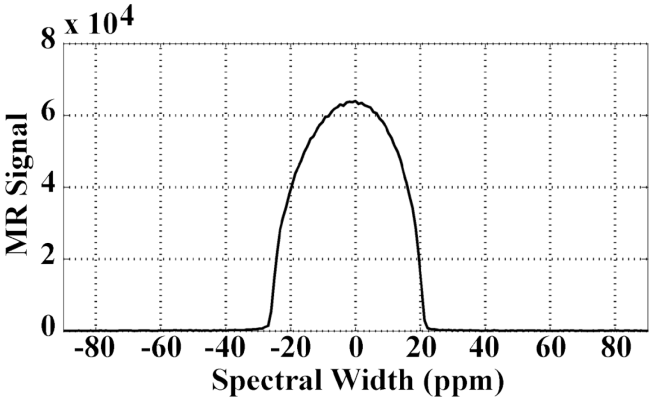

Figure 7.2. 1D Profile Read-out of Spin Echo. Slice thickness = 3 cm.

7.4.2. FLEX Imaging Parameters

In our initial proof-of-principle scan, we wanted to sweep a wide range of frequencies and detect all possible exchangeable protons in the whole blood. To do this, we wanted to place the FLEX pulse as far away from the water frequency as possible. The calculation of the FLEX pulse offset is derived from the off-resonance field generated by hard pulses ($\Delta\omega_{eff}$):

$$\Delta\omega_{eff} = \sqrt{\omega_1^2 + \Delta\omega_{s01}^2} \qquad \text{(Equation 7.2)}$$

Where is the ω_1 is the B_1 field strength, and $\Delta\omega_{o1}$ is the offset frequency. An offset $\Delta\omega_{s01}$ can be chosen such that the product $\omega_{eff} \cdot \tau_{90}$ is 2π radians on water and π/2 for exchangeable protons to minimize water excitation thereby functioning as a water suppression pulse. This relationship is then governed by equation 7.3.

$$\Delta\omega_{so1} = \omega_1 \cdot \sqrt{15} \qquad \text{(Equation 7.3)}$$

Using the highest power we could (limited only by hardware), we determined that we could use a 30 μs pulse placed at 32266.67 Hz (or +46.10 ppm at 700 MHz). However, this offset is actually a little bit unfortunate because we were originally also interested in imaging the histidine proton (known as the distal histidine) next to the iron on deoxyhemoglobin. Previous research has shown that the chemical shift of the distal histidines of the alpha and beta globin chains in this deoxygenated molecule are at 58.5 ppm and 71.0 ppm, respectively (27).

Other FLEX parameters that need to be defined include: 1) the evolution time and number of tevolution times needed to encode the chemical shift evolution of exchangeable proton peaks; 2) the exchange time, which is the delay after labeling used for labeled peaks to exchange to bulk water (this exchange time parameter can also be tuned for the FLEX sequence to be sensitized to slowly or quickly exchanging protons); and 3) the number of LTMs, which is the number of repetitions of the label transfer module. The FLEX sequence is displayed in figure 7.3 for the user's reference.

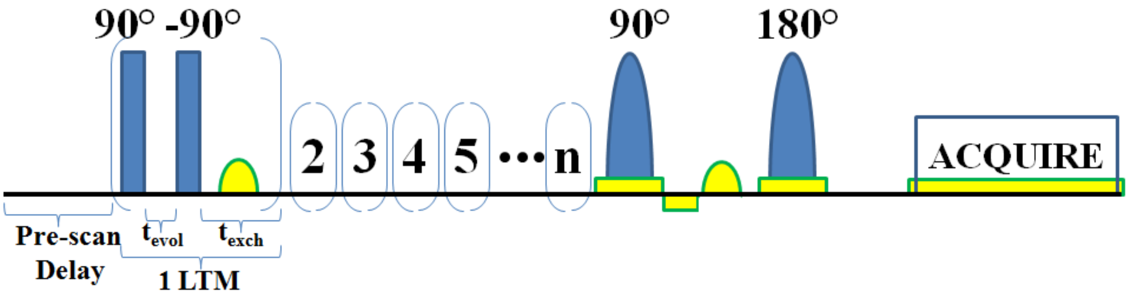

Figure 7.3. FLEX Sequence. RF pulses are represented using blue blocks: The FLEX 90° and -90° pulses were block pulses; and the 90° and 180° pulses for spin echo were Gaussian pulses. Gradients are represented in yellow. A gradient was used during the t_{exch} period to dephase any residual transverse magnetization. The next two gradients are for slice selection for the 90° pulse. This is followed by a dephase gradient, slice selection gradient for the 180° pulse, and readout gradient.

In our initial efforts, we chose to vary the evolution times between 0 and 1 ms in increments of 5 μs (also known as the dwell time). The duration of the dwell time is important in fulfilling the Nyquist sampling theorem, which defines the minimum sampling rate to be twice the frequency of the signal of interest. Using a 5 μs dwell time applied at a reference frequency of 32,266.67 Hz, we would be able to adequately measure signals oscillating at 100,000 Hz away from our reference frequency. We decided to initially go with 400 LTMs with a single LTM duration of 5 ms (yielding a t_{exch} of 4.94 ms), which gives us a total FLEX preparation time of two seconds (400*5 ms = 2000 ms). Using a short exchange time sensitizes the FLEX sequence to fast exchanging protons because after the protons are frequency labeled, they are only given a short period of time to exchange with bulk water. Therefore, the label on fast exchanging protons is transferred effectively whereas the label on the more slowly exchanging protons does not have enough time to exchange yet. The reason why our initial efforts focused on fast exchanging protons is because the protons that we were interested in detecting are histidine protons, and past research has shown that histidine protons can exchange between 500-10,000 times per second (28).

Multi-pulse sequences such as the FLEX may have contamination from many signal components, for instance stimulated echoes. An important way to improve the signal quality of FLEX experiments is through phase cycling, which can be used to eliminate unwanted signals from NMR experiments on the basis of their phase. In order to get phase-sensitive spectra, we acquired a cosine and sine component for the FLEX signal. Phase cycling for the cosine component employed 0°, 90°, 180°, 360° with the flip-back pulse set to 180°, 270°, 0°, 90°. Phase cycling for the sine component was implemented with 0°, 90°, 180°, 270° with the flip-back pulse set to 90°, 180°, 270°, 0°. To make sure phase cycling does not adversely affect our spectra, we ran FLEX experiments with the following parameters on the 4.9 mM HbCO sample:

Experiment 1) t_{evol} = 0 to 1 ms (increment 5 μs), t_{exch} = 10 ms, LTMs = 400, without phase cycling.

Experiment 2) t_{evol} = 0 to 1 ms (increment 5 μs), t_{exch} = 10 ms, LTMs = 400, with phase cycling.

Experiment 3) t_{evol} = 0 to 1 ms (increment 5 μs), t_{exch} = 20 ms, LTMs = 400, without phase cycling.

Experiment 4) t_{evol} = 0 to 1 ms (increment 5 μs), t_{exch} = 20 ms, LTMs = 400, with phase cycling.

Results of these four experiments are presented below in figure 7.4.

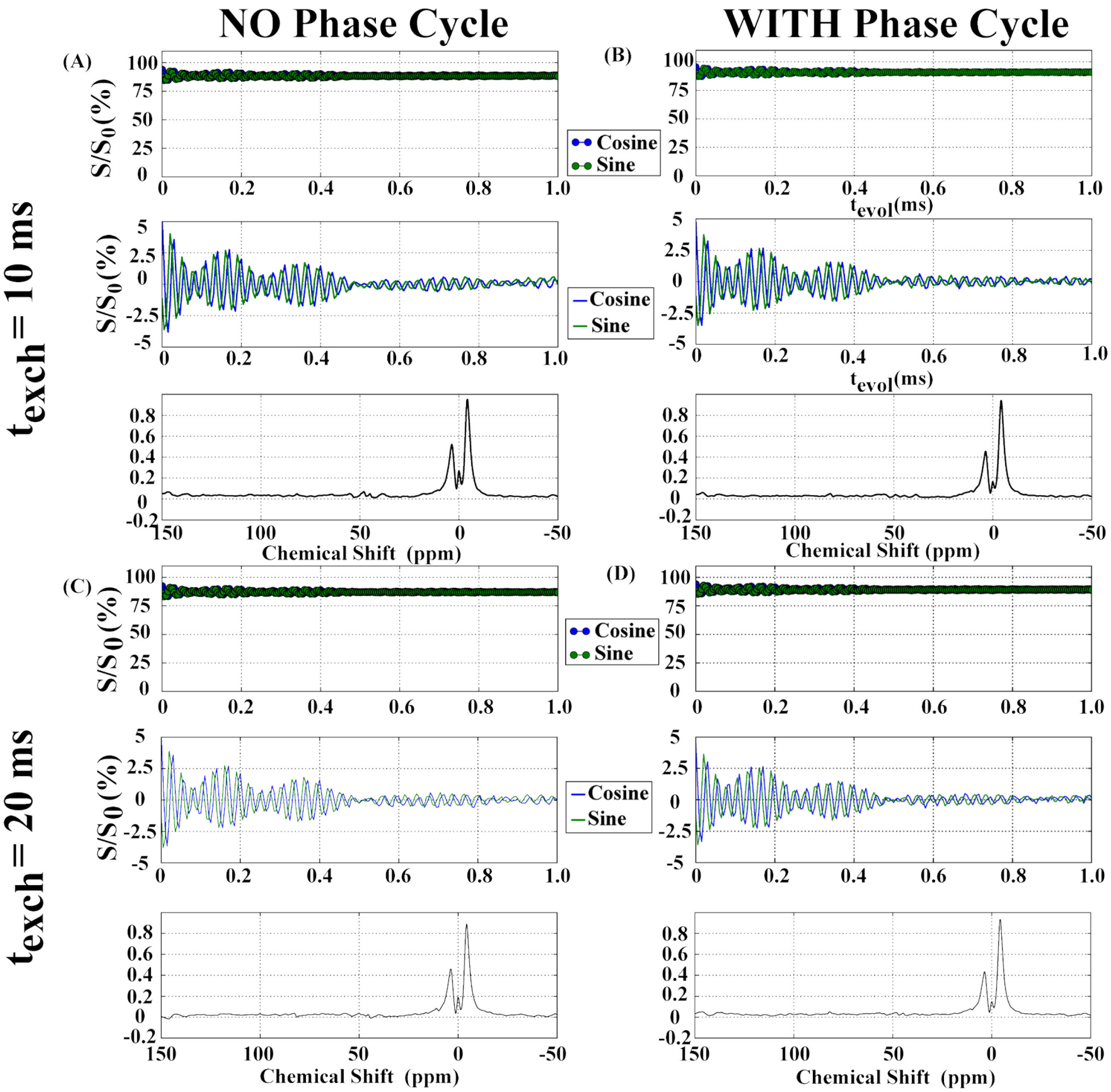

Figure 7.4. (A) FLEX, t_{exch} = 10 ms, without phase cycle (B) FLEX, t_{exch} = 10 ms, with phase cycle (C) FLEX, t_{exch} = 20 ms, with phase cycle (D) FLEX, t_{exch} = 20 ms, without phase cycle

Based on the data presented in figure 7.4, phase cycling appears to help clean-up unwanted signals in our FLEX acquisition and does not appear to introduce any unwanted artifacts.

Additionally, it is important to check FLEX excitation profiles to verify that 1) water excitation is minimized; and 2) the range of exchangeable protons that we are interested is properly excited. FLEX excitation profiles were acquired experimentally on a sample of 44% hematocrit 100% oxygenated whole blood by applying a 90° pulse across a wide range of offset frequencies. Excitation profiles for FLEX pulse durations of 30 μs and 40 μs are presented in figure 7.5.

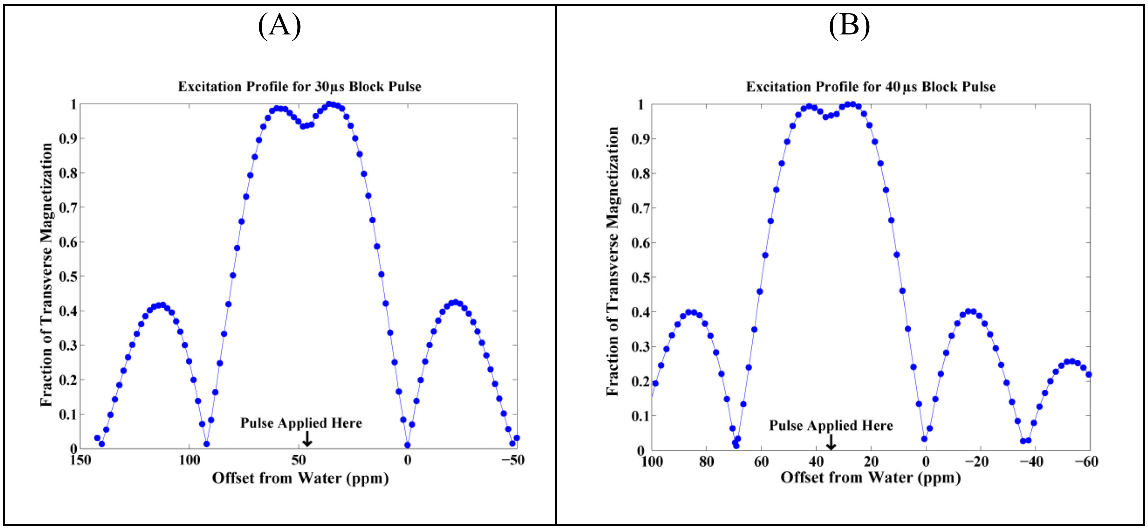

Figure 7.5. FLEX Excitation Profiles for (A) 30 μs block pulse applied at +46.10 ppm (B) 40 μs block pulse applied at +34.57 ppm

It appears that there may be some overtipping of the FLEX excitation pulses near the frequency offset where the pulse is applied, but the excitation profiles follow what we would expect for these pulses.

7.4.3. CEST Imaging Parameters

The CEST sequence is composed of three main parts: 1) Pre-scan delay, to allow for enough time for the magnetization to recover after saturation; 2) Saturation Pulse, to saturate over a range of frequencies so saturated exchangeable protons can exchange into bulk water and replaced by non-saturated protons; and 3) Acquisition. The optimized CEST sequence is displayed in figure 7.6.

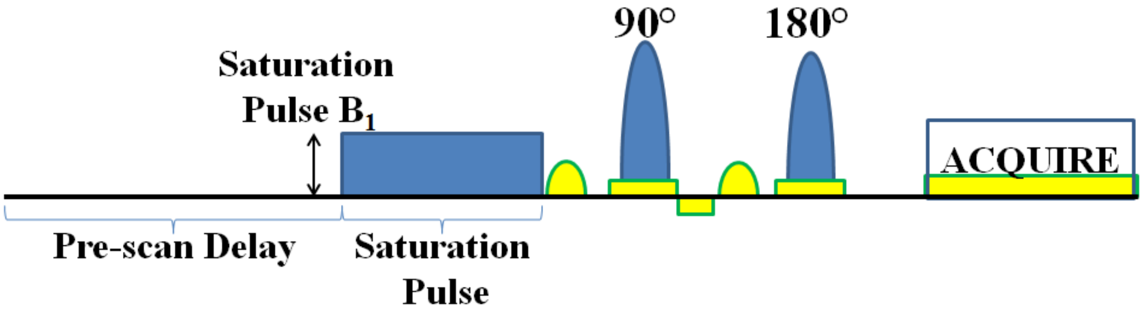

Figure 7.6. CEST Sequence. RF pulses are represented in blue: the saturation pulse is represented by a blue box because a block pulse was used for it; and Gaussian pulses were used for spin echo 90° and 180°. Gradients are represented in yellow. The gradient after the CEST pulse is to dephase any transverse magnetization left after the CEST pulse. The next two gradients are for slice selection for the 90° pulse. This is followed by a dephase gradient, slice selection gradient for the 180° pulse, and readout gradient.

An unsaturated CEST scan (S_0) was collected after all of the saturated volumes were collected and was composed of exactly the same sequence but with the B_1 of the saturation pulse set to zero.

7.4.4. Optimizing CEST Saturation Pulse Duration

One important parameter to optimize in CEST experiments is the saturation pulse duration. A quick glance at how the saturation efficiency of the CEST pulse is determined (equations 7.3-7.5) would tell us that a saturation pulse of infinite duration would yield the highest CEST effect (29):

$$\alpha = \frac{\omega_1^2}{\omega_1^2 + pq} \qquad \text{(Equation 7.3)}$$

$$p = r_{2c} - \frac{C_{ac}C_{ca}}{r_{2a}} \qquad \text{(Equation 7.4)}$$

$$q = r_{1c} - \frac{C_{ac}C_{ca}}{r_{1a}} \qquad \text{(Equation 8.5)}$$

Where r_{1c} is the sum of R_{1c}, the longitudinal relaxivity of the amide proton and C_{ac}, the exchange rate between bulk water and the amide proton and r_{2c} is the sum of R_{2c}, the transverse relaxivity (inverse of T_{2c}) of the amide proton and C_{ac}, the exchange rate between bulk water and the amide proton. Additionally, it can be simulated that exchangeable proton pools with a short T_2 do not undergo complete saturation with short saturation pulses.

At 37°C bovine blood is only fresh for a certain period of time (~12 hours), so we want a short enough saturation pulse to minimize scan time yet a long enough saturation pulse to increase the CEST effect (PTR) and minimize artifacts from the possibly short T_2 of exchangeable protons on hemoglobin. At low oxygenation (60%) and high field (700 MHz), T_2 of deoxygenated blood is very short (~13 ms for 44% hematocrit and τ_{cpmg} = 0.5 ms (unpublished data)). We put in a sample of 44% hematocrit whole blood at 65% oxygenation and ran three CEST experiments with B_1 = 14.1 µT but with different saturation times (1 seconds, 2 seconds, 3 seconds) with the pre-scan delay set to 8 seconds over the frequency range -5 ppm to 5 ppm in increments of 0.2 ppm. Here, flow was set to 0.48 mL/second.

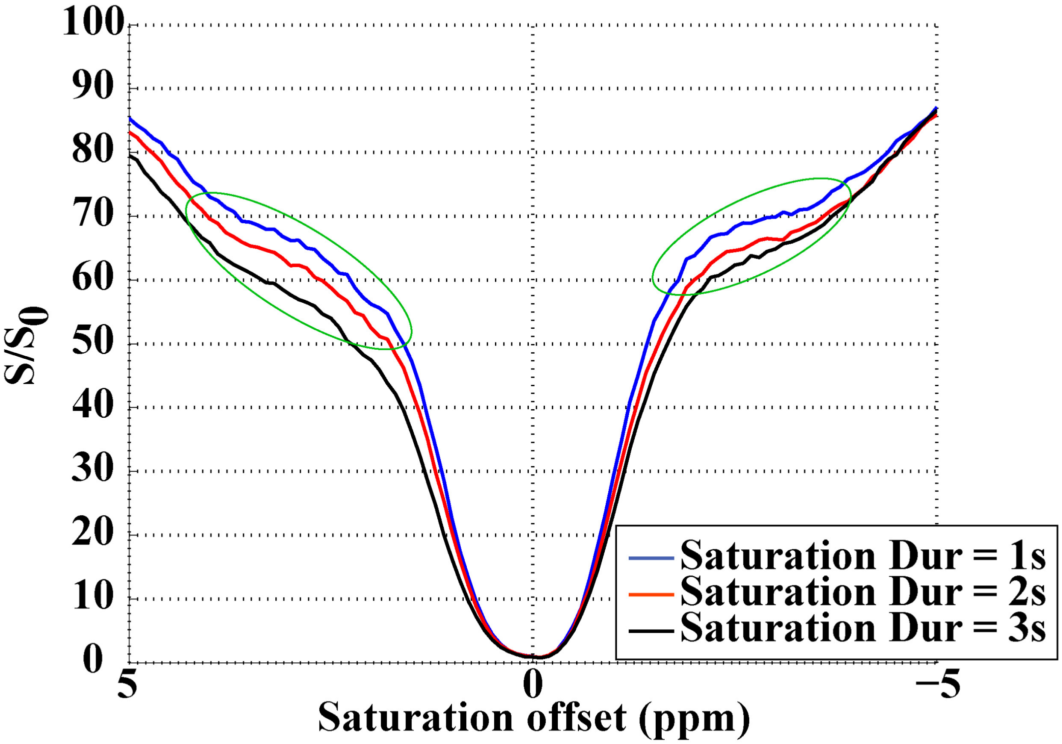

Figure 7.7. Data Over Multiple Saturation Pulse Durations.

"Wiggles" (green boxes) in the CEST spectra show that a saturation pulse duration of less than three seconds may not be long enough for the exchangeable protons in blood to be in steady state saturation. Based on this data, we chose a saturation pulse duration of three seconds for our CEST experiments. Now that we have determined the saturation pulse duration, we can estimate a pre-scan delay needed to allow magnetization to return back to normal. It is well-known that five times the longitudinal magnetization relaxation time is enough time for magnetization to recover. We ran a quick inversion recovery experiment and quantified the T_1 of 44% hematocrit, 100% oxygenated blood to be 2,462 ms. Five times of that would be 12.31 seconds. Interestingly, because the blood is constantly flowing, another way to calculate a pre-scan delay would be to figure out how long it takes for the current bolus to flow out. To do this, we could divide the volume of blood that the coil excites (2.356 mL) by the flow speed (0.49 mL/second) and arrive at 4.8 seconds. We could even add one second for a margin of error. After six seconds, the bolus of blood that was previously saturated has already flowed out. Therefore, we selected a pre-scan delay of six seconds.

Another parameter that needs to be chosen for CEST experiments is the saturation pulse B_1. The simplified solution for saturation efficiency (α) under slow exchange conditions on the NMR time scale tells us that the B_1 we choose for our experiments will depend on the exchange rate of the proton we are interested in.

$$\alpha = \frac{(\gamma B_1)^2}{(\gamma B_1)^2 + k_{sw}^2} \qquad \text{(Equation 7.6)}$$

Where γ is the gyromagnetic ratio of hydrogen ($267.53\text{x}10^6 \frac{rad}{s \cdot T}$), B_1 is the power of the saturation pulse, and k_{sw} is the exchange rate of the exchangeable proton. Because the histidine protons that we were trying to detect has a fast exchange rate, we chose to use a 14.1 μT pulse.

And finally, the last CEST parameter that needs to be set is the frequency range over which the saturation pulse will be swept. Previously, we mentioned in the FLEX section that it may also be interesting to detect the distal histidine of deoxyhemoglobin. However, in order to detect that far away from water, it would be necessary to sweep from +80 ppm to -10 ppm in order to capture the water offset to determine whether or not there was a B_0 shift over the period of our experiment. However, in order to have enough spectral resolution to differentiate narrow peaks, we would have to acquire a point every 0.2 ppm, which would make the total scan time 67 minutes and 48 seconds long for a single oxygenation and a single B_1. To be practical, we decided we would use the FLEX scan to "screen" the blood to see if there were any exchangeable proton resonances on deoxyhemoglobin. If so, then we would run a CEST scan with frequency offsets from +80 ppm to -10 ppm in increments of 0.2 ppm. Otherwise, we would restrict ourselves between +15 ppm to -15 ppm in increments of 0.2 ppm.

7.4.5. 1-H WATERGATE Imaging Parameters

Traditionally, exchangeable protons have been detected using spectroscopic sequences with water suppression that does not saturate the water signal until just before acquisition of the spectra, such as the well-known WATERGATE (3-9-19) sequence (30). Because spectroscopy has been previously used to study exchangeable protons on hemoglobin, we believed that it would be an independent check for any exchangeable protons detected with CEST or FLEX. However, after optimizing the 1H-WATERGATE sequence, we checked the excitation profile and realized we could only acquire between -10 ppm and 11 ppm if we wanted at least 1% excitation efficiency (figure 7.8).

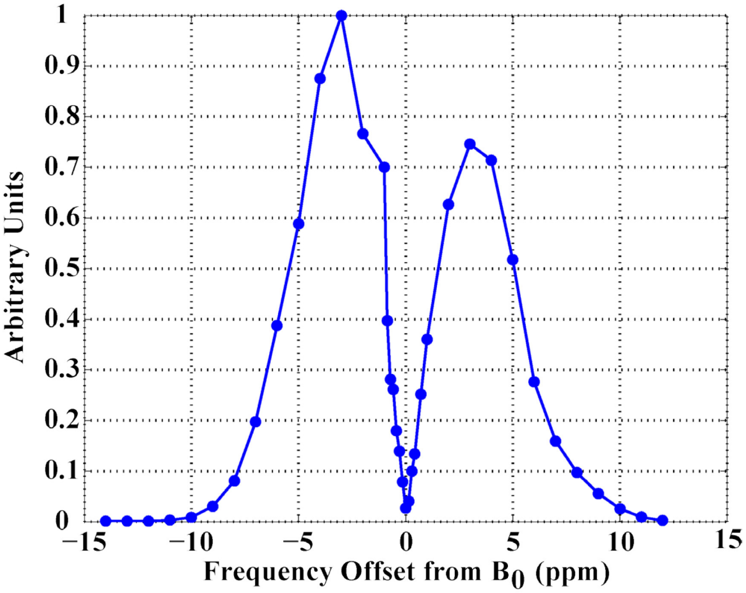

Figure 7.8. Excitation Profile of 1H-WATERGATE sequence on 700 MHz scanner.

We realized that the reason why this happened was because of hardware limitations. Using the highest power we could achieve on the 30 mm imaging probe, the shortest duration of the longest rectangular pulse in the 3-9-19 pulse train was 59.50 µs. In the frequency domain, this would be equal to 16,807 Hz, which at 700 MHz, corresponds to 24 ppm. This means that the excitation profile of a WATERGATE sequence will be a convolution of the WATERGATE excitation profile with infinitely short pulses with the frequency response of a 59.5 µs pulse (figure 7.9). Because of hardware limitations, we decided not to continue with this sequence.

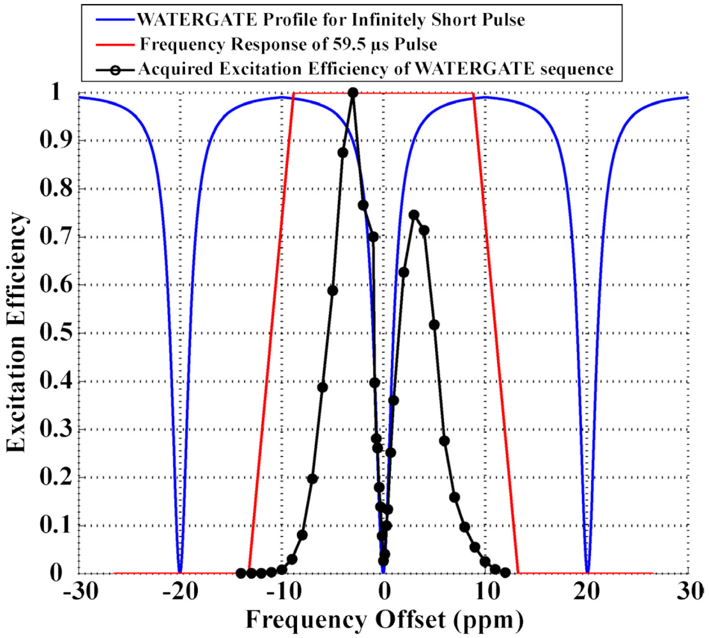

Figure 7.9. Explanation of why WATERGATE at 700 MHz using our hardware does not work.

7.5. Data Processing

All data was processed using in-house written MATLAB® R2008a (The Mathworks, Natick, MA) and in-house written Python routines.

7.5.1. FLEX Processing

The FLEX FID was generated by integrating the spin echo projection of the sample at each evolution time for both cosine and sine components. Next, the FID was normalized by the integral of S_0 and multiplied by 100 to yield a percentage. Then, we fit the S/S_0 cosine and sine FIDs to the five component exponential FLEX equation (equation 7.7).

$$FLEX_{FID} = \sum_s PTR_s \cdot e^{-(k_{sw}+R_2^*)\cdot t_{evol}} \cdot \cos(\Delta\omega_{so1} \cdot t_{evol} + \varphi) \qquad \text{(Equation 7.7)}$$

Where PTR_s is the amplitude of the exchangeable proton resonance, R_2^* is inverse of the time constant of the loss of phase coherence of the exchangeable protons, $\Delta\omega_{s01}$ is the frequency difference between the resonance offset of the exchangeable proton and the frequency offset of the FLEX excitation pulse. A five compartment model was chosen because the first component was fitted for low frequency drift, the second component was fitted for the amide proton component, the third component was fitted for NOEs, the fourth component was fitted for bulk water, and the last component was allowed to vary to fit for the oxygenation dependent peak. Fitting bounds for the frequency of the last component were used to prevent other peaks from being fitted. After determining the baseline and low frequency drift using the fitted values, we subtracted these from the data to derive the baseline-corrected FLEX FID. Then, we combined the real (cosine FLEX) and imaginary (sine FLEX) components using the Hilbert transform theory to arrive at the combined FID. To prevent truncation artifacts that frequently arise from not sampling the FID until the signal has completely decayed, we applied a cosine filter over the time domain. Finally, we took the Fourier transform of the combined FID to get the phase-sensitive frequency spectrum. To calculate the frequency offsets for the spectrum, we calculated the sweep width to be the inverse of the dwell time, defined as the increment in FLEX evolution times. Zeroth order and first order phase corrections were performed the same way as Friedman et al (23).

Additional data processing to study what we believed to be an oxygenation dependent peak in the FLEX spectrum included time domain fitting using the exponential FLEX equation to fit out the amide proton, water, and Nuclear Overhauser Effects from the FID. After subtracting out the amide proton, bulk water, and NOEs from the fid, we were left with a spectrum with only a peak at 10 ppm.

7.5.2. CEST Processing

At each irradiation offset frequency, the raw CEST data were processed by applying a Fourier Transform to the spin echo to get the 1D projection of the sample. Then, the spin echo was integrated over the frequency spectrum to get a single intensity value. This value was then normalized using the first unsaturated (S_0) scan acquired and multiplied by 100 to yield a percentage value.

Because of scanner drift, S_0 scans were interspersed throughout the data acquisition after every ten frequencies. CEST baseline correction was performed on the z-spectra similarly to the method described in Chapter 6.

Furthermore, asymmetry curves were calculated based on the following equation:

$$MTR_{asymmetry}(\Delta\omega) = \frac{S_{sat}(-\Delta\omega) - S_{sat}(\Delta\omega)}{S_0} \qquad \text{(Equation 7.6)}$$

Where $S_{sat}(-\Delta\omega)$ is the saturated volume acquired Δω ppm upfield of water, $S_{sat}(\Delta\omega)$ is the saturated volume acquired Δω ppm downfield of water, and S_0 is the unsaturated image.

7.6. Results & Discussion – Part 1

7.6.1. Carbonmonoxy Hemoglobin

The FLEX results for carbonmonoxy hemoglobin are displayed in figure 7.10. The results are in line with what is expected for the two concentrations of HbCO. A higher concentration of HbCO would yield peaks with higher protein effects (amide protons and NOEs). The difference in the water peak arises from the difference between the T_1 of the two samples. It is also clear that there are no other peaks from exchangeable protons in this spectrum, which is also in line with what is understood about carbon monoxy hemoglobin.

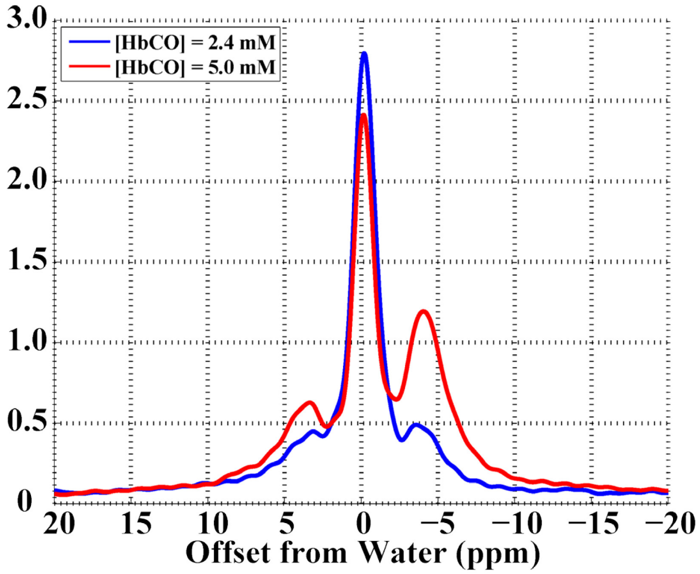

Figure 7.10. FLEX results for 2.4 mM and 4.9 mM HbCO.

The FLEX spectrum for carbonmonoxy hemoglobin at two different concentrations both shows three main peaks. The peak downfield of water (to the left of water) around +3.5 ppm are amide protons on the carbonmonoxy hemoglobin protein. The peak at 0 ppm is the bulk water signal. Notice between the two different concentrations of HbCO that the bulk water peak is slightly different. This is because the bulk water peak is proportional to T_1 and T_2, which is probably different between these two concentrations. And finally, the peak on the right around -4 ppm is due to NOEs.

The CEST results for 4.9 mM HbCO are shown in figure 7.11 for a saturation pulse duration of five seconds with B_1 = 1.4 uT.

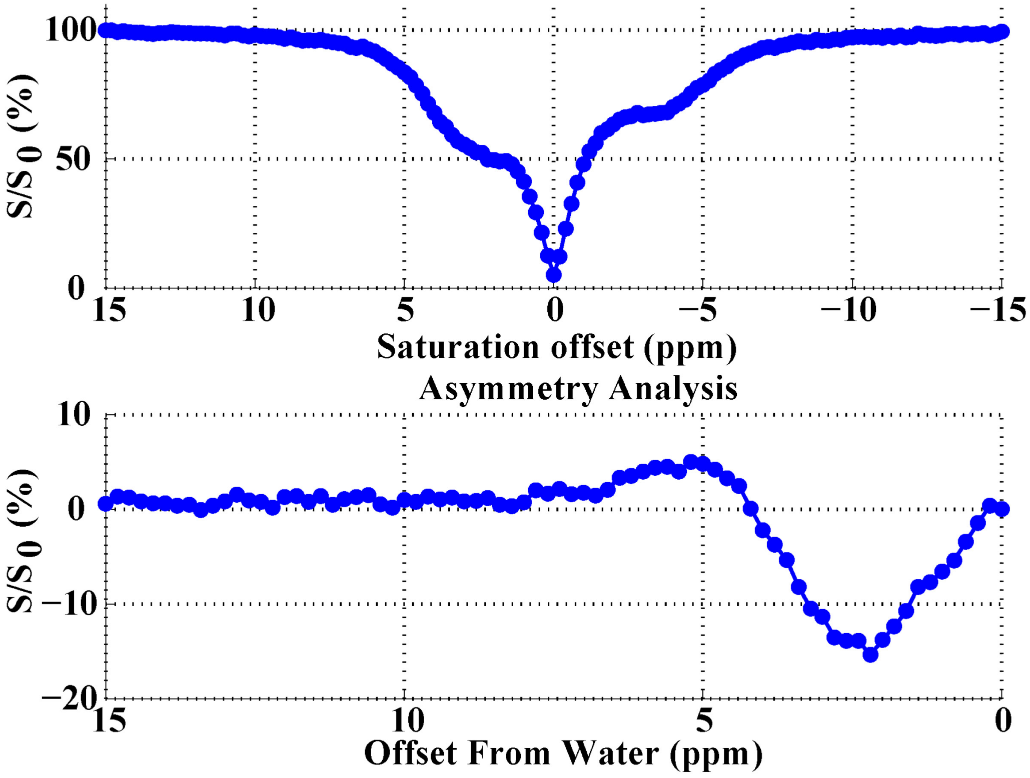

Figure 7.11. CEST (top) and $MTR_{asymmetry}$ (bottom) spectra for 4.9 mM concentration of HbCO.

The CEST spectra of the 4.9 mM HbCO is in line with the results of the FLEX data. There is a clear peak from amide protons around 3.5 ppm, and a peak between -5 and -2 ppm from NOEs. There do not appear to be any other exchangeable protons detectable with CEST or FLEX at this concentration of HbCO.

7.6.2. 30 μs FLEX of 44% Hematocrit Whole Blood

The initial results of the multi-oxygenation scan were quite interesting and have been summarized in figure 8.12A-D.

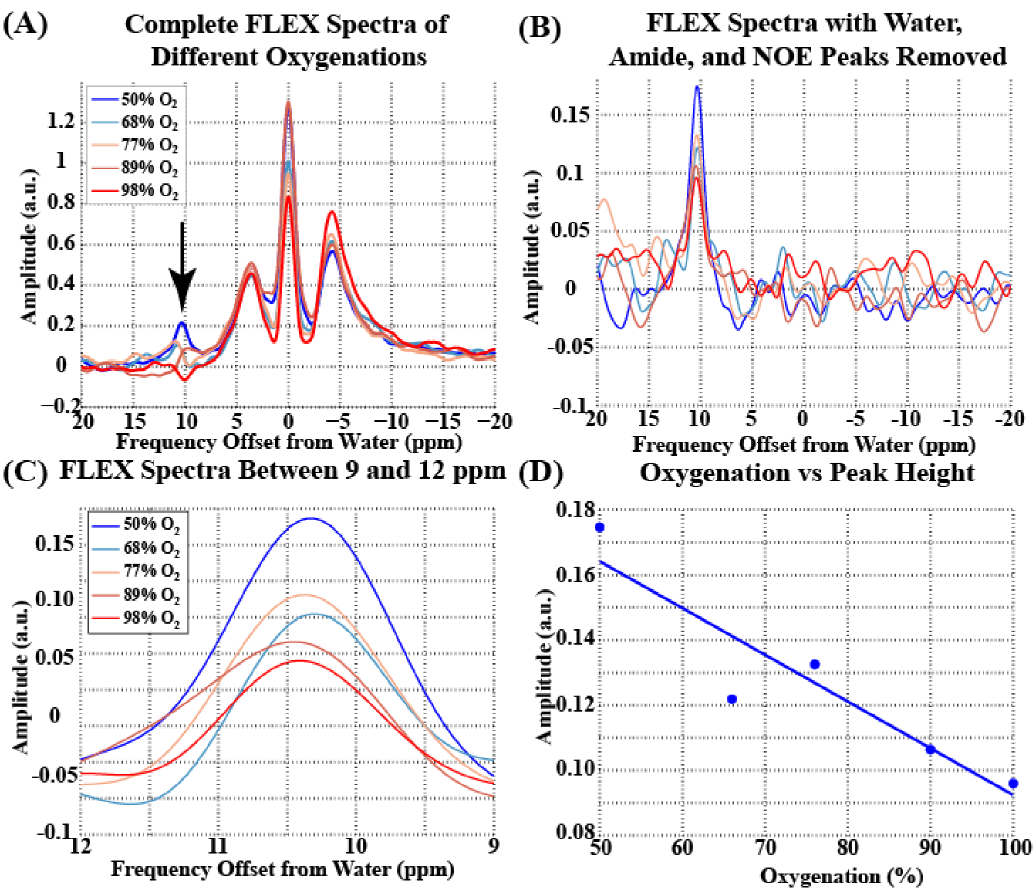

Figure 7.12. FLEX Results of Multi-oxygenation Scan (A) FLEX results for 5 different oxygenations. (B) Amide Proton, Bulk Water, and NOE-filtered FLEX spectrum

(C) Zoomed-in 10 ppm peaks for 5 different oxygenations (D) Linear correlation of Oxygenation vs Peak Amplitude, $r^2 = 0.86$

FLEX scans run on a sample of 44% hematocrit whole blood over a range of oxygenations show a possible oxygenation dependent peak around 10 ppm (figure 7.12A). To further study the peak, bulk water, amide protons, and NOEs were filtered out using time domain analysis only to leave the peak around 10 ppm (figure 7.12B&figure 7.12C). After independently phase correcting each peak, there appears to be an oxygenation dependent at 10 ppm. When plotting the peak amplitude against oxygenation (figure 7.12D), there is a strong correlation ($r^2 = 0.86$) with the equation relating the two being:

Peak Amplitude = $-0.001*O_2+0.236$ (Equation 7.7)

I thought that I imaged the so-called "T-marker" that uniquely identifies deoxyhemoglobin, resonating at 9.4 ppm with respect to water (8). It was previously identified by Fung et al (8) to be a hydrogen bond between α42 tyrosine and β99 aspartic acid at the $\alpha_1\beta_2$ interface and follows a similar behavior as what we have uncovered. It can be argued that the exchangeable proton that our data points to is sitting at 10.3 ppm from water so this is not necessarily the T-marker. However, it is widely known that chemical shift is very sensitive to environment and protein conformation. In Fung et al's studies, they isolated human hemoglobin A and dissolved it in a phosphate buffer of pH 7.4 whereas we were imaging bovine whole blood, which means hemoglobin is inside of red blood cells, at pH 7.2.

7.6.3. 30 µs FLEX of Washed Erythrocytes

After seeing the previous results, we were worried that the peak may have been from proteins (albumin) in plasma. To test our hypothesis that the peak is due to an oxygenation dependent exchangeable proton on hemoglobin, we washed the erythrocytes to remove plasma and ran the FLEX scan on a sample of 100% oxygenated washed erythrocytes and a sample of 65% oxygenated washed erythrocytes. Data is presented in figure 7.13.

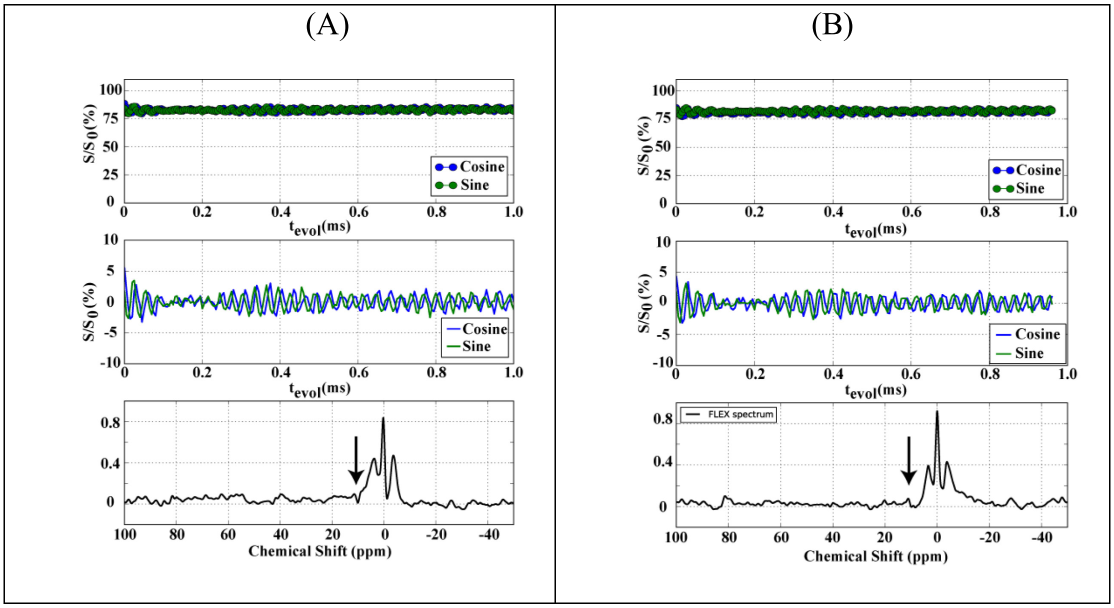

Figure 7.13. FLEX data and spectra of 44% hematocrit washed erythrocytes with (A) 100% oxygenation; and (B) 65% oxygenation.

Interestingly, we still saw a peak in the sample with lower oxygenation, and the peak appeared inverted in the higher oxygenated sample. Thus, FLEX spectra acquired on washed cells confirm the existence of an oxygenation dependent peak around 10 ppm and show that this peak is not due to proteins in plasma. In figure 7.13A, the peak around 10 ppm appeared to be inverted, but at the time, we thought this was something that could be corrected with data processing. More details on this later.

7.6.4. CEST of Whole Blood

After showing that the peak at 10 ppm could be due to an exchangeable proton on deoxyhemoglobin, we decided to move to CEST imaging. Using the results of the FLEX spectra, we thought we were imaging a histidine proton and used a higher saturation pulse B_1 for CEST imaging because of faster exchange rates of histidine protons. The results of imaging 44% hematocrit whole blood at multiple oxygenations using CEST is presented in Figure 7.14.

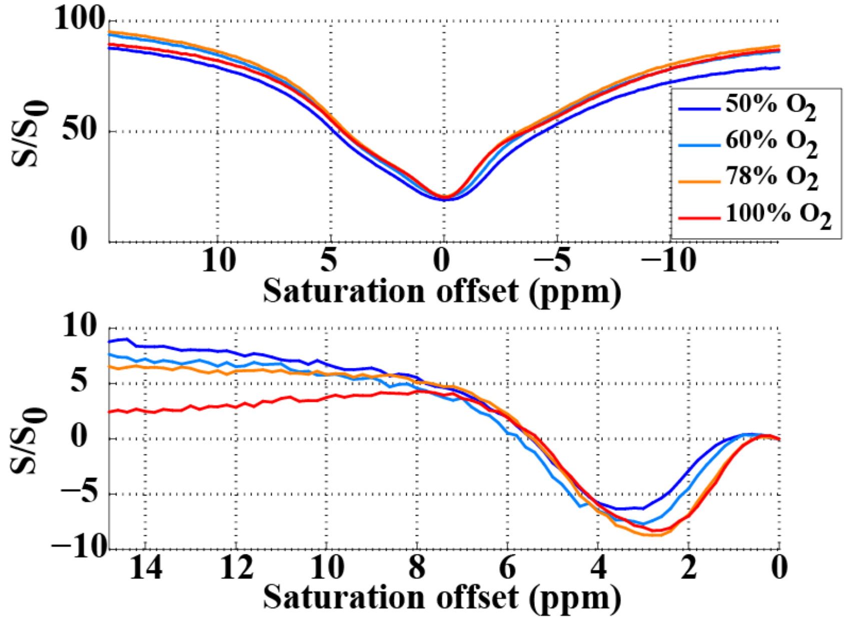

Figure 7.14. CEST spectra (top) and $MTR_{asymmetry}$ (bottom) for 44% hematocrit Whole Blood at Multiple Oxygenations.

Oddly, we did not see the exchangeable proton we thought we were able to image from the FLEX data. However, we do believe that this data makes sense. When looking at the CEST spectra, the direct saturation region becomes wider for lower oxygenations. This is due to a shorter T_2 in lower oxygenations and is in line with what is published in literature.

7.6.5. Varying Offset (and Pulse Duration) for FLEX Imaging on 44% Hematocrit Whole Blood at 66% Oxygenation

Therefore, we decided to go back to FLEX imaging to understand why this was happening. Using a 30 μs pulse, one simple modification we can make to the pulse sequence is to apply the pulse at -46.10 ppm (instead of +46.10 ppm). If an exchangeable proton were to resonate around 10 ppm, then changing the excitation pulse offset to the negative side would lower the sensitivity of detecting that proton because the FLEX excitation efficiency would be much lower for the peak around 10 ppm. The result for the FLEX sequence with pulse offset applied at -46.10 ppm on 44% hematocrit, 57% oxygenated whole blood is displayed in figure 7.15B. A dataset acquired with the same parameters but with the pulse offset at +46.10 ppm is displayed in figure 7.15A for comparison. Additionally, another scan with the FLEX excitation pulse set to +34.57 ppm was run with all other parameters (dur_{LTM}, number of LTMs, t_{evol}) equal.

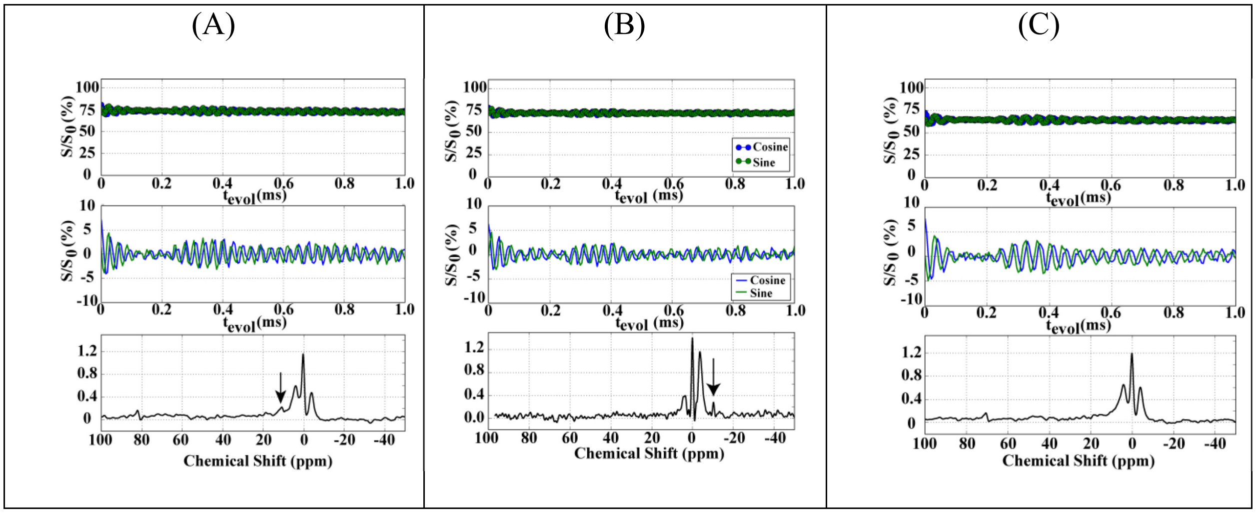

Figure 7.15. FLEX Spectra for (A) FLEX Excitation Pulse Applied at 46.10 ppm (B) FLEX Excitation Pulse Applied at -46.10 ppm (C) FLEX Excitation Pulse Applied at 34.57 ppm.

As expected, a peak around 10 ppm is seen in figure 7.15A, but a couple of aspects of figure 7.15B stand out. First, the NOE peak appears to be “larger” than the amide proton peak relative to figure 7.15A. This makes sense because application of the pulse at a negative offset frequency would give the NOE peak higher sensitivity because of a higher excitation efficiency (see FLEX excitation efficiency plots in figure 7.5). What is odd is that the peak that we originally detected around +10 ppm is now around -10 ppm. Furthermore, if we look to figure 7.15C where we moved the frequency offset at which the FLEX excitation pulse was applied closer to water, we would expect the peak around 10 ppm to have an even higher excitation efficiency than when the FLEX excitation pulse was at +46.10 ppm. However, that peak is not visible.

Our conclusion was that the peak around 10 ppm that we imaged using FLEX MRI was actually a flow artifact that manifested in a phase change. If we refer to the exponential FLEX equation (equation 7.5), we see that φ is an important component of the equation and represents the phase of the exchangeable proton that is being imaged. When blood (or any other sample that is imaged) is flowing, there is a phase change, and the phase change was being modulated in the FLEX spectrum. However, this explanation alone is not enough to explain the oxygenation dependence of the peak amplitude. Our conclusion is that the flow artifact resulted in a fold over of the bulk water peak. Because the T_1 and T_2 of blood are different for different oxygenations, we believe we were imaging these T_1 and/or T_2 differences in a fold over artifact.

Therefore, we concluded that we should stop the flow during RF preparation and data acquisition. We also took a closer look at the slice thickness and wondered whether or not RF inhomogeneities at the edge of the RF coil would cause any issues too. And finally, we believed that there may be baseline drift in our CEST images and needed a method to correct for this. Additionally, we thought that the high power of the saturation pulse (high B_1) was saturating much of the bound proton pool (from erythrocyte cell membranes), and we were worried that this generated an MT effect that could also mask the 1-2% effect that we were interested in.

7.7. Methods – Part 2

After realizing the issues that we faced may be hiding the signal we were interested in, we decided to modify our experiments. To do this, we reanalyzed our profile to reduce the RF inhomogeneities at the edges of the coil, and we flowed the blood in the phantom except during RF preparation and data acquisition. To flow blood in the phantom except during RF preparation and data acquisition, code was written to run in the background of the NMR console synchronized with the data acquisition to instruct me when to flow the blood and when to stop it.

7.7.1. Checking the Profile Acquisition

After realizing that RF inhomogeneities at the edges of the coil may be causing "un-clean" FLEX labeling that are flowed into the region where we were detecting the signal, we decided to run the following test. Before the spin echo acquisition, we added a single 30 μs 90° FLEX pulse to test the efficiency of the FLEX 90° pulse and varied the slice thickness (by varying the strength of the readout gradient).

Table 7.3. Checking the Efficiency FLEX 90° Pulse versus Slice Thickness.

Slice Thickness (cm)	**Percentage of Signal Left after 90° Pulse (%)**
3	15.37%
2.5	8.25%
2	8.01%
1	6.59%

It appeared that RF inhomogeneities at the edges of the coil significantly reduced the efficiency of the FLEX 90° labeling pulse when a 3 cm slice was used. Although it appears that the labeling efficiency is optimal for a 1 cm slice, we considered the loss in signal-to-noise ratio (SNR) with a 1 cm slice. SNR in MRI is directly proportional to slice thickness so a 1 cm slice would have three times less

SNR than a 3 cm slice. Ultimately, we decided a 2.5 cm slice maximized the signal-to-noise ratio and sufficiently reduced inhomogeneities from the edges of the RF coil.

7.7.2. Baseline CEST Spectrum Drift

Because the signals we detect using CEST are of the order of 1-2%, it is important to verify that the baseline of the z-spectra has no interference from other sources of noise. However, similar to the human data in Chapter 6, we noticed instabilities in the baseline of the CEST spectra so we ran unsaturated scans repeatedly for 47 minutes.

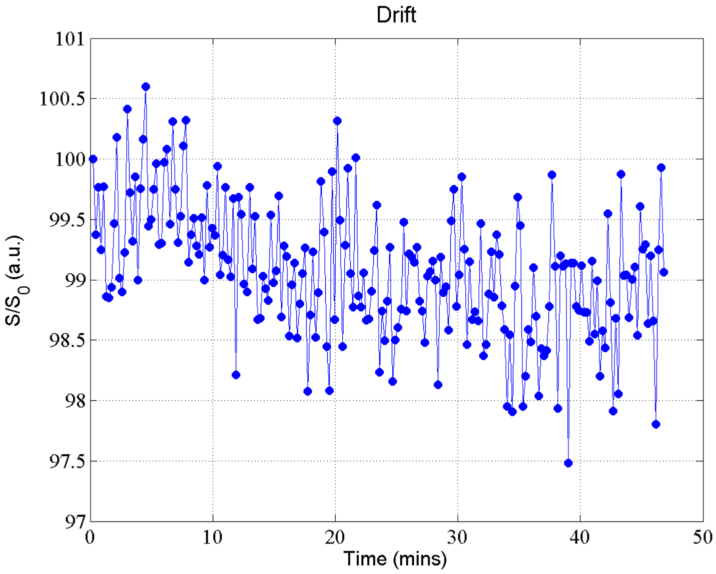

Figure 7.16. Drift of S_0 Images at 700 MHz.

Because of the baseline drift of unsaturated images, S_0 scans need to be interspersed throughout the CEST acquisition to correct for this drift. Baseline drift can be corrected in a similar manner as described in Chapter 6.

7.7.3. Testing Stop & Go with FLEX Acquisition

It is important to verify that stopping and flowing the blood does not cause any unwanted artifacts in the FLEX spectrum so we put 44% hematocrit whole blood, 100% oxygenation into the perfusion system and ran FLEX scans using a flow speed of 0.17 mL/second and while using the Stop & Go program. Furthermore, we increased the exchange time (t_{exch}) to 10 ms and reduced the number of LTMs to 200 so the total RF preparation time for FLEX remained the same (2 seconds).

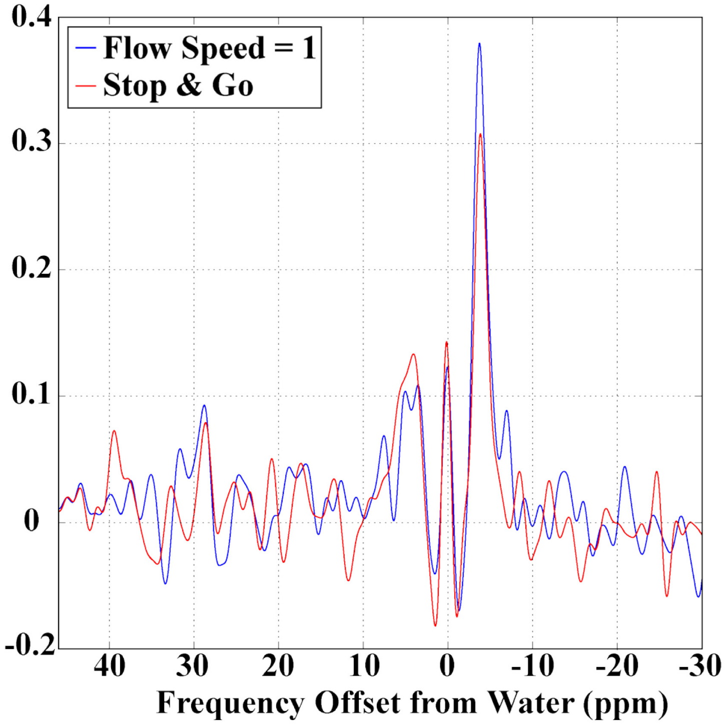

Figure 7.17. Testing Stop & Go Acquisition Using FLEX

It does not appear that the Stop&Go acquisition introduces any artifacts into the FLEX spectrum.

7.7.4. Testing Stop and Go with CEST Acquisition

Additional testing with the stop and go was also performed with CEST acquisitions where we flowed the blood during the pre-scan delay and stopped it three second before the saturation pulse was applied. We wanted to generate

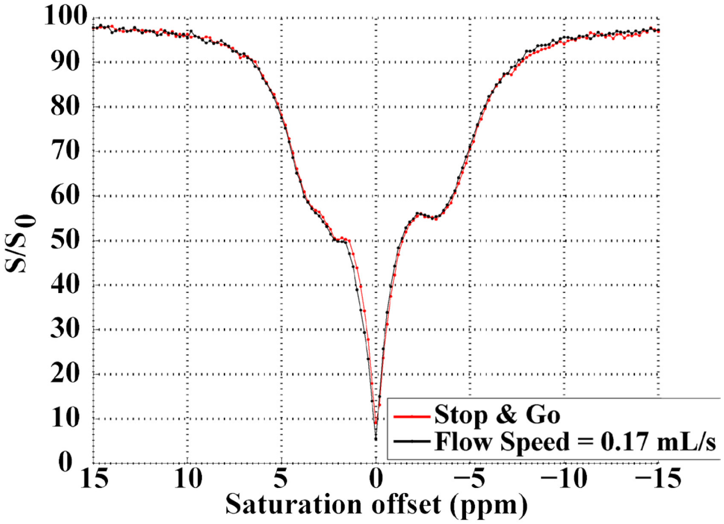

Figure 7.18. Testing Stop & Go Acquisition Using CEST.

Our data shows that the Stop & Go acquisition does not introduce any abnormal artifacts into the CEST spectra either.

7.7.5. CEST Acquisitions Using Stop & Go

After verifying that flowing the blood except during RF preparation and data acquisition did not induce any artifacts in the CEST and FLEX spectra, we proceeded with acquiring data this new way. This allowed us to maximize signal-to-noise by imaging all of the exchangeable protons that we labeled (previously a portion of the protons that were labeled were flowing out). We proceeded to acquire CEST data with the following sequence parameters: saturation pulse duration = 5 seconds, saturation pulse B_1 = 1.4 μT, offset frequencies acquired: -15 ppm to +15 ppm (increments of 0.2 ppm), pre-scan delay = 11 seconds. Unsaturated scans (S_0) were interspersed throughout the acquisition after every 10 frequencies acquired so baseline correction can be applied. This resulted in a total scan time of 44 minutes and 39 seconds. We also tried increasing the range at which our offset frequencies were acquired to -20 ppm to +20 ppm. This increased the total scan time to 59 minutes and 37 seconds. We acquired the CEST data using a saturation pulse B_1 = 1.4 μT and 2.5 μT.

7.8. Results and Discussion – Part 2

CEST – with flowing blood EXCEPT during RF preparation and data acquisition

After re-thinking the experiments and optimizing the necessary parameters, we ran the CEST scans again and saw some interesting results (figure 7.19).

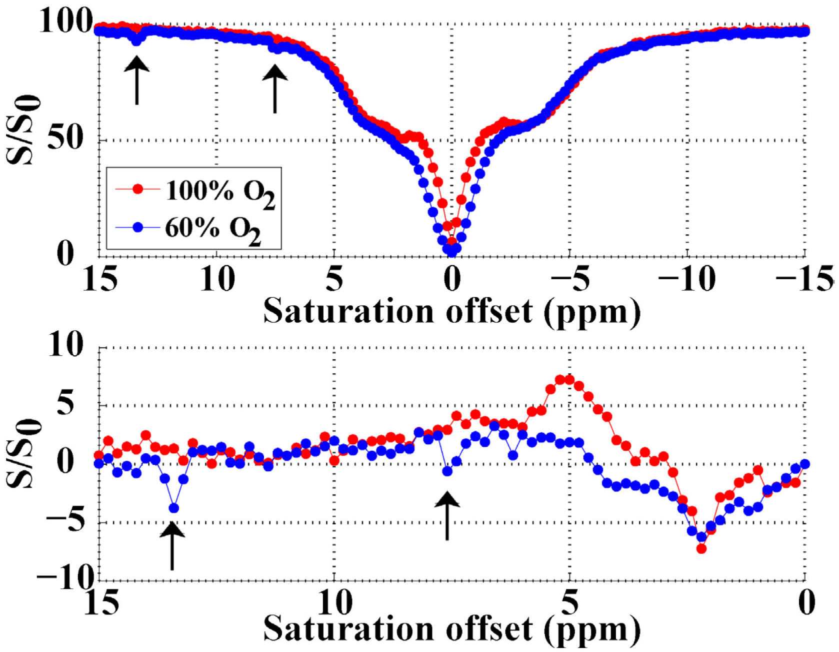

Figure 7.19. CEST spectra (top) and $MTR_{asymmetry}$ (bottom) of 44% hematocrit whole blood at 100% oxygenation (red) and 60% oxygenation (blue).

Saturation pulse duration = 5 seconds, saturation pulse B_1 = 1.4 μT.

The CEST data in figure 7.19 shows two distinct peaks in the CEST spectra of the 44% hematocrit whole blood at 60% oxygenation. The peak at +13.4 ppm shows an effect of 3-4% with a linewidth of 0.4 ppm, and the peak at +7.6 ppm shows an effect of 2-3% with a linewidth of 0.3 ppm. At a chemical shift of +7.6 ppm and +13.4 ppm in the 100% oxygenation CEST spectra, there do not appear to be any peaks. Unfortunately, after running a few scans, the oxygenation of the blood could not be held constant and the sample had to be discarded.

We tried to repeat that experiment at more oxygenations, however, we did not see the peaks that we previously saw. Results of follow-up CEST scans done with 44% hematocrit whole blood at 58%, 70%, 90%, and 100% oxygenations with saturation pulse duration of five seconds and saturation pulse B_1 of 1.4 and 2.5 µT are presented in figure 7.20.

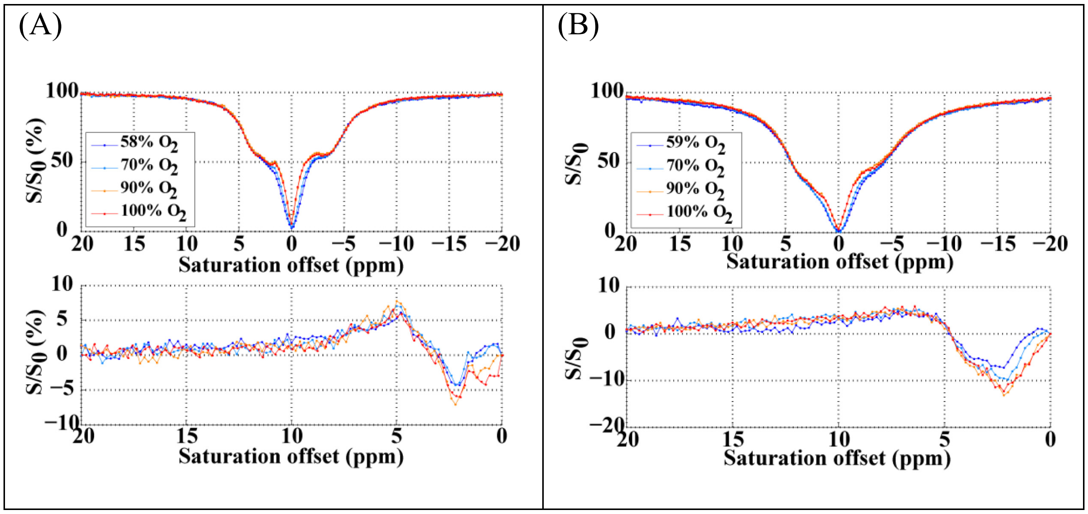

Figure 7.20. Follow-up Results CEST Spectra (top) and $MTR_{asymmetry}$ (bottom) for (A) B_1=1.4 µT (B) B_1=2.5 µT

There appear to be some small differences in the $MTR_{asymmetry}$ graphs between different oxygenations, but these effects are likely due to differences in T_1 and T_2, which are known to affect the direct saturation region of the CEST spectra.

7.9. Conclusion

In conclusion, while our initial efforts have taught us many new concepts and shown some interesting results for this topic, we have been unable to reproduce consistent results. Possible ways for improving stability includes using a motor with automatic control for stopping and starting flow that can be synchronized to the spectrometer or using a different experimental set-up with the capability of mixing blood while imaging occurs. We believe it should be possible to detect exchangeable protons in blood using CEST and FLEX, and a technique capable of doing so would be beneficial to stroke imaging.

7.10. References

1. Ogawa S, Lee TM, Kay AR, Tank DW. Brain magnetic resonance imaging with contrast dependent on blood oxygenation. Proc Natl Acad Sci U S A. 1990;87(24):9868-72.
2. Lu H, Ge Y. Quantitative evaluation of oxygenation in venous vessels using T2-Relaxation-Under-Spin-Tagging MRI. Magn Reson Med. 2008;60(2):357-63.
3. Qin Q, Grgac K, van Zijl PC. Determination of whole-brain oxygen extraction fractions by fast measurement of blood T(2) in the jugular vein. Magn Reson Med. 2011;65(2):471-9.
4. Bolar DS, Rosen BR, Sorensen AG, Adalsteinsson E. QUantitative Imaging of eXtraction of oxygen and TIssue consumption (QUIXOTIC) using venular-targeted velocity-selective spin labeling. Magn Reson Med. 2011;66(6):1550-62.
5. He X, Yablonskiy DA. Quantitative BOLD: mapping of human cerebral deoxygenated blood volume and oxygen extraction fraction: default state. Magn Reson Med. 2007;57(1):115-26.
6. van Zijl PC, Eleff SM, Ulatowski JA, Oja JM, Ulug AM, Traystman RJ, Kauppinen RA. Quantitative assessment of blood flow, blood volume and blood oxygenation effects in functional magnetic resonance imaging. Nature medicine. 1998;4(2):159-67.
7. Mihailescu MR, Russu IM. A signature of the T ---> R transition in human hemoglobin. Proc Natl Acad Sci U S A. 2001;98(7):3773-7.
8. Fung LW, Ho C. A proton nuclear magnetic resonance study of the quaternary structure of human homoglobins in water. Biochemistry. 1975;14(11):2526-35.

9. Greenfield NJ, Williams MN. Proton magnetic resonance studies of human hemoglobin. Histidine titrations. Biochim Biophys Acta. 1972;257(2):187-97.

10. Yuan Y, Simplaceanu V, Ho NT, Ho C. An investigation of the distal histidyl hydrogen bonds in oxyhemoglobin: effects of temperature, pH, and inositol hexaphosphate. Biochemistry. 2010;49(50):10606-15.

11. Russu IM, Ho NT, Ho C. A proton nuclear Overhauser effect investigation of the subunit interfaces in human normal adult hemoglobin. Biochim Biophys Acta. 1987;914(1):40-8.

12. Chang CK, Simplaceanu V, Ho C. Effects of amino acid substitutions at beta 131 on the structure and properties of hemoglobin: evidence for communication between alpha 1 beta 1- and alpha 1 beta 2-subunit interfaces. Biochemistry. 2002;41(17):5644-55.

13. Song XJ, Yuan Y, Simplaceanu V, Sahu SC, Ho NT, Ho C. A comparative NMR study of the polypeptide backbone dynamics of hemoglobin in the deoxy and carbonmonoxy forms. Biochemistry. 2007;46(23):6795-803.

14. Song XJ, Simplaceanu V, Ho NT, Ho C. Effector-induced structural fluctuation regulates the ligand affinity of an allosteric protein: binding of inositol hexaphosphate has distinct dynamic consequences for the T and R states of hemoglobin. Biochemistry. 2008;47(17):4907-15.

15. Ho C, Perussi JR. Proton nuclear magnetic resonance studies of hemoglobin. Methods in enzymology. 1994;232:97-139.

16. Ward KM, Balaban RS. Determination of pH using water protons and chemical exchange dependent saturation transfer (CEST). Magn Reson Med. 2000;44(5):799-802.

17. Ward KM, Aletras AH, Balaban RS. A new class of contrast agents for MRI based on proton chemical exchange dependent saturation transfer (CEST). J Magn Reson. 2000;143(1):79-87.

18. Zhou J, Payen JF, Wilson DA, Traystman RJ, van Zijl PC. Using the amide proton signals of intracellular proteins and peptides to detect pH effects in MRI. Nature medicine. 2003;9(8):1085-90.

19. McVicar N, Li AX, Suchy M, Hudson RH, Menon RS, Bartha R. Simultaneous in vivo pH and temperature mapping using a PARACEST-MRI contrast agent. Magn Reson Med. 2012.

20. Zhou J, Lal B, Wilson DA, Laterra J, van Zijl PC. Amide proton transfer (APT) contrast for imaging of brain tumors. Magn Reson Med. 2003;50(6):1120-6.

21. Jones CK, Schlosser MJ, van Zijl PC, Pomper MG, Golay X, Zhou J. Amide proton transfer imaging of human brain tumors at 3T. Magn Reson Med. 2006;56(3):585-92.

22. Lauzon CB, van Zijl P, Stivers JT. Using the water signal to detect invisible exchanging protons in the catalytic triad of a serine protease. Journal of biomolecular NMR. 2011;50(4):299-314.

23. Friedman JI, McMahon MT, Stivers JT, Van Zijl PC. Indirect detection of labile solute proton spectra via the water signal using frequency-labeled exchange (FLEX) transfer. Journal of the American Chemical Society. 2010;132(6):1813-5.

24. Lin CY, Yadav NN, Friedman JI, Ratnakar J, Sherry AD, van Zijl PC. Using frequency-labeled exchange transfer to separate out conventional magnetization transfer effects from exchange transfer effects when detecting ParaCEST agents. Magn Reson Med. 2012;67(4):906-11.

25. Yadav NN, Jones CK, Xu J, Bar-Shir A, Gilad AA, McMahon MT, van Zijl PC. Detection of rapidly exchanging compounds using on-resonance frequency-labeled exchange (FLEX) transfer. Magn Reson Med. 2012;68(4):1048-55.

26. Chanarin I. Blood and its diseases. 3rd ed. Edinburgh ; New York: Churchill Livingstone; 1984. viii, 333 p. p.

27. Takahashi S, Lin AK, Ho C. Proton nuclear magnetic resonance studies of hemoglobins M Boston (alpha 58E7 His leads to Tyr) and M Milwaukee (beta 67E11 Val leads to Glu): spectral assignments of hyperfine-shifted proton resonances and of proximal histidine (E7) NH resonances to the alpha and beta chains of normal human adult hemoglobin. Biochemistry. 1980;19(23):5196-202.

28. Liepinsh E, Otting G. Proton exchange rates from amino acid side chains--implications for image contrast. Magn Reson Med. 1996;35(1):30-42.

29. McMahon MT, Gilad AA, Zhou J, Sun PZ, Bulte JW, van Zijl PC. Quantifying exchange rates in chemical exchange saturation transfer agents using the saturation time and saturation power dependencies of the magnetization transfer effect on the magnetic resonance imaging signal (QUEST and QUESP): Ph calibration for poly-L-lysine and a starburst dendrimer. Magn Reson Med. 2006;55(4):836-47.

30. Liu ML, Mao XA, Ye CH, Huang H, Nicholson JK, Lindon JC. Improved WATERGATE pulse sequences for solvent suppression in NMR spectroscopy. Journal of Magnetic Resonance. 1998;132(1):125-9.

Chapter 8. Conclusion and Future Directions

8.1. Conclusion

The research described in this dissertation developed, optimized, and applied novel pulse sequences for imaging the ischemic penumbra in acute stroke patients. All of the work in this dissertation focused on magnetic resonance imaging modalities that are non-invasive owing to recent research showing the dangers (nephrogenic systemic fibrosis, an untreatable disease that at its severest stage leads to death) of using gadolinium-based contrast agents.

In this work, we quantitatively measured blood flow in the cerebellum using pseudocontinuous arterial spin labeling. It was demonstrated that a shorter labeling duration (600 ms) coupled with shorter post labeling delays could be used to quantify blood flow in the cerebellum. Acquired perfusion-weighted images correspond well to co-registered anatomical images, and cerebellar blood flow values and transit times fitted from data acquired over five volunteers are in good agreement with values published in literature from positron emission tomography and magnetic resonance imaging.

Next, we optimized magnetization transfer vascular space occupancy (MT-VASO), a cerebral blood volume weighted technique, for imaging acute ischemic stroke patients. Work done on this topic included modeling MT-VASO signal changes over the range of cerebral blood volume changes for ischemic stroke patients, testing the sequence on normal volunteers, and applying the sequence to elucidate changes in cerebral blood volume in patients. Results in three patients showed that MT-VASO localized increases in the cerebral blood volume of patients (due to autoregulation) with blood vessels that may not have collapsed yet. However, processing of this data is tedious and can be complicated by changes in the longitudinal and transverse relaxation times of tissue that change in later stages of ischemia.

Furthermore, recent research showing that reductions in cerebral blood flow beyond a certain threshold (30% of normal cerebral blood flow) causes neurons to switch from aerobic respiration (with oxygen) to anaerobic respiration (without oxygen) and leads to the build-up of lactic acid, which eventually causes tissue acidosis. We proceeded to apply pH-weighted imaging with CEST MRI to image the tissue acidosis, but noticed that scanner drift interfered with our measurements. We developed a baseline correction method for pH-weighted imaging based on acquiring unsaturated images interspersed within the saturated images. The unsaturated scans were fit with a smooth spline and the saturated images were corrected accordingly. This helped to reduce the noise within the CEST spectra leading to better fits using the Lorentzian difference method of analysis. Results from two ischemic stroke patients show that pH-weighted imaging could possibly predict tissue at risk of infarction more accurately than perfusion weighted imaging. An additional result from a third stroke patient (who also had stenosis in the left carotid artery) suggests that pH-weighted imaging may have some useful applications in carotid artery stenosis patients.

Finally, when thinking about how to develop image methods that are sensitive to other parameters that change for ischemia, we began work on developing a technique that could show changes in oxygenation based on using CEST MRI and frequency label exchange transfer MRI to study exchangeable protons on hemoglobin proteins in the blood. Although this study has not yet been completed yet, we have performed a number of experiments and learned a tremendous amount of information. Preliminary data shows the possibility of oxygenation dependent exchangeable protons at +13.4 ppm and +7.6 ppm downfield from the water peak.

8.2. Future Directions

Much of the work in this dissertation can be continued further. We will summarize how some of the work mentioned in this dissertation can be carried further in the following bullet points:

- For **pH-weighted imaging in ischemic stroke patients**, we have shown some promising initial results of pH-weighted imaging being a better predictor of tissue at risk of infarction. However, this is just the beginning. Further studies should systematically compare the predictive value (of tissue progressing to infarction) of pH-weighted imaging to perfusion weighted imaging using a receiver operating characteristic (ROC) curve, a plot based on correctly and falsely identifying tissue that will progress to infarction.

  Improvements can also be made from a sequence development perspective. Patient motion is always an issue especially with stroke patients given the level of discomfort that they feel. Recently, data acquisition methods have been developed and accounts for patient motion during acquisition. Tailoring such a sequence towards pH-weighted imaging for stroke patients would not be trivial but could be immensely useful in the clinic.

- For **using chemical exchange saturation transfer and frequency label exchange transfer to image exchangeable protons on hemoglobin,** our results show that it should be possible to image oxygenation dependent exchangeable protons on hemoglobin and use this as a way to spatially image oxygen extraction fractions in the brain and other areas of the body.

In conclusion, we believe the work presented in this dissertation has made contributions to the area of diagnostic stroke imaging. However, exciting future work is not limited to the contents of this dissertation. It will also depend on the funding opportunities and future students/researchers' interest. We hope more excellent research work could be carried out based on the contribution of the work from this dissertation.

ALAN HUANG CURRICULUM VITAE

CONTACT INFORMATION

Office Address	Home Address
F.M Kirby Functional MRI Research Center 707 North Broadway Street Baltimore, MD 21205 Tel: 443-834-0202 Fax: 443-923-9505	222 East University Parkway Baltimore, MD 21218 *E-mail:* Alan.J.Huang@jhmi.edu

EDUCATION

Ph.D. 2006 – 2014	**Biomedical Engineering** Specialization: Imaging Physics (MRI Pulse Sequence Development) **Johns Hopkins University School of Medicine**, Baltimore, MD
B.S. 2006	**Honors Electrical and Computer Engineering** Specialization: Biomedical Electronics, Digital Signal Processing **University of Texas at Austin**, Austin, TX
B.S. 2006	**Biology** Specialization: Neurobiology **University of Texas at Austin**, Austin, TX

WORK EXPERIENCE

FM Kirby Research Center Functional Brain Imaging – Thesis *02/07-present*

- Developed a chemical exchange saturation transfer-based neuroimaging technique to image oxygenation in the brain.
- Optimizing a chemical exchange saturation transfer-based imaging technique to image exchange-relayed Nuclear Overhauser Effects (NOEs).
- Co-developed a technique to improve stability of amide proton transfer (APT) imaging.
- Measured T_2 of bovine blood at 700 MHz to model chemical exchange and diffusion inside of red blood cells.
- Developed neuroimaging technique to image changes in cerebral blood volume to estimate tissue infarction in acute ischemic stroke patients.
- Imaged cerebellar blood flow quantitatively using pseudo-continuous arterial spin labeling.
- Optimized a cerebral blood volume technique to quantify changes in cerebral blood volume in acute ischemic stroke patients.

Wireless Networking and Communications Group - Dell Research Project 01/05-06/06

- Undergraduate student investigator in performance characterization of the new ultra wideband (UWB) IEEE 802.15 standard.
- Ran tests to determine whether coexistence issues existed between the ultra wideband (UWB) network and other wireless network standards.

Applied Research Laboratories – UT Austin – Honors Scholars Program 06/04 – 08/04

- Developed a prototype for electromagnetic vehicle detection sensor using giant magnetoresistors (GMR).
- Designed hardware interface and analog signal processing circuitry to improve signal quality from the GMRs.
- Programmed computer software and algorithms to accurately and efficiently process the electromagnetic signature of multiple vehicles.

Electro-Thermal Bioinstrumentation Lab 01/04 – 06/05

- Research description: Design of a thermistor-based data acquisition system using basic signal processing to measure atherosclerotic plaques.
- Ran comparative analysis of various biomedical amplifier designs.
- Built hardware circuits to confirm analysis and verify simulations of circuit parameters.

AWARDS

- Third Place in JHU Business Case Competition (2012)
- ISMRM Magna Cum Laude Abstract Merit Award (2012)
- Finalist for JHU Outstanding Teaching Assistant Award (2009)
    - Nominated by students for ability to breakdown complex concepts in a difficult undergraduate class.
- Recipient of ISMRM (International Society of Magnetic Resonance in Medicine) Travel Award (2008, 2011, 2012)
    - Amount Received: $400, $120, $140 respectively
- Recipient of Neuroengineering Training Grant Initiative (2007-2008)
    - Amount Received: ~$30,000
- Membership to Eta Kappa Nu, Electrical Engineering Honors Society (2004)
- Recipient of Ernest Cockrell Excellence in Engineering Scholarship (2002)
    - Amount received: $800

JOURNAL PUBLICATIONS

1. Qin Qin, **Alan J. Huang**, Jun Hua, John E. Desmond, Robert Stevens, Peter van Zijl. Three-dimensional whole-brain perfusion quantification using pseudo-continuous arterial spin labeling MRI at multiple post-labeling delays: accounting for both arterial transit time and impulse response function. NMR Biomed. 2013.

2. Craig Jones, **Alan J. Huang**, Jiadi Xu, Richard A. Edden, Michael Schär, Jun Hua, Nikita Oskolov, Domenca Zaca, Michael T. McMahon, Jay Pillai, Peter van Zijl. Nuclear Overhauser enhancement (NOE) Imaging in the human brain at 7T. Neuroimage. 2013 Aug; 77:114-24.

3. Jun Hua, Robert Stevens, **Alan Huang**, James Pekar, Peter van Zijl. "Physiological origin for the BOLD post-stimulus undershoot in human brain: vascular compliance versus oxygen metabolism." *Journal of Cerebral Blood Flow and Metabolism.* 2011 Jul;31(7):1599-611.

4. Bennett A. Landman, **Alan J. Huang**, Aliya Gifford, Deepti S. Vikram, Issel Anne L. Lim, Jonathan A.D. Farrell, John A. Bogovic, Jun Hua, Min Chen, Samson Jarso, Seth A. Smith, Suresh Joel, Susumu Mori, James J. Pekar, Peter B. Barker, Jerry L. Prince, Peter C.M. van Zijl**. "**MULTI-PARAMETRIC NEUROIMAGING REPRODUCIBILITY: A 3T RESOURCE STUDY." *NEUROIMAGE*. 2011;54(4):2854-66.

5. J. Hua, M.J. Donahue, Jason N. Zhao, Ksenija Grgac, **A.J. Huang**, J.Y. Zhou, and P.CM. van Zijl. "Magnetization Transfer Enhanced Vascular-Space-Occupancy (MT-VASO) Functional MRI". *Magnetic Resonance in Medicine.* 61:944-51. April 2009.

PUBLISHED CONFERENCE ABSTRACTS

1. CK Jones, **A.J. Huang**, J Xu, RAE Edden, M Schär, J Hua, N Oskolkov, MT McMahon, PCM van Zijl. "NOE Imaging in the Human Brain at 7T." *International Workshop on Chemical Exchange Saturation Transfer*, Annapolis, United States. October 2012.

2. Qin Qin, **Alan J. Huang**, Jun Hua, Robert Stevens, John E. Desmond, Peter van Zijl. "3D High-Resolution CBF Quantification with Consideration of Both Arterial Arrival Time and Impulse Residue Function." *International Society for Magnetic Resonance in Medicine Perfusion Workshop*, Amsterdam, Netherlands. October 2012.

3. **Alan J. Huang,** Craig Jones, Richard Leigh, Samson Jarso, Peter van Zijl. "Initial Application of pH-weighted Imaging with Pulsed CEST to Image an Acute Ischemic Stroke Patient," *International Society for Magnetic Resonance in Medicine*, Melbourne, Australia. May 2012. Page 1007.

4. Qin Qin, **Alan J. Huang**, Jun Hua, Robert Stevens, John E. Desmond, Peter van Zijl. "3D High-Resolution Whole-Brain Perfusion Measurement Using Pseudocontinuous ASL at Multiple Post-Labeling Delays." *International Society for Magnetic Resonance in Medicine*, Melbourne, Australia. May 2012. Page 3513.

5. **Alan J. Huang**, J. Hua, J. Farrell, Q. Qin, J. Pekar, Matthias van Osch, P.C.M. van Zijl. "Quantification of Cerebellar Blood Flow using Pseudocontinuous Arterial Spin Labeling", *International Society for Magnetic Resonance in Medicine*, Montreal, Canada. May 2011. Page 301.

6. **Alan J. Huang**, Li An, Jun Hua, Manus Donahue, Steven Warach, Peter C.M. van Zijl. "Non-invasive method to image changes in cerebral blood volume in acute ischemic stroke patients.", *International Society for Magnetic Resonance in Medicine*, Montreal, Canada. May 2011. Page 2134.

7. Craig Jones, **Alan J. Huang**, P.C.M. van Zijl. "Nuclear Overhauser Effects from a pulsed CEST Approach", *International Society for Magnetic Resonance in Medicine*, Montreal, Canada. May 2011. Page 2735.

8. Qin Qin, **Alan J. Huang**, Jun Hua, Matthias van Osch, P.C.M. van Zijl. "Acquisition Strategy of 3D GraSE with a Sharp Point Spread Function for Whole Brain ASL Perfusion Mapping at 3T", *International Society for Magnetic Resonance in Medicine*, Montreal, Canada. May 2011. Page 3983.

9. Jun Hua, Robert Stevens, **Alan J. Huang**, James J. Pekar, Peter C.M. van Zijl. "Hemodynamic responses following brief breath-holding and visual stimulation reconcile the vascular compliance and sustained oxygen metabolism origins for the BOLD post-stimulus undershoot in human brain", *International Society for Magnetic Resonance in Medicine,* Stockholm, Sweden, May 2010. Page 183.

10. Jun Hua, Robert Stevens, Manus J. Donahue, **Alan J. Huang**, James J. Pekar, Peter C.M. van Zijl. "Cerebral blood volume changes in arterial and post-arterial compartments and their relationship with cerebral blood flow alteration during brief breath-holding and visual stimulation in human brain", *International Society for Magnetic Resonance in Medicine,* Stockholm, Sweden, May 2010. Page 1127.

11. Manus J. Donahue, Robert D. Stevens, Jun Hua, **Alan Huang**, James J. Pekar, Peter C.M. van Zijl. "Cerebral Blood Flow (CBF) and Cerebral Blood Volume (CBV) Coupling Differs During Neuronal and Vascular Tasks", *International Society for Magnetic Resonance in Medicine,* Honolulu, Hawaii, May 2009. Page 513.

12. Jun Hua, Manus J. Donahue, Jason M. Zhao, Ksenija Grgac, **Alan J. Huang**, Jinyuan Zhou, Peter C. M. van Zijl. "Using Magnetization Transfer (MT) to Enhance SNR and CNR for VASO MRI", *International Society for Magnetic Resonance in Medicine,* Toronto, Canada, May 2008. Page 3582.

PRESENTATIONS AND INVITED TALKS

1. **Quantification of Cerebellar Blood Flow with Arterial Spin Labeling.** International Society for Magnetic Resonance in Medicine. Montreal, Quebec, Canada. May 10, 2011. Arterial Spin Labeling Section.

2. **Non-invasive method to image cerebral blood volume changes in acute ischemic stroke patients**. National Institute of Neurological Disorders and Stroke. Bethesda, MD. March 28, 2011. Invited by Dr. Steven Warach.

3. **Imaging Changes in Cerebral Blood Volume of Acute Stroke Patients.** Neuroradiology MR Physics Seminar Series. Johns Hopkins School of Medicine. October 19, 2010. Invited by Dr. Richard Edden.

4. **Non-invasive Method to Image Cerebral Blood Volume Changes in Acute Ischemic Stroke Patients.** Radiology MR Division Retreat, Johns Hopkins School of Medicine. October 8, 2010**.** Invited by Dr. Peter van Zijl.

5. **Towards Quantitative Cerebellar Blood Flow Imaging.** Radiology MR Division Retreat, Johns Hopkins School of Medicine. October 23, 2009**.** Invited by Dr. Peter van Zijl.

TEACHING EXPERIENCE

Signals and Controls Teaching Assistant (01/08-05/08 and 01/09-05/09)

- Involved in teaching approximately 120 sophomore undergraduate students the fundamentals of signals and systems properties and analysis.
- Guest lectured for professor several times throughout the semester.
- Taught three recitation sections (20-30 students each section) each week.

Digital Logic Design Teaching Assistant (01/04-05/04)

- Assisted in teaching course material to students.
- Graded tests, homework assignments, and lab assignments for students taking the course.

LEADERSHIP POSITIONS

President of JHU Biomedical Engineering PhD Council *08/09-08/10*

- Worked with professors and PhD students to develop and implement policies fair to both parties to accelerate the time to graduation in our department.
- Budgeted and planned symposia, leadership training, and social events for PhD students in the biomedical engineering department.
- Co-procured $10k activity budget per anum.

President of JHU Taiwanese Students Association *05/07-05/08*

- Worked with the JHU International Students Office and the Taipei Economic and Cultural Representative Office to implement guidelines to facilitate the smooth transition of over 100 recently arrived Taiwanese graduate students to life in the United States.
- Recognized by Taiwan’s Department of Education for outstanding leadership.

PROFESSIONAL SOCIETIES

International Society for Magnetic Resonance in Medicine (ISMRM) (2008 – present)
Order of the Engineer (2006 – present)
Eta Kappa Nu (Electrical Engineering Honors Society) (2004 – present)

SPECIAL SKILLS AND INTERESTS

1. Fluent in English and Mandarin Chinese; reading knowledge of Spanish.
2. Four years of programming experience with Philips MR machines.
3. Six years of experience with developing MATLAB software for image processing.
4. Five years clinical scanning experience (sickle cell patients, acute ischemic stroke, alcoholics, stroke recovery patients).
5. One year of experience using and programming high resolution NMR spectrometers (Bruker 500 MHz horizontal and vertical bore, Bruker 700 MHz).
6. Proficient in fMRI data analysis tools (FSL, FAST segmentation, FLIRT image registration, BET brain extraction tool).
7. Proficient in Microsoft Word, Excel, PowerPoint.

Vita

Alan Huang was born on June 29, 1984 in Redbank, New Jersey. He was raised by Dr. Nian Huang and Mrs. Piching Huang and grew up with his younger brother Bernard Huang. He received a Bachelors of Science in Electrical Engineering and a Bachelors in Science in Neurobiology in 2006 from the University of Texas at Austin in 2006. From there, he enrolled in the PhD program in the Department of Biomedical Engineering at Johns Hopkins University School of Medicine. His research interests lies in the development of novel contrast mechanisms with MRI.

After obtaining his PhD in Biomedical Engineering in Professor Peter van Zijl's lab, Alan will pursue a career in industry by joining Philips Healthcare in Best, Netherlands as a Clinical MRI Expert performing Research and Development functions within the MRI business unit.

He can be reached at Alan.J.Huang@jhmi.edu.